SOVIET
ATOMIC
ENERGY

АТОМНАЯ ЭНЕРГИЯ
(ATOMNAYA ÉNERGIYA)

TRANSLATED FROM RUSSIAN

SOVIET ATOMIC ENERGY

Soviet Atomic Energy is abstracted or indexed in Chemical Abstracts, Chemical Titles, Pollution Abstracts, Science Research Abstracts, Parts A and B, Safety Science Abstracts Journal, Current Contents, Energy Research Abstracts, and Engineering Index.

SOVIET ATOMIC ENERGY

CONTENTS

Engl./Russ.

CONTENTS

(continued)

Engl./Russ.

The Russian press date (podpisano k'pechati) of this issue was 6/3/1985.
Publication therefore did not occur prior to this date, but must be assumed
to have taken place reasonably soon thereafter.

HYDRODYNAMICS OF THE PRESSURE AND UPPER MIXING CHAMBERS OF THE BN-600 REACTOR OF THE BELOYARSK NUCLEAR POWER STATION

T. V. Zubkova, A. I. Karpenko,
A. A. Lyzhin, and A. G. Sheinkman

UDC 621.039.526

Mixing conditions of the coolant in the mixing chambers of nuclear reactors determine the reliability of the signals entering the safety and control system of the reactor [1, 2]. This assumption underlied a study of mixing processes in the pressure and upper mixing chambers of the BN-600 reactor of the Beloyarsk nuclear power station under operating conditions.

When the rated power of the BN-600 reacotr was first attained, coolant flow in the first circuit was investigated by a thermocouple method. It was observed that the temperature in the upper mixing chamber is nonuniform due to nonuniform heating in the core and blanket fuel assemblies and to the hydrodynamics of the chamber. According to the readings of thermocouples, temperature stratification was observed at the outlets of fuel assemblies (FA), in the reactor tank, and at the inlets of intermediate heat exchangers (IHE). It was found that there was no complete mixing of the coolant in the pressure chamber. Parallel flows moving along pressure conduits of different loops from the three main circulators of the first circuit MC-1 mix only slightly in the pressure chamber; at the FA inlets they preserve the different temperatures they had at the outlets of the IHE of different loops. At the FA outlets the coolant flow preserves the different temperatures of the first circuit loops.

Slight mixing of loop flows was observed in experiments under operating conditions with various values of the BN-600 reactor power (50 and 85% of power rating) and various coolant flow rates in the first circuit (70 and 90% of the rated coolant flow, respectively). While the power remained steady, the sodium temperature was changed at the IHE outlet in one (the i-th) of the three working loops by changing the rotational speed of the i-th MC-1 with a constant rotational speed of the other MC-1. As the steady-state operating conditions were reached, major thermal properties of the sodium circuits of the BN-600 reactor were measured; afterwards, the initial rotational speed of this MC-1 was restored. Similar operations were alternately carried out for all the MC-1. Thermal reactor power was maintained constant during the experiments by automatic control rods.

Figure 1 shows the variation of mean coolant temperature of each loop at the IHE outlets with variation of the rotational speed of one MC-1. Temperature measurement at the IHE outlet of each loop and at the FA outlets makes it possible to evaluate the pattern of temperature variation at the FA inlets.

All the thermocouples over the FA caps were divided into three groups according to the sign of the change in the readings. As the coolant flow rate along the i-th loop of the first circuit increases, thermocouple readings over the FA of the i-th group increase, while those over the FA of the other two groups decrease, with the absolute value of variation of thermocouple signals in the i-th group being approximately twice as great as in the others (Fig. 2).

The readings of thermocouples located at the IHE inlets also point to the loop pattern of coolant flow at the reactor outlet. The variation of sodium temperature at the IHE inlets in the loops is similar to the temperature variation at the outlets of these IHE (Fig. 3), but its absolute value is smaller. As the operating conditions are stabilized 40 min after the rotational speed of one of the MC-1 is changed, the coolant temperature of the first circuit in different loops does not become uniform.

On one occasion when the third block was put into operation, thermocouple readings of the first circuit were recorded as power grew from 60 to 95% of its rated value and the rotational speed of all the MC-1 was successively increased. An analysis of experimental data showed that in this case as well the variation pattern of all the thermocouple readings of the first circuit was similar to the one considered above.

449
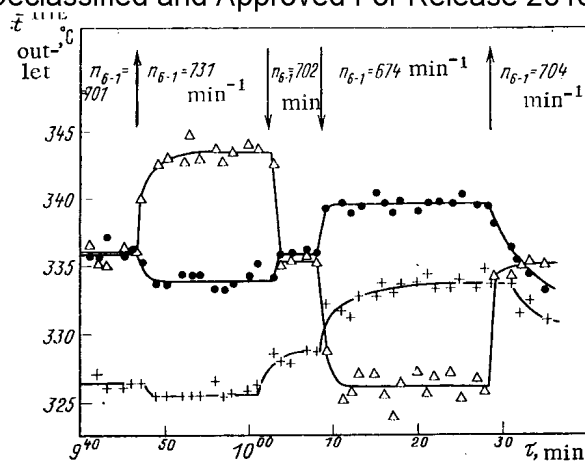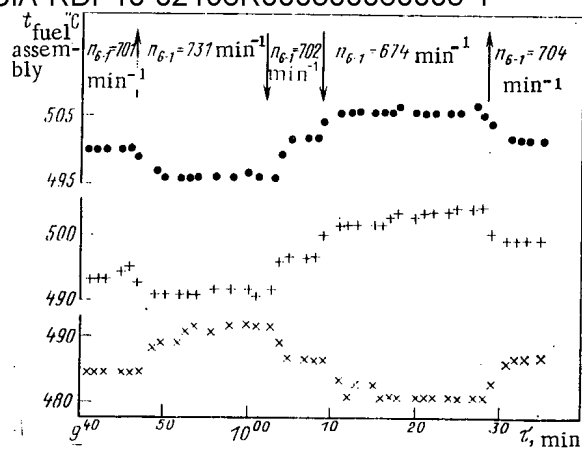
Fig. 1

Fig. 2

Fig. 1. Variation of coolant temperature at the outlets of the IHE in different circulation loops with variation of rotational speed of one MC-1: ●) the 4th loop; +) the 5th loop; Δ) the 6th loop.

Fig. 2. Coolant temperature variation at the FA outlets with variation of the rotational speed of one of the MC-1: ●) cell 11-17 (4th loop); +) cell 18-21 (5th loop); ×) cell 12-05 (6th loop).
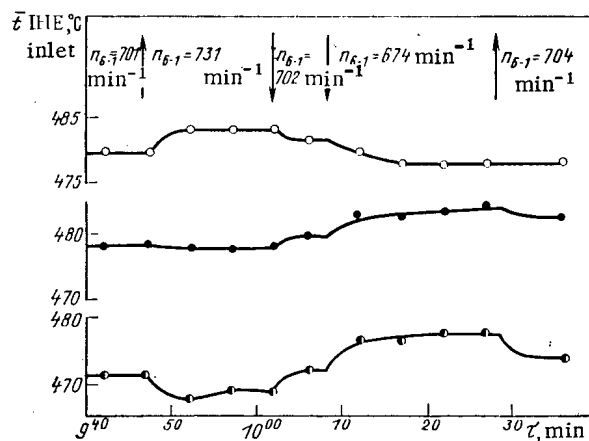
Fig. 3. Variation of coolant temperature at the IHE inlets in different circulation loops with variation of the rotational speed of one of the MC-1: ○) 6th loop; ●) 5th loop; ◐) 4th loop.

The results of the experiments suggest that only a weak interaction of loop sodium flows takes place in the tank-type BN-600 reactor, i.e., there is no complete mixing of the coolant either in the lower or in the upper mixing chambers. Incomplete mixing at the inlet and outlet of the core must be taken into account in the thermal design of operating conditions with a significant difference between the temperature at the IHE outlet of one circulation loop and the temperatures at the IHE outlets of the two other circulation loops.

A sector (loop) model of coolant motion is proposed for determining the coolant flow pattern in the first circuit of the BN-600 reactor. In accordance with this model, the entire reactor charge is subdivided into three sectors. The coolant is admitted from each sector into two IHE of one loop. The subdivision is carried out in such a way that the bulk coolant temperature at the outlet of each sector was equal to the mean coolant temperature at the IHE inlets of each loop obtained from the thermal balance between the first and second circuits. The largest discrepancy between the above temperatures did not exceed 4°C over the whole range of operating modes of the reactor. An example of a subdivision of the reactor charge into three sectors is given in Fig. 4. The boundaries of the sectors are determined according to the variation pattern of the thermocouple readings over the FA caps, i.e., each sector contains

450
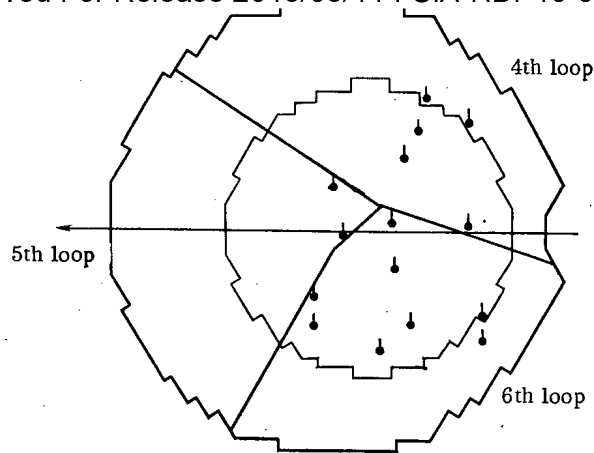
Fig. 4. Subdivision of the charge of the
BN-600 reactor into sectors.

thermocouples of one of the three groups defined above. The boundaries of the sectors are not strictly fixed, but are rather dependent on the relationship between the MC-1 rotational speeds, i.e., on the relationship between the loop flow rates.

Finally, let us note that incomplete coolant mixing is also characteristic of other types of reactors with mixing chambers of a relatively large diameter in comparison to their axial dimensions [2].

Thus, reactor experiments have demonstrated a weak interaction among loop sodium flows in the pressure and upper mixing chambers of the BN-600 reactor. A sector model of coolant flow is in good agreement with experimental data for practicable modes of operation of the reactor. The sector pattern of the coolant flow must be taken into consideration in forming the signals entering the safety and control system, in choosing the number and location of thermocouples in the first circuit, and in coolant extraction for the monitoring system of the fuel-element containment.

LITERATURE CITED

1. A. N. Opanasenko and N. N. Shan'gin, "Hydrodynamics of mixing chambers of nuclear power-plants," At. Énerg., 52, No. 6, 385-389 (1982).
2. S. A. Tsimbalov and A. V. Kraiko, "Temperature field in the coolant at the inlet of the VVER-440 water-cooled, water moderated power reactor core," At. Énerg., 52, No. 5, 304-308 (1982).

451

METHODS OF ESTIMATING HIGH-BOILING CHANNEL REACTOR (RBMK)

FUEL-PIN AND CASSETTE RELIABILITY

A. I. Klemin and A. G. Sitkarev   UDC 621.039.58+621.039.546.3

INTRODUCTION

The core in the RBMK-1000 or RBMK-1500 contains approximately 1400-1700 fuel-pin cassettes, in accordance with the working period. Each such assembly consists of two parts, with 18 fuel pins in each. The core reliability is largely determined by that of the cassettes, which in turn is dependent on that of the individual pins. At nuclear power stations having a high-boiling channel reactor (RBMK), there are thousands of cassettes in use simultaneously (correspondingly, up to 500,000 fuel pins). It is therefore important to estimate the working reliability parameters for the RBMK cassettes and pins. It is necessary to know the actual values of the reliability parameters for use by designers, manufacturers, and power station staff.

However, up to now there has been a lack of a complete set of such parameters and also a lack of reliable methods of estimating them, and no confidence-range estimates have been made at all.

Here we describe applied methods of using cassette working data to calculate point and interval estimators for the main range of reliability parameters for RBMK. The methods are of nonparametric type and do not require one to know the distribution of the cassette operating times to a limiting state, which is usually unknown in practice.

BASIC CONCEPTS

RBMK cassettes and pins are components that cannot be repaired. It is assumed that all the pins in one cassette are equally reliable. The limiting state of a cassette is the state in which further operation must be halted (the cassette unloaded) either to ensure a normal radiation environment in the power station (if the sealing has failed) or else to maintain the necessary reactivity margin and power production pattern in the core (on account of burnup). Sealing failure is the loss of sealing in one or more pins. Cassette failure is an event involving attainment of the limiting state because of sealing failure.*

The cassette life to failure is a random quantity, and the life at which the state attains the limiting one because of burnup is determined by the reloading in a particular unit of the power station. The fuel recharging conditions (recharging order, power produced by the unloaded cassettes, etc.) differ for the various units in a station, although they retain the general tendencies for this type of reactor, because of various random working factors. The cassette life at which the latter attains the limiting burnup state is random. In addition to the purely random factors, the life is influenced by definitive factors such as the position in the core (central or peripheral) and the working period (a transient period after the first fuel loading or the period of stationary reloading) [1].

During RBMK operation, a cassette is a nondemountable combination of pins. From the reliability viewpoint, it is a so-called coupled system [2], in which the attainment of the limiting state by a component is a dependent event responsible for change in the output parameter of the entire system. The limiting state of a pin must be determined from that for the cassette.

By pin limiting state we understand a state characterized either by loss of sealing and the attainment by the corresponding cassette of the limiting state because of sealing failure, or else burnup in the pin and attainment by this cassette of the limiting state due to burnup. The fact of sealing failure in a pin (cassette) does not necessarily indicate failure, since

---

*The detailed features (criteria) for cassette failure are laid down by the corresponding technical specification (TS).

0038-531X/85/5806-0452$09.50   © 1985 Plenum Publishing Corporation

it continues to perform the basic function of producing thermal energy. Pin failure is an event in which the pin sealing fails and the corresponding cassette attains the limiting state because of that sealing failure.

Clearly, the instants of pin failure and failure in the corresponding cassette coincide. A failed cassette may contain one or more failed pins. The sealed pins in a failed cassette are unloaded prematurely, before they have failed.

If the working life of a fuel-pin assembly t_{fpa} and that of a fuel pin t_{fp} are estimated in energy production units, we have that $t_{tp} = t_{fpa}/k$, where k = 36 is the number of pins in a cassette. If t_{fp} and t_{fpa} are measured in time units, then $t_{fp} = t_{fpa}$ (the case will be analogous if t_{fp} and t_{fpa} are measured in other units such as relative ones for the energy production per unit mass of fuel and so on).

Set of RBMK Reliability Parameters for Cassettes and Pins

In accordance with the technical standardization documentation (TSD), the main standardized fault-free parameter for a cassette is $\mathscr{P}(t)$, the probability of fault-free operation for a time t (over the interval [0, t]). The working-life parameters for RBMK cassettes can be taken as the following: $T(\theta)$ the mean working life* of a cassette with a given working time θ up to unloading because of burnup, T_t the mean working life of the cassette in the transient period of operation, and T_{st} the mean working life when the reactor works in the stationary state of fuel reloading.

Here T_t and T_{st} are the basic parameters standardized by the TSD. The same distinction must be drawn for the mean period of service for a cassette. We elucidate the meanings of these working-life parameters by means of mathematical expressions:

$$T(\theta) = \int_0^\theta \mathscr{P}(t)\, dt. \tag{1}$$

The difference

$$\Delta T(\theta) = \theta - T(\theta) \tag{2}$$

is the mean unused working life of a cassette due to possible failure before operation to θ:

$$T_t = \sum_{i=1}^s w_t(i)\, T[\theta_t(i)], \tag{3}$$

where $w_t(i)$, $i = \overline{1, s}$ is the proportion of cassettes (out of the total number of cassettes used in the transient state) to be reloaded on attaining the working state $\theta_t(i)$, $\sum_{i=1}^s w_t(i) = 1$; while $\theta_t(t)$, $i = \overline{1, s}$ is the set of characteristic working states (the means over group i) before the the cassettes are reloaded because of burnup in the transient state, and s is the total number of $\theta_t(i)$.

The difference

$$\Delta T_t = [\sum_{i=1}^s w_t(i)\theta_t(i)] - T_t \tag{4}$$

corresponds to the mean unused life of an assembly arising from possible failure in the transient state, and

$$T_{st} = \sum_{i=1}^r w_{st}(i)\, T[\theta_{st}(i)], \tag{5}$$

where $\theta_{st}(i)$, $i = \overline{1, r}$ is the mean energy production before the cassette is unloaded because of turnup from core region i in the stationary state of continuous fuel reloading, r is the

*We note that the working life is the name given to the life up to the limiting state.

453

the number of distinct core regions, and $w_{st}(i)$, $i = 1$, r is the proportion of the consumption in reloading (in unit time in the stationary reloading state) corresponding to core region i, $\sum_{i=1}^{r} w_{st}(i) = 1$.

The difference

$$\Delta T_{st} = [\sum_{i=1}^{r} u_{st}(i)\, \theta_{st}(i)] - T_{st} \tag{6}$$

is the mean unused cassette life arising from possible failure in the stationary reloading state.

The reliability parameter set for a fuel pin is completely analogous to that for a cassette: $P(t)$ the probability of fault-free pin operation up to time, t and $t(\vartheta)$, t_t, and t_{st} the mean pin working lives with a given value of ϑ before unloading because of burnup in the transient state and in the stationary state of continuous reloading correspondingly.

The same division is performed for the mean service of a pin. The formulas for the mean pin working lives coincide with (1), (3), and (5) if the cassette characteristics are replaced by the pin ones. The weighting function $w_t(t)$ and $w_{st}(t)$ are identical for RBMK cassettes and pins.

Initial Data for Calculating RBMK Cassette Reliability Parameters

These initial data can be either statistical information derived from one unit at a power station or the over-all statistical information from several units at one or more stations. In the first case, the information may be divided into the following four types in accordance with the reactor working period:

I. The reactor works with the initial loading. The unloading of cassettes because of burnup has not begun. Cassettes are unloaded only either because of failure or for reasons not related to the cassettes attaining the limiting state (for example, a cassette may be unloaded because of a leak through the sealing channel at the upper supporting end of the cassette). In that case, one uses information on all the cassettes both in the core and unloaded at a given instant.

II. The reactor works in the transient state of fuel reloading. Cassettes are unloaded either because they have attained the limiting state or for unrelated reasons. In formation is given on all the cassettes, as in case I.

III. The reactor has reached the stationary reloading state, and one has the information on the entire transient period. One uses data on all the cassettes unloaded in that period.

IV. The reactor is working in the stationary reloading state. Information is available on all the cassettes in the core and unloaded during the entire working period from startup.

The overall statistical data from several units may represent a combination of any of these four types.

In turn, the working periods of the cassettes given in the initial data are of four types:

A. working to failure: $\tau_1, \ldots, \tau_L$;

B. the working times for cassettes in the core at the time the information is obtained: $t_{1,1}, t_{1,2}, \ldots, t_{1,M_1}$;

C. the working times for cassettes unloaded on attaining the limiting state because of burnup: $t_{2,1}, t_{2,2}, \ldots, t_{2,M_2}$; and

D. working times for cassettes unloaded for reasons not related to the cassettes attaining the limiting state.

Type I information contains working periods of types A, B, and D; types II and IV contain the entire set A-D; and type III contains A, C, and D.

Estimating the RBMK Fault-Free Cassette Operation Parameter

The algorithm for calculating the estimators for the probability of fault-free operation is independent of the type of initial data used (I-IV). To derive the reliability estimators,

454

the initial information must be converted to a multitruncated set, for which one has to spec-
ify the working times of cassettes to failure $\tau_1 < \tau_2 < \ldots < \tau_L$, where is the total number of
working times to failure, together with the values of the different working times for the un-
failed cassettes (truncated working times) $t_1 < t_2 < \ldots < t_M$, and the corresponding set of
numbers of these cassettes $m_1, \ldots, m_M$, where M is the number of unfailed cassettes differing
in value of working time (these data are obtained by combining the working times of types B–D

in accordance with the values in the initial information), and the sample volume $N, \sum_{i=1}^{M} m_i + L = N$.

The point estimator for the probability of fault-free operation up to time t is given
by

$$\hat{\mathcal{P}}(t) = \left[\prod_{i=1}^{d} \frac{N - \sum_{j=1}^{i-1} m_j - \sum_{j=1}^{i} l_j}{N - \sum_{j=1}^{i-1} m_j - \sum_{j=1}^{i-1} l_j} \right] \frac{N - \sum_{j=1}^{d} m_j - \sum_{j=1}^{d} l_j - l}{N - \sum_{j=1}^{d} m_j - \sum_{j=1}^{d} l_j} = \left[\prod_{i=1}^{d} \frac{N - M_{i-1} - L_i}{N - M_{i-1} - L_{i-1}} \right] \frac{N - M_d - L_d - l}{N - M_d - L_d}, \qquad (7)$$

where d is the number of truncated working periods in the working information on failed cas-
settes less than t, $0 \leqslant d \leqslant M$, with l_j the number of working periods to failure in the inter-
val $[t_{j-1}, t_j]$ between truncations, $l_j \geqslant 0$; and l is the number of working periods to failure

in the initial set belonging to the interval $[t_d, t]$, $l \geqslant 0$; $M_i = \sum_{j=1}^{i} m_j$, $M_0 = 0$, $L_i = \sum_{j=1}^{i} l_j$, $L_0 = 0$.

The value of the lower confidence limit to this probability of fault-free operation $\mathcal{P}_{ff}(t)$
for a given probability β is defined by the following algorithm.

For the case where $\sum_{i=1}^{d} l_i + l = L_d + l = 0$, i.e., up to working time t in the initial sam-
ple there are no failures,

$$\mathcal{P}_{ff}(t) = (1 - \beta)^{1/(N - M_d)}. \qquad (8)$$

If $L_d + l \neq 0$, i.e., if there are cassette failures up to working time, t, then for sufficient-
ly large value of $n_d = N - M_d - L_d$

$$\mathcal{P}_{ff}(t) = \frac{\hat{\mathcal{P}}(t) + \frac{1}{2} \frac{u_\beta^2}{n_d} - u_\beta \sqrt{\frac{\hat{\mathcal{P}}(t)[1 - \hat{\mathcal{P}}(t)]}{n_d} + \frac{1}{4} \frac{u_\beta^2}{n_d^2}}}{1 + \frac{u_\beta^2}{n_d}}, \qquad (9)$$

where u_β is defined by $\beta = \frac{1}{\sqrt{2\pi}} \int_{-\infty}^{u_\beta} e^{-t^2/2} dt$. When n_d is small, $\mathcal{P}_{ff}(t)$ is determined from the fol-
lowing equation [3]:

$$I_{\mathcal{P}_{ff}} [n_d - n_d(1 - \hat{\mathcal{P}}), \, n_d(1 - \hat{\mathcal{P}}) + 1] = 1 - \beta, \qquad (10)$$

where the function $I_{\mathcal{P}}(n - x, \, x + 1)$ takes the form

$$I_{\mathcal{P}}(n + x, \, x + 1) = \frac{\int_0^{\mathcal{P}} y^{n-x-1}(1 - y)^x \, dy}{\int_0^1 y^{n-x-1}(1 - y)^x \, dy}.$$

In deriving (8)–(10) for $\mathcal{P}_{ff}(t)$. we have used the data of [3, 4].

Estimating RBMK Working Life for Cassettes from Data from One Power Station Unit

The type of statistical information available determines whether it is possible to obtain
estimators for the various working-life parameters and the accuracy in them.

Type I Statistical Information. We are given the working times

A. $\tau_1, \tau_2, \ldots, \tau_L;$

B. $t_{1,1}, t_{1,2}, \ldots, t_{1,M_1};$ (11)

D. $t_{3,1}, t_{3,2}, \ldots, t_{3,M_3}$

$$(L + M_1 + M_3 = N).$$

In that case, it is impossible to estimate the cassette working life without knowing the form of the distribution for the working times of the cassettes to failure (i.e., by the non-parametric method). One can only obtain estimators for the probabilities of fault-free operation from (7)-(10).

Type II Statistical Information. We are given the working times

A. $\tau_1, \tau_2, \ldots, \tau_L;$

B. $t_{1,1}, t_{1,2}, \ldots, t_{1,M_1};$

C. $t_{2,1}, t_{2,2}, \ldots, t_{2,M_2};$ (12)

D. $t_{3,1}, t_{3,2}, \ldots, t_{3,M_3}$

$$(L + M_1 + M_2 + M_3 = N).$$

From working times C one can identify the part of the complete set of characteristic (average) working times to reloading arising from burnup in a given unit: $\hat{\theta}_t(1) < \hat{\theta}_t(2) < \ldots < \hat{\theta}_t(s_1)$, where $s_1 \geqslant 1$, and for each working time $\hat{\theta}_t(p)$, $p = 1, s_1$ we can estimate the parameter $T[\hat{\theta}_t(p)]$.

For this purpose, the initial data of (12) must be represented as a multitruncated set, as above, and the estimator $T[\hat{\theta}_t(p)]$ is derived from the formula

$$\hat{T}[\hat{\theta}_t(p)] = \frac{\sum_{j=1}^{l_1} \tau_j}{N} + \sum_{i=1}^{d} \hat{\mathscr{P}}_i \frac{\sum_{j=1}^{l_{i+1}} \tau_{L_i+j}}{N - M_i - L_i} + \hat{\mathscr{P}}[\hat{\theta}_t(p)]\hat{\theta}_t(p),$$ (13)

where d is the number of truncated working periods less than $\hat{\theta}_t(p)$ and $\hat{\mathscr{P}}_i$, $\hat{\mathscr{P}}[\hat{\theta}_t(p)]$ are the estimators from (7) for the probability of fault-free operation to working times to t_i and $\hat{\theta}_t(p)$ correspondingly. We note that the sum of the working times A, C, and D of (12) divided by the total number

$$\left(\sum_{j=1}^{L} \tau_j + \sum_{j=1}^{M_2} t_{2,j} + \sum_{j=1}^{M_3} t_{3,j}\right)/(L + M_2 + M_3),$$

which until recently has been used to calculate the mean cassette working life, in the general case is not an estimator for this parameter but instead is the mean of the working times taken over the unit for cassettes unloaded from the reactor.

Type III Statistical Information. We are given the working times

A. $\tau_1, \tau_2, \ldots, \tau_L;$

C. $t_{2,1}, t_{2,2}, \ldots, t_{2,M_2};$

D. $t_{3,1}, t_{3,2}, \ldots, t_{3,M_3}$ (14)

$$(L + M_2 + M_3 = N).$$

From working times C, we isolate the complete set of characteristic (mean) working times to cassette unloading because of burnup in a given unit: $\hat{\theta}_t(1) < \hat{\theta}_t(2) < \ldots < \hat{\theta}_t(s)$. According to (3), the estimator for the mean cassette working life in the transient period T_t is given by

$$\hat{T}_t = \sum_{i=1}^{s} \hat{w}_t(i)\hat{T}[\hat{\theta}_t(i)],$$ (15)

456

where $\hat{w}_t(i) = \hat{w}[\hat{\theta}_t(i)]$ is the estimator for the weighting function $w_t(i)$.

The estimators $\hat{T}[\hat{\theta}_t(i)]$ are calculated from (13), for which the initial data of (14) are represented as a multitruncated set, as above. The preliminary estimators for $w_t(i)$ may be taken as the design values. The refined estimators $w_t(i)$ corresponding to the actual reloading are determined from the type III information as follows.

For these working times $\hat{\theta}_t(1) < \hat{\theta}_t(2) < \ldots < \hat{\theta}_t(s)$, one finds the corresponding number of cassettes unloaded because of burnup with working times close to $\hat{\theta}_t(i)$: n_1, n_2, $\ldots$,

n_s, $\sum_{i=1}^{s} n_i = M_2$. The working times of types A and D of (14) are combined and arranged in

increasing order, from which one determines values of p_i, the numbers of working times belonging to the intervals $[\theta_t(i-1), \hat{\theta}_t(i)]$, $\hat{\theta}_t(0) = 0$. Then the estimators $\hat{w}_t(i)$ are calculated from

$$\hat{w}_t(1) = n_1/(N - p_1);$$

$$\hat{w}_t(i) = \left[\prod_{j=1}^{i-1} \left(1 - \frac{n_j}{N - \sum_{r=1}^{j} p_r - \sum_{r=1}^{j-1} n_r} \right) \right] \frac{n_i}{N - \sum_{j=1}^{i} p_j - \sum_{j=1}^{i-1} n_j}. \tag{16}$$

If the initial set of (14) does not contain working times of type D, formula (15) becomes as follows on using the estimators of (16):

$$\hat{T}_t = \frac{\sum_{i=1}^{L} \tau_i + \sum_{i=1}^{M_1} t_{2.i}}{N}. \tag{17}$$

Type IV Statistical Information. We are given the working times

$$
\begin{aligned}
&\text{A. } \tau_1, \tau_2 \ldots, \tau_L; \\
&\text{B. } t_{1.1}, t_{1.2}, \ldots, t_{1.M_1}; \\
&\text{C. } t_{2.1}, t_{2.2}, \ldots, t_{2.M_2}; \\
&\text{D. } t_{3.1}, t_{3.2}, \ldots, t_{3.M_3} \\
&(L + M_1 + M_2 + M_3 = N).
\end{aligned} \tag{18}
$$

According to (5), the estimator for the mean working life in the stationary reloading state can be derived from

$$\hat{T}_{st} = \sum_{i=1}^{r} \hat{w}_{st}(i) \, \hat{T}[\hat{\theta}_{st}(i)], \tag{19}$$

where $\hat{w}_{st}(i) = \hat{w}_{st}[\hat{\theta}_{st}(i)]$ is the estimator for the weighting function $w_{st}(i)$.

The estimators $\hat{T}[\hat{\theta}_{st}(i)]$ are determined from (13), for which purpose the initial data of (18) are presented as a multitruncated set, as above. The values of $\theta_{st}(i)$ and the estimators $\hat{w}_{st}(i)$ are found from working observations in each distinct part of the core in the stationary reloading mode. For example, let part i of the core be observed for a time interval ΔT_i. Out of the N_i cassettes operated in this part of the core during ΔT_i, some p_i will be unloaded prematurely, while n_i will be unloaded on attaining on average the working time $\hat{\theta}_{st}(i)$. Then

$$\hat{w}_{st}(i) = \left(\frac{N_i n_i}{N_i - p_i} \frac{1}{\Delta T_i} \right) \bigg/ \sum_{j=1}^{r} \frac{N_j n_j}{N_j - p_j} \frac{1}{\Delta T_j}. \tag{20}$$

If these observations are lacking, we should use the design values for the parameters as $\hat{\theta}_{st}(i)$ and $\hat{w}_{st}(i)$. We note here that the sum of the working times A, C, and D of (18) divided by the total number is not an estimator for the mean working life of the cassettes in the stationary state.

Estimating RBMK Cassette Working Life from Data for Several Units

The statistical information on the cassette operation derived from several units may represent a sum of statistical data of different types. The range of working-life parameters to be estimated and the algorithms for calculating them are dependent on what data types occur in the initial set. The procedure for deriving estimators in that situation is basically similar to that described above, but there are some special points in certain cases.

If the initial set contains statistical information of type III, then to derive the estimators $\hat{T}_t$ it is necessary to distinguish this information out of the overall set, since the estimators $\hat{w}_t(i)$ and $\hat{\theta}_t(i)$ can be obtained only from pure statistical type III information.

If the initial overall set contains several forms of type III information (from different units), then to calculate T_t it is necessary to distinguish each of the forms. Then one determines the complete sets $\hat{\theta}_t^i(1) < \hat{\theta}_t^i(2) < \ldots < \hat{\theta}_t^i(s_i)$, where $i = \overline{1, m}$ and m is the number of forms, together with the corresponding estimators for $\hat{w}_t^i(1)$, $\hat{w}_t^i(2)$, $\ldots, \hat{w}_t^i(s_i)$.

The working times $\hat{\theta}_t^i(j)$ are arranged in increasing order, and coincident values are combined. Then one selects a complete set of characteristic (average) working times to unloading arising from burnup:

$$\hat{\theta}_t(1) < \hat{\theta}_t(2) < \ldots < \hat{\theta}_t(s), \quad s \leqslant \sum_{i=1}^{m} s_i.$$

The corresponding values of the weighting function are calculated from

$$\hat{w}_t(j) = \frac{\sum_{i=1}^{m_j} \hat{w}_t^i |\hat{\theta}_t^i(j)|}{m}, \tag{21}$$

where m_j is the number of forms whose complete sets contain $\hat{\theta}_t(j)$.

Estimating RBMK Fuel-Pin Reliability Parameters

The formulas for the mean working lives of a pin t_t and t_{st} are analogous to (15) and (19) for the corresponding cassette parameters. The estimators for the weighting functions $w_t(i)$ and $w_{st}(i)$ are identical for the cassettes and pins in the RBMK. The estimate for the reliability parameter $t(\vartheta)$ is determined from

$$\hat{t}(\vartheta) = \int_0^\vartheta \hat{P}(t)\, dt, \tag{22}$$

where $\hat{P}(t)$ is the estimator for the probability of fault-free pin operation to working time t.

The initial information for calculating this probability is provided by working data on cassette failure. The information on the cassette failures is represented as the above initial multitruncated set. The data on sealing failures in cassettes are the values of the working times to sealing failure $\tau_1' < \tau_2' < \ldots < \tau_{L'}'$, where L' is the total number of sealing-failed cassettes and $L' \geqslant L$; the values of the differing working times for the sealed cassettes are $t_1' < t_2' < \ldots < t_{M'}'$, and the corresponding set of numbers of these cassettes is m_1', m_2', $\ldots$ $m_{M'}'$, where M' is the number of differing working times, $M' \leqslant M$. The sample volume is $N = \sum_{i=1}^{M'} m_i' + L' = \sum_{i=1}^{M} m_i + L$. The latter sum contains the parameters from the initial multitruncated set, which contains information on the failed cassettes.

The point estimator for the probability of fault-free pin operation to working time t_{tp} $\hat{P}(t_{tp})$ is defined as a function of the point estimators for the probability of fault-free cassette operation $\hat{\mathscr{P}}(t)$ and the probability of maintaining sealing $\hat{R}(t)$:

$$\hat{P}(t_{tp}) = 1 - \frac{1 - \hat{\mathscr{P}}(t)}{k} - \frac{k-1}{2}\{1 - |\hat{R}(t)|^{\frac{1}{k}}\}^2. \tag{23}$$

The estimator $\hat{\mathscr{P}}(t)$ is calculated from (7), while $\hat{R}(t)$ is calculated from a formula analogous to (7) on the basis of the data set on cassette sealing failure.

458

The one-sided lower confidence bound to the probability of fuel-pin fault-free operation for a given probability β is given by

$$P_{ff}(t_{tp}) = 1 - \frac{1 - \hat{P}_{ff}(t)}{k} - \frac{k-1}{2}\{1 - [\hat{R}(t)]^{\frac{1}{k}}\}^2, \tag{24}$$

where $\hat{P}_{ff}(t)$ is the corresponding estimator for the cassette reliability parameter calculated from (8), (9), or (10).

When one performs approximate calculations, one can neglect the last terms in the above formulas and calculate the estimators $\hat{P}(t_{tp})$ and $P_{ff}(t_{tp})$ correspondingly from

$$\hat{P}(t_{tp}) = 1 - \frac{1 - \hat{P}(t)}{k};$$
$$P_{ff}(t_{tp}) = 1 - \frac{1 - \hat{P}_{ff}(t)}{k}. \tag{25}$$

Under these conditions, it is not necessary to have the initial information on the sealing failures in the cassettes, and consequently it is not necessary to calculate $\hat{P}(t)$. However, it is necessary to remember that the estimators of (25) somewhat overestimate the fuel-pin reliability in the absence of the estimators of (23) and (24).

CONCLUSIONS

These formulas for the point and interval fault-free probability estimators for RBMK cassettes and fuel pins have not been derived before, nor have the formulas for the estimators for the mean working life in terms of statistical working data, and experience with using them has shown that they are reasonably accurate and convenient in engineering applications. They have been incorporated into the sectional TSD. The formulas for estimating the mean service lives of cassettes and pins are analogous to those given for the mean working life. To derive these estimators requires one to split up the initial statistical information into several types, since the range of cassette and pin reliability parameters for the RBMK is dependent on the type of initial data available, as are the algorithms for calculating them.

LITERATURE CITED

1. N. A. Dollezhal' and I. Ya. Emel'yanov, The Channel Nuclear Power Reactor [in Russian], Atomizdat, Moscow (1980).
2. A. S. Pronikov, Machine Reliability [in Russian], Mashinostroenie, Moscow (1978).
3. Statistical Problems in Developing Systems and Tables for Numerical Calculations on Reliability Parameters [in Russian], Vysshaya Shkola, Moscow (1975).
4. L. N. Bol'shev and É. A. Loginov, "Interval estimators in the presence of interfering parameters," Teor. Veroyatn. Primen., 11, Issue 1, 94–102 (1966).

MULTIGROUP CALCULATION OF CYLINDRICAL CELLS WITH STRONGLY ABSORBING
ANNULAR REGIONS BY THE SURFACE-PSEUDOSOURCE METHOD

N. V. Sultanov   UDC 621.039.5

For multigroup calculations of reactor cells, an effective method is to factorize the operator, solving the spatial—angular part by the surface—pseudosource method, i.e., first to solve the single-group spatial—angular problems separately and then to solve the system of coupled energy equations for the zone-mean group fluxes [1-4]. Single-group kinetic equations are solved by the surface-pseudosource method in the G_N approximation, and the resulting system of algebraic equations for the moments of the surface pseudosources is solved by direct manipulation. In calculating RBMK-reactor cells with an element of the control and safety system (CSS) in which there are optically thick annular zones with a large absorption cross section, this method of solving the single-group equations proves unstable with respect to error of the approximation. Since in the given method the pseudosources of each zone are related only to the pseudosources of the neighboring zones, the matrix of the system of algebraic equations is of strip form [5]. A method of solving systems of algebraic equations which is a version of the method of matrix fitting and ensures stable calculations with respect to the error of the approximation and rounding is proposed below. In addition, the time for computer calculation is reduced: in direct manipulation of the matrix, the calculation time is proportional to M^3 (M is the dimensionality of the matrix being considered) and in manipulation of the matrix by the matrix-fitting method it is proportional to M [6].

In reactor problems, the fitting method is used to solve finite-difference equations [7] and for stable (with respect to rounding error) calculation of the cells with strongly absorbing zones in the spherical-harmonic [8] and surface-pseudosource [9] methods.

Use of Matrix Fitting to Solve Single-Group Problems

In the method of factorizing the operator from the single-group calculation, it is necessary to obtain the dependence

$$\psi = \hat{H}\mathbf{S}, \tag{1}$$

where ψ is the vector of zone-mean neutron fluxes; $\mathbf{S}$ is the vector of constant (over the zone) neutron sources and neutron currents at the external boundary of the cell; $\hat{H}$ is a matrix [1-4].

In the surface-pseudosource method, the neutron-distribution function in zone z of a cylindrical cell in the G_N approximation expanded in terms of the spherical function $Y_n^m(\Omega)$ takes the form [5]

$$\Psi^z(\rho, \Omega) = S^z/\Sigma_a^z + \sum_{j=2(z-1)}^{2z-1} \sum_{nm}^{N} \sum_{n'm'}^{N} G_{n'm'}^{nm}(\rho/\rho_j') g_{n'm'}^j Y_n^m(\Omega), \tag{2}$$

where Σ_a^z is the absorption cross section of zone z; ρ_j is the boundary radius of the j-th zone z; $G_{n'm'}^{nm}(\rho/\rho_j')$ is the angular moment of the Green's function of the kinetic equation in an infinite homogeneous medium with cross sections of the zone z at a surface of radius ρ from a source with an angular distribution $Y_{n'}^m(\Omega)$ at a surface of radius ρ_j'.

After integrating Eq. (2) with respect to all directions of the vector Ω and with respect to the volume V_z of zone z, an expression is obtained for the mean (over zone z) of the neutron flux

$$\overline{\Psi}^z = S^z/\Sigma_a^z + \frac{1}{V_z \Sigma_a^z} \sum_{\substack{j=2(z-1) \\ j'=2(z-1)}}^{2z-1} 2\pi\rho_j \sum_{n'm'}^{N} G_{n'm'}^{10}(\rho_j/\rho_{j'}') g_{n'm'}^{j'}. \tag{3}$$
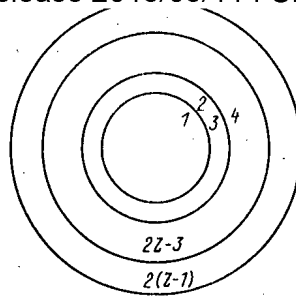
0038-531X/85/5806-0460$09.50

Fig. 1. Distribution
of zones in the cylin-
drical cell.

In Eq. (3), the zone-mean flux $\overline{\Psi}^z$ is expressed in terms of the neutron source of the given zone S^z and the surface pseudosources of zone $g_j^{j'}$. The surface pseudosources may be obtained from the condition of equality of the angular moments of the neutron distribution functions at the zone boundaries with a single-speed calculation for the whole cell. Thus, it is necessary to obtain the dependence of $\mathbf{g}$ on $\mathbf{S}$. For stable calculation of this dependence with respect to the error of the approximation, the matrix-fitting method is used.

Suppose that a cylindrical cell with Z zones is given (Fig. 1). Each zone is characterized by constant absorption and scattering cross sections and zone-constant neutron sources S^z. Taking account of Eq. (2), the condition of equality of the angular moments* at the boundary 1–2 may be written in vector-matrix form

$$\hat{A}_{23}\mathbf{g}_{23} = \hat{A}_1\mathbf{g}_1 + \hat{B}^1(S^1, S^2), \tag{4}$$

where $A_{23} = \{G^{nm}_{n'm'}(\rho_2/\rho_2'), \; G^{nm}_{n'm'}(\rho_2/\rho_3')\};$

$$\hat{A}_1 = \{G^{nm}_{n'm'}(\rho_1/\rho_1')\}; \qquad \mathbf{g}_{hl} = \begin{Bmatrix} g^h_{n'm'} \\ g^l_{n'm'} \end{Bmatrix};$$

$$\hat{B}^1 = \begin{Bmatrix} S^1/\Sigma^1_a - S^2/\Sigma^2_a \\ 0 \qquad\quad 0 \\ \vdots \qquad\quad \vdots \\ 0 \qquad\quad 0 \end{Bmatrix} \quad \begin{array}{l} n \leqslant N; \; n' \leqslant N; \\ 0 \leqslant m \leqslant n; \; 0 \leqslant m' \leqslant n'. \end{array}$$

Here and below, the following notation is used. The subscripts of the matrices and vectors correspond to the surface numbers. The numbering of the matrix rows $\hat{A}$, $\hat{C}$, is associated with change in the indices n, m, and the numbering of the columns with change in the indices n', m'. The superscripts refer either to the number of the boundary at which the angular moments of the distribution function are equal (for matrix $\hat{B}$) or to the zone number (for the variables S).

If Eq. (4) is solved relative to the unknowns $\mathbf{g}_{23}$, the matrix-convolution method is used [8]; this method is unstable relative to errors of the approximation and rounding, in particular, because the norms of the left-hand and right-hand parts of the matrix $\hat{A}_{23}$ differ by many orders of magnitude in cells with strongly absorbing (black) zones, which complicates its manipulation [9]. Therefore, Eq. (4) is brought to the form

$$\hat{A}_{12}\mathbf{g}_{12} = \hat{A}_3\mathbf{g}_3 + \hat{B}^1(S^1, S^2). \tag{5}$$

To solve Eq. (5) relative to the unknowns $\mathbf{g}_{12}$, the matrix-fitting method is used; this method is stable to errors of approximation and rounding in calculating cells with black zones [9] and, in particular, the norms of the left-hand and right-hand parts of matrix $\hat{A}_{12}$ do not differ by many orders of magnitude. Practical calculations show that the matrix-fitting method is also stable in other cases.

Solving Eq. (5), it is found that

---

*In the G_1 approximation, the angular moments of the functions $(\Omega n) \Psi (\rho, \Omega)$ are equated at the zone boundaries [10].

461

$$g_{12} = A_{12}A_{13}g_3 + A_{12}D^{\circ}(S^1, S^2).$$

The condition of equality of the angular moments of the distribution function at boundary 3–4 is then written in the form

$$\hat{C}_{23}\mathbf{g}_{23} = \hat{A}_{45}\mathbf{g}_{45} + \hat{B}^2(S^2, S^3), \tag{7}$$

where

$$\hat{C}_{23} = \{G_{n'm'}^{nm}(\rho_3/\rho_2'), \; G_{n'm'}^{nm}(\rho_3/\rho_3');$$

$$\hat{B}^2 = \begin{Bmatrix} 0 & -S^2/\Sigma_a^2 & S^3/\Sigma_a^3 \\ 0 & 0 & 0 \\ \vdots & \vdots & \vdots \\ 0 & 0 & 0 \end{Bmatrix}.$$

Substituting $\mathbf{g}_2$ from Eq. (6) into Eq. (7), it is found that

$$\hat{D}_3\mathbf{g}_3 = \hat{A}_{45}\mathbf{g}_{45} + \hat{B}^2(S^1, S^2, S^3), \tag{8}$$

where

$$\hat{D}_3 = \hat{C}_3[\hat{A}_{12}^{-1}\hat{A}_3]_2 + C_3; \tag{9}$$

$[\hat{A}_{12}^{-1}\hat{A}_3]_2$ is the lower half of the matrix $\hat{A}_{12}^{-1}\hat{A}_3$, which is referred to pseudosource $\mathbf{g}_2$ in Eq. (6)

$$\hat{B}^2(S^1, S^2, S^3) = -\hat{C}_2[\hat{A}_{12}^{-1}\hat{B}^1(S^1, S^2)]_2 + \hat{B}^2(S^2, S^3). \tag{10}$$

Equation (8) is analogous to Eq. (4) and is solved analogously. Equating the angular moments of the distribution function at the penultimate cell boundary $Z - 1$, the following equation is obtained

$$\hat{D}_{2Z-3}\mathbf{g}_{2Z-3} = \hat{A}_{2Z-2}\mathbf{g}_{2Z-2} + \hat{B}^{Z-1}(S^1, S^2, \ldots, S^Z, I), \tag{11}$$

where the matrices $\hat{D}_{2Z-3}$ and $\hat{B}^{Z-1}(S^1, S^2, \ldots, S^Z, I)$ are calculated from the recurrence formulas in Eqs. (9) and (10), respectively

$$\hat{A}_{2Z-2} = \left\{ G_{n'm'}^{nm}(\rho_{2Z-2}/\rho_{2Z-2}') - \frac{G_{10}^{n'}(\rho_{2Z-1}/\rho_{2Z-2})\,G_{as}^{nm}(\rho_{2Z-2})}{G_{as}^{10}(\rho_{2Z-1})} \right\}^*;$$

$G_{as}^{mn}(\rho) = A_n^{\circ}(\nu_0)\Phi_{n,0}^m(\rho/\nu_0)$ [5]; I is the neutron current at the external cell boundary. The matrix elements $\hat{A}_{2(Z-1)}$ are written for the condition of reflection at the external boundary of the "sink at infinity" [5]. In Eq. (11), there are as many equations as unknowns. Solving Eq. (11), an expression is obtained for the angular moments of the surface pseudosources $\mathbf{g}_{2Z-3,2Z-1}$ as a function of the neutron-source vector $\mathbf{S}$: $\mathbf{g}_{2Z-3,\,2Z-2} = \hat{E}_{2Z-3,\,2Z-2}^{-1}\,\hat{B}^{Z-1}(S^1, S^2, \ldots, I)$, where

$$\hat{E}_{2Z-3,\,2Z-2}^{-1} = \{\hat{D}_{2Z-3}, \; -\hat{A}_{2Z-2}\}.$$

The direct part of matrix fitting is complete. The inverse part of matrix fitting consists in the substitution of the known angular moments of surface pseudosources into an equation of the type in Eq. (6) in order to determine the unknown angular moments of surface pseudosources. As a result, an expression is obtained for the vector of all angular moments of the surface pseudosources $\mathbf{g}$ as a function of the constant (over the zone) neutron sources of all zones and the neutron current entering the cell through the external boundary $\mathbf{g} = \hat{U}\mathbf{S}$. Substituting this dependence into Eq. (3), the required equation — Eq. (1) — is obtained.

The matrix-fitting method used here differs from the traditional version [7] in that, in the direct and inverse parts, it is required to express the unknown pseudosources in terms of the neutron sources of all the zones $\mathbf{S}$, but, as shown by the numerical calculations below, this does not disrupt the stability of the calculation. This algorithm is realized in the RATsIYa program, which permits the calculation of cylindrical cells with annular zones containing materials with a large absorption cross section. In the old version [4], this calculation

462

TABLE 1. Initial Data for an Expanded Region with a CSS Cell

External zone radius, cm	Composition of zone	Concn. of nuclei, 10^{-24} cm^{-3}
2,52	Zr	0,042835
	Natural Hf	0,00000731
3,28	Nb *	0,0004876
	Natural B (nuclide 1011 [10])	0,0626
	C	0,0156
3,5	Zr	0,042835
	Natural HF	0,00000731
	Nb *	0,0004876
3,8	} H$_2$O	0,0334
4,1		
4,4		0,042835
	Natural HF	0,00000731
	Nb *	0,0004876
7,0	C	0,08382
14,11	Impurity *	0,00006706
24,2	C	0,08382
	Impurity *	0,00006706
25,8	O	0,0184
	H	0,0124
	^{238}U	0,00596
	^{235}U†	0,0001
31,5	C	0,08382
	Impurity *	0,00006706

*In the WIMSD program, these elements are not taken into account; they are replaced by an absorber with a 1/v absorption law.
†1.65% enrichment.

TABLE 2. Boundaries of Energy Groups

Group No.	Boundary group, eV	Group No.	Boundary group, eV
1	10,0 MeV — 9118	11	0,280 — 0,250
2	9118 — 5530	12	0,250 — 0,220
3	5530 — 906,898	13	0,220 — 0,140
4	906,898 — 9,877	14	0,140 — 0,080
5	9,877 — 4,006	15	0,080 — 0,058
6	4,006 — 1,020	16	0,058 — 0,042
7	1,020 — 0,625	17	0,042 — 0,030
8	0,625 — 0,350	18	0,030 — 0,020
9	0,350 — 0,300	19	0,020 — 0,010
10	0,300 — 0,280	20	0,010 — 0,000

TABLE 3. Absorption Cross Section of RBMK Cell with CSS Element

Constant	WIMSD				RATsIYa		
	DSN			PERSEUS	G_3 9 zones	G_3 11 zones	$\tilde{G}_3$ 11 zones
	S_4	S_8	S_{16}				
$\bar{\Sigma}_a^\delta$, cm^{-1}	0,002395 (−1,2)	0,002418 (−0,2)	0,002424	0,002442 (0,7)	0,002425 (0,05)	0,002426 (0,1)	0,002464 (1,6)
$\bar{\Sigma}_a^\tau$, cm^{-1}	0,004928 (−1,6)	0,0049995 (−0,2)	0,005011	0,004968 (−1,1)	0,005072 (1,2)	0,005029 (0,4)	0,005061 (1,0)
$\bar{\Sigma}_{Sr-\delta}$, cm^{-1}	0,005088 (0,1)	0,005084 (0,0)	0,005083	0,005190 (2,1)	0,005101 (0,4)	0,005185 (1,4)	0,005096 (0,3)
Calculation time, min	10	25	70	13	1,2	2	1,5

Note. The discrepancy between the results and the data obtained in the WIMSD—DSN program in the S_{16} approximation, %, is shown in parentheses. The calculation time is shown for the WIMSD program on an EC-1040 computer and for the RATsIYa program on a BESM-6 computer. The calculation time by the RATsIYa program is the same for the two computer.

463

was impossible because of instability of the calculation of single-group problems in solving the system of algebraic equations relative to the angular moments of surface pseudosources.

Calculation of RBMK Cells with a CSS Element

Since in RBMK cells with a CSS element there are no intrinsic neutrons, an expanded region including the given cell (of radius -p to 14.11 cm) and its immediate vicinity (up to 31.5 cm) is calculated (Table 1). The calculation of the cell in 20 groups is performed in the RATsIYa and WIMSD programs (Table 2) [12].

For the RATsIYa program, the scattering, absorption, fission, and group-transition cross sections of the neutrons and the spectra of fission neutrons are taken from the WIMSD program at 300°K. Zones with zirconium and boron are regarded as nonmoderating and nonthermalizing, and no account of transition from group to group is taken there. The scattering cross sections in these zones are determined from the formula

$$\Sigma_s^g = \sum_{g'=1}^{G} \Sigma_{sg' \to g}$$

where G is the number of groups.

Single-group calculations are performed in the G_1 and G_3 approximations, while the approximation of constant derivatives of the neutron energy current is also used; therefore, to refine the results, the water and graphite zones are divided into subzones (Table 1).

In the WIMSD program, DSN and PERSEUS routines are used. (Routines are one of several methods of solving the problem in the program.) In the DSN routine the calculations are performed in S_4, S_8, and S_{16} approximations, using the S_n method (variants of the discrete-ordinate method). The PERSEUS routine is a variant of the method of first-collision probabilities [12] (Table 3). In the thermal neutron region there are 15 groups. In calculations by the DSN and PERSEUS routines, the radius step in each zone is chosen in all approximations so that it is approximately equal to half and one neutron free path length in the group with maximum optical thickness, respectively.

The results of cell calculation in approximation G_3 (nine zones) differ from the values calculated in the S_{16} approximation by approximately 1% (Table 3) . With additional division of the water and graphite zones into subzones — see the G_3 approximation (11 zones) — this difference is reduced. In practice, the G_1 approximation may also prove acceptable (a difference of around 1%).

On the basis of the results of the comparison, it may be concluded that all the approximations used in the RATsIYa program allow the cell-mean two-group constants to be calculated with an error of approximately 1% and an acceptable calculation time for a single variant (around 2 min) on BÉSM-6 and EC-1040 computers.

Influence of Taking Account of the Incoming Neutrons on the Absorbing Characteristics of the Cells

As a rule, multigroup calculation of the CSS cells of the RBMK reactor and estimation of the constants on this basis is undertaken for the thermal energy region of a "closed" cell for which it is assumed that the integral neutron current at the external boundary is zero, and the thermal-neutron sources are distributed constantly over the zones of the cell in proportion to the moderating power of the medium $\xi\Sigma_s$.

The CSS cells of the RBMK reactor are nonbreeder cells, and therefore neutrons (mainly superthermal) enter these cells. To determine the dependence of the cell characteristics on taking account of the incoming thermal neutrons, the RATsIYa program is used. It allows the value of Σ_a^T to be calculated for the thermal region of an "open" cell, entered by neutrons through the external boundary with zero volume neutron sources. From the results of the calculation for an open cell and an expanded region, $\Sigma_a^{T,C}$ in a closed cell may be calculated from the formula

$$\Sigma_a^{T,C} = \frac{\Sigma_a^{T,E}\,\overline{\psi}^{T,E} - \Sigma_a^{T,O}\overline{\psi}^{T,O}}{\overline{\psi}^{T,E} - \overline{\psi}^{T,O}},$$

where the superscripts E and O denote the expanded region and the open cell, respectively.

464

The calculated values of the absorption cross section of the expanded region and the open and closed cells are 0.005030, 0.004216, 0.005195. The results for an open cell are less than for a closed cell by 18.8%. For the case when thermal neutrons enter the cell, the mean (over the whole cell) absorption cross section is between the data for the open and closed cells. In the given case, when the CSS cells are in the vicinity of four fuel cells with 1.65% ^{235}U enrichment, this difference is 3.2%. With increase in the current of incoming thermal neutrons in the cell, the difference increases, reaching 18.8% if all the thermal neutrons enter the cell through the external boundary.

It remains to thank N. I. Laletin for suggesting the topic and for valuable discussions.

LITERATURE CITED

1. N. I. Laletin, "Using the method of factoring the operator to spearate the energy and spatial problems in calculating the neutron distribution in a reactor cell," Vopr. At. Nauk. Tekh., Ser. Fiz. Tekh. Yad. Reakt., No. 5(18), 63-68 (1981).
2. N. V. Sultanov, "Multigroup calculation of a cylindrical cell by the surface–pseudosource method (approximation of plane derivatives of the neutron energy current)," Vopr. At. Nauk. Tekh., Ser. Fiz. Tekh. Yad. Reakt., No. 5(18), 69-76 (1981).
3. N. V. Sultanov, Multigroup Program for Calculating the Use Coefficient of Thermal Neutrons in a Multizone Cylindrical Cell (MGPRAKTINETs). Preprint IAÉ-3376/5 [in Russian], Moscow (1981).
4. N. V. Sultanov, RATsIYa Multigroup Program for Calculating a Cylindrical Cell. Preprint IAÉ-3536/5 [in Russian], Moscow (1982).
5. N. I. Laletin, "Method of surface pseudosources for solving the neutron-transfer equation (G_N approximation)," in: Methods of Calculating Thermal-Neutron Fields in Reactor Lattices [in Russian], Atomizdat, Moscow (1974), p. 187.
6. N. N. Kalitkin, Numerical Methods [in Russian], Nauka, Moscow (1978).
7. G. I. Marchuk and V. I. Lebedev, Numerical Methods in Neutron-Transfer Theory [in Russian], Atomizdat, Moscow (1981).
8. V. E. Raevskii and B. Z. Torlin, "Matrix-fitting method for calculating a complex lattice in the P_S approximation," At. Énerg., 49, No. 5, 310-311 (1980).
9. N. V. Sultanov, Single-Speed Calculation of Cylindrical Cells of Strongly Absorbing Annular Zones. Preprint IAÉ-3988/4 [in Russian], Moscow (1984).
10. N. I. Laletin and N. V. Sultanov, "Development of the surface-pseudosource method for calculating neutron fields in cells with a fuel-rod assembly," At. Énerg., 46, No. 3, 148-154 (1979).
11. N. V. Sultanov and I. A. Zhokina, "Refinement of the boundary conditions in calculating 'close' lattices by the surface-pseudosource method," At. Énerg., 53, No. 3, 155-157 (1982).
12. J. Askew, F. Fayers, and P. Kemshell, "A general description of the lattice code WIMS," J. BNES, 4, No. 4, 564 (1966).

MULTIGROUP CALCULATION OF CLUSTER CELLS BY THE
SURFACE-PSEUDOSOURCE METHOD

N. V. Sultanov   UDC 621.039.52

The method of operator factorization for separating the energy and spatial—angular problems is useful in the multigroup calculation of neutron distributions in a cylindrical reactor cell [1-5]. In [2-5], the spatial—angular part of the problem was solved by the surface-pseudosource method, assuming constant neutron energy current through the zone. This is less approximate than the assumption that the neutron fluxes through the zone are constant, which is the assumption made in the metod of first-collision probability, so that the step over the spatial variable may be increased and the time of computer calculation may be reduced [1-5].

The present work is devoted to applying the method of operator factorization with solution of the spatial—angular part of the problem by the surface-pseudosource method for rapid calculation of cluster cells with sufficient accuracy.

Application of the Factorization Method for Multigroup Calculation of Cluster-Type Cells

Each zone of a cluster cell (Fig. 1) is characterized by a constant (over the zone) differential cross section of scattering from group go to group g', $\Sigma_s^{g \to g'}$, absorption Σ_a^g, and fission Σ_f^g (in the calculations, it is usual to take $\Sigma_s^{g \leftarrow g}$ in the transport approximation). The eigenvalue k_∞ inside the cell is obtained by solving the multigroup kinetic equation

$$\Omega\nabla\Psi^g(\mathbf{r}, \Omega) + \Sigma_t^g(\mathbf{r})\Psi^g(\mathbf{r}, \Omega) = \sum_{g'=1}^{G} \Sigma_s^{g \leftarrow g'}(\mathbf{r})\Psi_0^{g'}(\mathbf{r}) + \frac{\chi^g(\mathbf{r})}{k_\infty}\sum_{g'=1}^{G} \nu\Sigma_f^{g'}(\mathbf{r})\Psi_0^{g'}(\mathbf{r}), \tag{1}$$

where $\psi^g(\mathbf{r}, \Omega)$ is the distribution function of group-g neutrons; $\Psi_0^g(\mathbf{r}) = \int_{4\pi}\Psi^g(\mathbf{r}, \Omega)\,d\Omega$; $\chi^g(\mathbf{r})$

is the spectrum of fission neutrons; G is the number of groups.

At the external cell boundary, where the integral neutron current is zero, the condition of a "sink at infinity" [6] or the condition of an "isotropic sink" [7] is used. In the latter case, the results of the calculation are the same as in isotropic reflection. In calculating square and hexagonal lattices, the condition of a "combined source" is used; the results obtained here are close to those obtained with the condition of mirror reflection of neutrons. The zone-mean group neutron fluxes, the neutron group fluxes and currents at the zone boundaries, and k_∞ of the cell are determined from Eq. (1).

Equation (1) may be transformed to an equivalent system of two equations [1]

$$\begin{cases} \Omega\nabla\Psi^g(\mathbf{r}, \Omega) + \Sigma_t^g(\mathbf{r})\Psi^g(\mathbf{r}, \Omega) = \Sigma_{s,0}^g(\mathbf{r})\Psi_0^g(\mathbf{r}, \Omega) + S^g(\mathbf{r}); \tag{2} \\ \\ S^g(\mathbf{r}) = \frac{dQ^g(\mathbf{r})}{dE} + S_f^g(\mathbf{r}) = \sum_{g'=1}^{G} \Sigma_s^{g \leftarrow g'}(\mathbf{r})\Psi_0^{g'}(\mathbf{r}) - \Sigma_{s,0}^g(\mathbf{r})\Psi_0^g(\mathbf{r}) + \frac{\chi^g(\mathbf{r})}{k_\infty}\sum_{g'=1}^{G} \nu\Sigma_f^{g'}(\mathbf{r})\Psi_0^{g'}(\mathbf{r}), \tag{3} \end{cases}$$

where $Q^g(\mathbf{r})$ is the neutron current along the energy axis; $c(r) = 1$ [1].

Equation (2) determines the diffusion of group-g neutrons in the cell (group number g appears in the equation as a parameter) and Eq. (3) determines the transition of neutrons from

---

to another. The eigenvalue of Eqs. (2) and (3) k_∞ is sought by the method of iteration with respect to the source: in the n-th iteration, $S_f^g(\mathbf{r})$ is assumed to be known and equal to

$$\frac{\chi^g(\mathbf{r})}{k_\infty^{(n-1)}} \sum_{g'=1}^{G} \nu\Sigma_f^{g'}(\mathbf{r}) \Psi_0^{g'(n-1)}(\mathbf{r}),$$

where $\psi_0^{g(n-1)}$ is the group flux determined from the $(n-1)$-th iteration. Then in each iteration there is a problem with external neutron sources, which is solved by the method of factorizing the operator and solving the spatial—angular part of the problem by the surface-pseudosource method.

After integrating Eq. (3) over the zone volume, an equation in terms of the zone-mean group neutron fluxes is obtained. Thus, the basic approximations are the approximations of constant (in each zone z) derivatives of the neutron energy current $dQ^g(\mathbf{r})/dE = dQ_z^g/dE$ and sources of fission neutrons $S_f^g(\mathbf{r}) = S_{f, z}^g$. The equation for the "plane" source of zone z in the n-th iteration for group g takes the form

$$S_z^{g(n)} = \sum_{g'=1}^{G} \Sigma_{s, z}^{g \leftarrow g'} \overline{\Psi}_{0, z}^{g'(n)} - \Sigma_{s, 0, z}^{g} \overline{\Psi}_{0, z}^{g(n)} + \frac{\chi_z^{g'}}{k_\infty} \sum_{g'=1}^{G} \nu\Sigma_{f, z}^{g'} \overline{\Psi}_{0, z}^{g(n-1)}, \tag{4}$$

where $\overline{\psi}_{0, z}^{g(n)}$ is the mean (over zone z) flux of neutrons of the given group.

After substituting Eq. (4) into Eq. (2) and solving the result by the surface-pseudosource method, the zone-mean group neutron fluxes may be expressed in terms of the neutron sources $\mathbf{S}$ by the formula

$$\overline{\Psi} = \hat{H}\mathbf{S}, \tag{5}$$

where $\overline{\Psi} = \{\overline{\psi}_z^g\}$ is the vector of mean neutron fluxes of zone z $(z \leqslant Z)$ and group g $(g \leqslant G)$; Z is the number of zones; $\mathbf{S} = \{S_z^{S_i^g}\}$ is the vector of neutron sources S_z^g of zone z and neutron currents at the external boundary of the cell I^g of group g; H is a matrix whose elements are combinations of the angular moments of the Green's function.

In the equation, the part of the source associated with fission neutrons takes the form

$$\overline{\Psi}^{(n)} = \hat{H}\mathbf{S}_0^{(n)} + \frac{1}{k_\infty^{(n-1)}} \hat{H}\chi^{(n-1)}, \tag{6}$$

where

$$\{\chi\}^{z, g} = \chi_z^g \sum_{g'=1}^{G} \nu\Sigma_{fz}^g \overline{\Psi}_{0, z}^{g(n-1)}; \quad \mathbf{S}_0 = \frac{dQ}{dE}.$$

Equation (6) is a brief form of the iterative process for determining k_∞. In the zero iteration, the mean flux in all the zones and groups is taken to be unity. Iteration continues as long as $|k_\infty^n/k_\infty^{n-1} - 1| < \varepsilon = 10^{-4}$. In the subsequent iterations, an additional condition for checking the convergence of the flux appears

$$\max |\overline{\Psi}_z^{(n)g}/\overline{\Psi}_z^{g(n-1)} - 1| < \varepsilon_1 = 10^{-3}. \tag{7}$$

The maximum is determined over the whole set of zones and groups. Calculations of RBMK cluster cells (Fig. 1) show that this iterative process converges after three to five iterations. After convergence of the iterations with respect to k_∞ and the fluxes, the neutron fluxes and currents at the zone boundaries are determined.

In the assumptions adopted, the method of operator factorization allows all the single-group spatial—angular problems — Eq. (2) for each group — first to be solved and then the energy problem in Eq. (3) to be solved.

Application of the Matrix-Fitting Method in the Single-Group Problem

In the cluster cell, two types of zone may be distinguished: cylindrical with one or two cylindrical surfaces and cluster cylindrical with internal blocks. The matrix-fitting method for calculating cylindrical zones was described in [5]. Below it is presented for cluster zones.
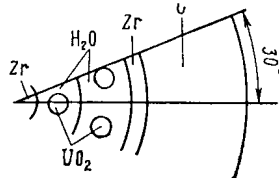
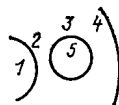Fig. 1. Cluster cell of RBMK reactor.

Fig. 2. Cluster zone.

In the surface-pseudosource method, the neutron distribution function in the G_N^P approximation [8, 9] for a cluster zone takes the form

$$\Psi^z(\mathbf{r}, \Omega) = S^z/\Sigma_a^z + \sum_{j=2}^{4} \sum_{pnm} \sum_{p'n'm'}^{PN} G_{n'm'p'}^{nmp}(\rho/\rho_j') \, g_{n'm'p'}^{j} \left\{ \begin{matrix} \cos p\alpha \\ \sin p\alpha \end{matrix} \right\} Y_n^m(\Omega), \qquad (8)$$

where Σ_a^z is the absorption cross section of zone z; j is the number of the surface of zone z (Fig. 2); $G_{n'm'p'}^{nmp}(\rho/\rho')$ are the angular and spatial moments of the Green's function of the kinetic equation in an infinite homogeneous medium with cross sections of zone z at the surface (radius ρ) of the source with a spatial distribution $\left\{ \begin{matrix} \cos p'\alpha \\ \sin p'\alpha \end{matrix} \right\}$ and angular distribution $Y_{n'}^{m'}(\Omega)$ positioned at the surface of radius ρ'.

Writing the equation expressing the equality of the angular moments of the distribution function in Eq. (8) at the boundary 1–2, it is transformed to give

$$\hat{A}_{12}g_{12} = \hat{A}_3 g_3 + \hat{A}_4 g_4 + \hat{B}^1(S^1, S^2), \qquad (9)$$

where

$$\hat{A}_{12} = \{G_{n'm'}^{nm}(\rho_1/\rho_1'), \ -G_{n'm'}^{nm}(\rho_2/\rho_2')\}; \qquad \hat{A}_3 =$$
$$= \{G_{n'm'p'}^{nm}(\rho_2/\rho_3')\}; \ \hat{A}_4 = \{G_{n'm'}^{nm}(\rho_4/\rho_4')\};$$

$$g_{kl} = \left\{ \begin{matrix} g_{n'm'p'}^{h} \\ \vdots \\ g_{n'm'p'}^{l} \end{matrix} \right\};$$

$$\hat{B}^1 = \left\{ \begin{matrix} -S^1/\Sigma_a^1 & S^2/\Sigma_a^2 \\ 0 & 0 \\ \vdots & \vdots \\ 0 & 0 \end{matrix} \right\} \begin{matrix} n \leqslant N; \ n' \leqslant N; \\ 0 \leqslant m \leqslant n; \ 0 \leqslant m' \leqslant n'; \\ 0 \leqslant p \leqslant P; \ 0 \leqslant p' \leqslant P. \end{matrix}$$

Here and below, the following notation is used: the subscripts of the matrices and vectors refer to the number of the surfaces (Fig. 2). The numbering of the matrix rows of type $\hat{A}$, $\hat{C}$, $\hat{D}$ is associated with the change in the indices p, n, m and the number of the columns with the change in the indices p', n', m'. The superscripts refer either to the number of the boundary at which the moments of the distribution functions are equated (for matrix $\hat{B}$) or to the number of the zone (for variables S).

Solving Eq. (9) gives

$$g_{12} = \hat{A}_3' g_3 + \hat{A}_4' g_4 + \hat{B}^1(S^1, S^2), \qquad (10)$$

where $\hat{A}_3' = \hat{A}_{12}^{-1}\hat{A}_3$; $\hat{A}_4' = \hat{A}_{12}^{-1}\hat{A}_4$; $\hat{B}^{1'} = \hat{A}_{12}^{-1}\hat{B}^1$. Equating the spatial and angular moments of the neutron distribution functions at the boundary with the block, the following relation is obtained

468

$$D_{35}g_{35} = D_2 g_2 + D_4 g_4 + B^0 (S^2, S''),$$

(11)

where $\hat{D}_{35} = \{-G_{n'm'p}^{nmp}, (\rho_3/\rho_3'), \ G_{n'm'p}^{nmp}, (\rho_5/\rho_5')\}; \ \hat{D}_2 = \{G_{n'm}^{nmp}, (\rho_3/\rho_2')\};$ and

$$\hat{D}_4 = \{G_{n'm'}^{nmp}(\rho_3/\rho_1')\}; \ \hat{B}^\delta = \begin{Bmatrix} 0 & S^2/\Sigma_a^2 & -S^\delta/\Sigma_a^\delta \\ 0 & 0 & 0 \\ \vdots & \vdots & \vdots \\ 0 & 0 & 0 \end{Bmatrix}.$$

Substituting g_2 from Eq. (10) into Eq. (11), it is found that

$$\hat{D}_{35}'' g_{35} = \hat{D}_4'' g_4 + \hat{B}^{\delta''} (S', S^2, S^\delta).$$

(12)

where $\hat{D}_{35}'' = \{\hat{D}_3 - \hat{D}_2 [A_3']_2, \ \hat{D}_5\}; \ D_4'' = \hat{D}_4 + \hat{D}_2 [A_4']_2; \ \hat{B}^{\delta''} = \hat{B}^\delta + \hat{D}_2 [B^{1'}]_2; [\hat{A}_4']_2$ is the lower half of matrix A_4, which pertains to vector g_2 in Eq. (10). Solving Eq. (12), it is found that

$$g_{35} = D_4' g_4 + \hat{B}^{\delta'} (S^1, S^2, S^\delta),$$

(13)

where $\hat{D}_4' = (\hat{D}_{35}'')^{-1}\hat{D}_4''; \ \hat{B}^{\delta'} = (\hat{D}_{35}'')^{-1}\hat{B}^{\delta''}$

Equating the angular moments of the neutron distribution function at the boundary of the second cluster zone, the vector—matrix equation

$$\hat{C}_2 g_2 + \hat{C}_3 g_3 + \hat{C}_4 g_4 = \hat{A}_6 g_6 + \hat{A}_7 g_7 + \hat{A}_8 g_8 + \hat{B}^2 (S^2, S^3),$$

(14)

is obtained; here the elements of matrix $\hat{C}$ take the form of the elements of matrix $\hat{A}$, replacing the radius ρ_2 by ρ_4. Eliminating g_2 and g_3 from Eq. (14) — substituting their values from Eqs. (10) and (13) — it is found that

$$\hat{C}_4'' g_4 = \hat{A}_6 g_6 + \hat{A}_7 g_7 + \hat{A}_8 g_8 + \hat{B}^{2''} (S^1, S^2, S^3, S^\delta),$$

(15)

where $\hat{C}_4'' = \hat{C}_4 + \hat{C}_2 [\hat{A}_4']_2 + \{\hat{C}_3 + \hat{C}_2 [\hat{A}_3']_2\}[\hat{D}_4']_3; \ \hat{B}^{2''} = \hat{B}^2 - \hat{C}_2\hat{B}^{1'} - \{\hat{C}_3 + \hat{C}_2[A_3']_2\}\hat{B}^{\delta'}$. Equation (15) is analogous to the initial Eq. (9). If a cylindrical zone follows the cluster zone, Eq. (15) takes the form

$$\hat{C}_4'' g_4 = \hat{A}_6 g_6 + \hat{A}_7 g_7 + \hat{B}^{2''} (S^1, \ S^2, \ S^3, \ S^\delta).$$

(16)

Equation (16) is analogous to the initial equation for a cylindrical cell. The next zone may be calculated either from Eqs. (9)–(15) or from the formula of [5]. Thus, the direct part of the matrix-fitting method is realized.

In the inverse part of the matrix-fitting method, the moments of the surface pseudosources may be determined either from Eqs. (10) and (13) or from the formulas of [5]. As a result, the dependence of all the surface-pseudosource moments on zone-constant neutron sources and on the neutron current entering through the external boundary is obtained [5]

$$g = \hat{U} S.$$

(17)

After integrating Eq. (8) over all directions of the vector Ω and over the whole volume V_z of cluster zone z, an expression is obtained for the mean (over zone z) neutron flux

$$\overline{\Psi^z} = S^z/\Sigma_a^z + \frac{1}{V_z \Sigma_a^z} \sum_{\substack{j=2 \\ j'=2}}^{4} 2\pi\rho_j \sum_{p'n'm'}^{PN} G_{n'm'p'}^{10} (\rho_j/\rho_j') g_{n'm'p'}^{j'}.$$

(18)

After substituting the dependence of $g_{n'm'p'}^{j'}$ from Eq. (17) into Eq. (18), the required Eq. (5) is obtained.

On the basis of this algorithm, the KLARA multigroup program for calculating cells of cluster type is written, solving the single-group kinetic problems by a modified PRAKTINEK program [8, 9]. Using the algorithm of the KLARA program, the energy problem for decelerating neutrons is calculated by successive solution of the equations [4] and in the region of thermalization of the neutrons by combined solution of all the single-group equations [3].
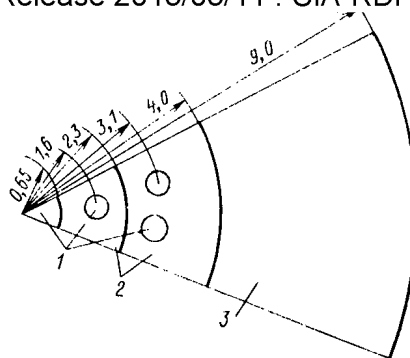
469

Fig. 3. Symmetry element of cluster cell: 1) uranium block of diameter 1.3 cm; 2) water; 3) graphite.

The use of the given method reduces the time for computer calculation by half in comparison with the direct solution of the system of equations following from the equation of the moments of the neutron distribution functions. The stability of the calculation relative to errors of the approximation and rounding for optically thick zones may evidently be proven analytically, as for cylindrical cells in [10]. In the remaining cases, the stability is established by comparison of numerical results.

Calculation of Cluster Cells

To determine the accuracy and time of computer calculation from the KLARA program, the results of calculation for cluster cells of RBMK type by the KLARA, PIT [11], and WIMSD4 [12] programs are compared.

First, the energy range 0-0.9 eV is investigated. Consider the cluster cell in Fig. 3, which is regarded as "closed": neutrons enter the cell from the moderation region with an intensely proportional to the moderating power of the medium $\xi \Sigma_s$, with zero integral neutron currents at the external boundary.

Calculation by the KLARA program is performed in 40 groups. The scattering, absorption, and group-transition cross sections are taken from the PIT program at a temperature 300°K of the medium. Water is considered in the gas approximation and graphite is considered taking its crystalline structure into account. The group-transition cross sections are determined in the transport approximation

$$\Sigma_{s,t,r}^{g \leftarrow g'} = \Sigma_{s,0}^{g \leftarrow g'} (1 - \overline{\mu}_{g'}).$$

The error in calculating the small-group constants is less than 1%.

In the PIT program, double differential scattering cross sections depending continuously on the angles and the energy are used in the transport approximation

$$\Sigma_s (E' \rightarrow E, \mu) = \frac{1}{4\pi} \Sigma_{s,0} (E' \rightarrow E) [1 - \overline{\mu} (E') + 2\overline{\mu} (E') \delta (1 - \mu)]$$

(Tables 1 and 2).

Another method of testing the KLARA program is to calculate k_∞ of the RBMK cell (Fig. 1, Table 3). Calculations are performed in 20 groups; the boundaries of the energy groups are given in [5]. After multigroup calculation, the two-group constants of the whole cell are determined (Table 4). The calculations are performed in the KLARA (in the $\tilde{G}_1^0$-, G_3^0-, G_1^1- and $\tilde{G}_3^1$- approximations of the surface-pseudo source method), WIMSD4 (according to the DSN, PIJ + PERSEUS, and PERSEUS routines), and RATsIYa programs [4]. The multigroup cross sections of neutron transition from group to group, absorption, fission, and the fission neutron spectrum for the KLARA and RATsIYa programs are taken from WIMSD4 program at a temperature of the medium of 300°K.

Homogenization of the cluster zones is used in calculating the cluster cell in the RATsIYa program [3, 13].

TABLE 1. Initial Data for Calculating RBMK Cluster Cells

Element	Nuclear concn., 10^{-24} cm^{-3}
^{235}U	0,000526
^{238}U	0,0263
H_2O	0,0334
C	0,0836

TABLE 2. Integral Characteristics of a Thick RBMK Cell

Parameter	PIT	KLARA *	
		version 1	version 2
$\overline{\Sigma}_a$	$0,03035(1\pm0,35\cdot10^{-2})$	0,03027 (−0,26)	0,03019 (−0,53)
$\overline{\nu\Sigma}_f$	$0,4571(1\pm0,35\cdot10^{-2})$	0,4557 (−0,33)	0,4544 (−0,59)
Θ†	0,93082	0,92951 (−0,14)	0,92941 (−0,15)

*The discrepancy between these values and results of PIT calculations is shown in parentheses, %. In version 1, the water zone is considered as a whole; in version 2, it is divided into two subzones. Neutrons in the fuel neither gain nor lose energy.

†θ is the use coefficient of the thermal neutrons.

TABLE 3. Initial Data for Calculating k_∞ of an RBMK Cell

Zone material	Zone composition	Zone radius, cm	Nuclear concn. in zones, 10^{-24} cm^{-3}
Zr (rod)	Zr	0,75	0,04283
	Hf		0,00000731
	Nb *		0,0004876
H_2O	H	2,3	0,0668
UO_2	O	4,0	0,0334
	O	0,68	0,04036
	^{238}U	1,6† 3,09†	0,02003
	^{235}U		0,000409
Zr (tube)	Zr	4,4	0,04209
	Hf		0,00000731
	Nb *		0,001219
C	C	14,11	0,08382
	Impurity *		0,00006706

*In the WIMSD program these elements are not taken into account; they are replaced by an absorber of given concentration with a 1/v absorption law.

†Radius of block center, cm.

471

TABLE 4. Small-Group Constants of RBMK Cluster Cell

Constant	KLARA				RATsIYa		WIMSD4			
	$\widetilde{G}_1^0$	G_1^0	$\widetilde{G}_1^1$	G_3^1	$\widetilde{G}_1$	G_3	PIJ	DSN S_1	DSN S_8	PERSEUS
k_∞	1,2794 (—1,4)	1,2809 (—1,2)	1,2968 (—0,02)	1,2971	1,2965 (—0,05)	1,2963 (—0,06)	1,3000 (0,2)	1,2967 (—0,03)	1,2978 (0,05)	1,2977 (0,1)
$\overline{\Sigma}_a^T$, cm^{-1}	0,004269 (—8,3)	0,004246 (—8,8)	0,004583 (—1,5)	0,004654	0,004690 (0,7)	0,004676 (0,4)	0,004708 (1,2)	0,004608 (—1,0)	0,004643 (—0,2)	0,004629 (—0,5)
$\overline{\Sigma}_a^\delta$, cm^{-1}	0,001298 (0,5)	0,001295 (0,3)	0,001222 (—5,3)	0,001291	0,001295 (0,3)	0,001295 (0,3)	0,001299 (0,6)	0,001296 (0,4)	0,001290 (0,1)	0,001293 (0,2)
$\overline{\nu\Sigma}_f^T$, cm^{-1}	0,006138 (—9,4)	0,006099 (—10,0)	0,006663 (—1,6)	0,006775	0,006834 (0,9)	0,006813 (0,6)	0,006872 (1,5)	0,006700 (—1,1)	0,006757 (—0,3)	0,006736 (—0,6)
$\overline{\nu\Sigma}_f^\delta$, cm^{-1}	0,0007544 (2,4)	0,0007751 (0,3)	0,007002 (—9,4)	0,0007731	0,0007517 (—2,8)	0,0007517 (—2,8)	0,0007741 (0,1)	0,0007786 (0,7)	0,0007740 (0,1)	0,0007786 (0,7)
$\overline{\Sigma}_{ST\leftarrow\delta}$, cm^{-1}	0,005738 (0,8)	0,005694 (0,02)	0,005633 (—1,0)	0,005693	0,005777 (1,6)	0,005777 (1,6)	0,005737 (0,8)	0,005729 (0,7)	0,005729 (0,7)	0,005726 (0,6)
Count time, min	1,1	2,5	1,4	3,2	1	2	110	3	7	3,0

Note. The figures in parentheses are the discrepancy from the results of calculation G_3^1 approximation by the KLARA program, %. For the KLARA and RATsIYa programs, the count time given corresponds to a BÉSM-6 computer and for the WIMSD-4 program to an EC-1040 computer. The count time in the RATsIYa program on BÉSM-6 and EC-1040 computers is the same.

In calculation by the PIJ sample, detailed division of all the zones into subzones with a sufficiently large number of grid points in calculating the probabilities is undertaken. Calculations of the RBMK cluster cell using the homogenization method are performed in the DSN (in the S_N approximation) and PERSEUS (using a version of the first-collision-probability method) samples [12].

The results of calculations by the KLARA program converse with increase in the approximation. To obtain sufficient accuracy for practical purposes in the small-group constants (around 1%), account must be taken of the first axial G_1^1 approximation and those of the G_3^1 approximation in the region of fast-neutron energies for $\overline{\Sigma}_a^\delta$ and $\overline{\nu\Sigma}_f^\delta$ remains to be elucidate.

Calculations of the cluster cell by the RATsIYa (in the G_1 and G_3 approximations) and KLARA (in the G_3^1 approximation) programs and also by the DSN (in the S_4 and S_8 approximations), PERSEUS, and PIJ routines lead to deviations of approximately 1% in the small group constants, which is acceptable in practice.

It remains to thank N. I. Laletin for discussion of the present work and valuable comments and also L. V. Maiorov for kindly furnishing the calculations by the PIT program.

LITERATURE CITED

1. N. I. Laletin, "Use of the operator factorization method for separating the energy and spatial problems in calculating the neutron distribution in the reactor cell," Vopr. At. Nauk. Tekh., Ser. Fiz. Tekh. Yad. Reakt., No. 5(18), 63-68 (1981).
2. N. V. Sultanov, "Multigroup calculation of reactor cells using the surface-pseudosource method (approximation of plane derivatives of the energy current)," Vopr. At. Nauk. Tekh., Ser. Fiz. Tekh. Yad. Reakt., No. 5(18), 69-76 (1981).
3. N. V. Sultanov, Multigroup Program for Calculating the Use Coefficient of Thermal Neutrons in a Multizone Cylindrical Cell (MGPRAKTINETs). Preprint IAÉ-3376/5 [in Russian], Moscow (1981).
4. N. V. Sultanov, Ratsiya Multigroup Program for Calculating a Cylindrical Cell. Preprint IAÉ-3536/5 [in Russian], Moscow (1982).
5. N. V. Sultanov, "Multigroup calculation of cylindrical cells with strongly absorbing annular zones by the surface-pseudosource method," At. Énerg., 58, No. 6, 410-413 (1985).
6. N. I. Laletin, "Surface-pseudosource methods for solving neutron-transfer equations (G_N approximation)," in: Methods of Calculating Thermal-Neutron Fields in Reactor Grids [in Russian], Atomizdat, Moscow (1974), pp. 187-214.

7. N. V. Sultanov and I. A. Zhokina, "Refining the boundary conditions in calculating 'dense' lattices by the surface-pseudosource method," At. Energ., 53, No. 3, 155-157 (1982).
8. N. I. Laletin and N. V. Sultanov, "Development of the surface-pseudosource method for calculating the neutron fields in cells with a fuel-rod assembly," At. Energ., 46, No. 3, 148-154 (1979).
9. N. V. Sultanov, Development of the Surface-Pseudosource Method for Calculating the Neutron Fields in RBMK Cells. Preprint IAÉ-3005 [in Russian], Moscow (1978).
10. N. V. Sultanov, Single-Speed Calculation of Cylindrical Cells with a Strongly Absorbing Annular Zone. Preprint IAÉ-3988/4 [in Russian], Moscow (1984).
11. A. S. Kaminskii and L. V. Maiorov, "PIT program for calculating slow-neutron fluxes by the Monte Carlo method, taking account of thermalization," Vopr. At. Nauk Tekh., Ser. Fiz. Tekh. Yad. Reakt., No. 8(21), 76-77 (1981).
12. J. Askew, F. Fayers, and P. Kewshell, "A general description of the lattice code WIMS," J. BNES, 5, No. 4, 564 (1966).
13. Yu. P. Elagin, A. S. Il'yashenko, V. A. Lyul'ka, et al., "Calculations of RBMK cells by various methods," At. Energ., 48, No. 3, 148-151 (1980).

STEADY PRESSURE OF HYDROGEN IN A SODIUM CIRCUIT WITH COLD TRAP

G. P. Sergeev and V. M. Makarov

In sodium circuits, sodium traps are used as the principal means of purifying the sodium from impurities. By this means, the removal of impurities dissolved in the sodium takes place in consequence of their crystallization in the volume of the trap at a lower temperature than the temperature of the circuit. Usually, the operating regime of the cold trap is defined by the flow rate through it of the sodium and its temperature at the outlet from the trap. During operation of the cold trap (in the case of ideal mixing in the circuit, the absence of suspended matter dissolved in the sodium and chemical interaction between the impurities) the steady value of the concentration of any impurity in the circuit is determined by the expression

$$C_s = C^{ex} + \frac{q \cdot 10^6}{G},$$ (1)

where G is the sodium flow rate through the trap, tons/h; q is the intensity of the impurity source, tons/h; C_s is the steady concentration of impurity in the circuit, ppm; C^{ex} is the impurity concentration at the outlet from the trap, ppm.

For sodium containing dissolved impurities which react chemically with one another, expression (1) is not valid. Thus, if hydrogen, oxygen, and sodium hydroxide are present in the dissolved state in the sodium (this occurs, for example, during operation of the cold trap, by the buildup of the reaction products of water with the sodium), then on the assumption of other reactions between them of the type

$$2Na + NaOH_p \rightleftharpoons Na_2O_p + NaH_p$$ (2)

with a large quantity of sodium the equations for steady values of the concentrations of these impurities have the following form:

$$\frac{G}{M}(X_H^{ex} - X_H) + K_1 X_{OH} - K_2 X_H X_O + 2q_H = 0;$$

$$\frac{G}{M}(X_O^{ex} - X_O) + K_1 X_{OH} - K_2 X_H X_O + 2q_O = 0;$$ (3)

$$\frac{G}{M}(X_{OH}^{ex} - X_{OH}) - K_1 X_{OH} + K_2 X_H X_O + q_{OH} = 0,$$

where X_H, X_O, X_{OH} and X_H^{ex}, X_O^{ex}, and X_{OH}^{ex} are the molar concentrations of hydrogen, oxygen, and sodium hydroxide in the circuit and at the outlet of the cold trap; q_H, q_O, and q_{OH} is the

---

inte... of generation of hydrogen, oxygen, and sodium hydroxide in the circuit, ton/... ; M, mass of a mole of sodium, ton/mole; K_1 and K_2, velocity constants of the forward and reverse interaction reactions (2) between the components of the solution.

It follows from Eq. (3) that in the general case, steady concentrations of hydrogen, oxygen, and sodium hydroxide dissolved in the sodium depend not only on the concentration of these impurities at the outlet from the cold trap and the intensity of their generation, but also on the interaction kinetics of the impurities in the solution.

With the presence in the circuit only of a source of hydrogen, the maximum error in the determination of the steady concentration of this element in the circuit due to not taking account of the kinetics of reaction (2), can be estimated in the following way. According to relations (3), if $q_O = q_{OH} = 0$ and K_1/K_2 is independent of temperature [1], then the maximum value of the quantity

$$A_1 = (K_2 X_H X_O - K_1 X_{OH}) \tag{4}$$

cannot be greater than

$$A_2 = X_O^{ex} G/M. \tag{5}$$

Substituting expression (5) in the first of Eqs. (3), in place of the inequality (4) we obtain

$$X_H = X_H^{ex} - X_O^{ex} + \frac{2q_H M}{G}. \tag{6}$$

Without consideration of reaction (2), the steady concentration of hydrogen in the circuit should be determined by the expression

$$X_H = X_H^{ex} + \frac{2q_H M}{G}. \tag{7}$$

As it follows from expressions (6) and (7), the maximum error in the estimate of X_H, without taking account of reaction (2), cannot exceed the value of X_O^{ex}.

The steady concentration of hydrogen in the sodium of the secondary circuit determines the background level of the signal from the detector of sodium-water leakage from the steam generator, which monitors the hydrogen in the sodium. The operating lifetime of the leak detectors with the magnetodischarge pumps, as well as with the measurement transducers of the detectors, depend on the level of this background hydrogen. The hydrogen background level and its stability, to a considerable degree also affects the actual sensitivity of the detector — the minimally detectable leakage of water into the sodium in the sodium-water steam-generator. Therefore, it is desirable to estimate this background level a priori. These estimates can be made on the basis of Eqs. (6) and (7) if the values of X_H^{ex}, X_O^{ex}, and q_H are known. On the other hand, monitoring the concentration of hydrogen in the sodium of the secondary circuit with detectors calibrated on hydrogen for known values of X_H^{ex} and X_O^{ex}, allows the intensity of the hydrogen generation in the circuit to be estimated. The main source of hydrogen in sodium circuits with sodium-water steam generators is corrosion, as a result of which hydrogen is formed and it appears in the tertiary (steam-water) circuit and enters the secondary circuit in consequence of diffusion through the walls of the heat exchange surfaces of the steam generator.

Usually, X_H^{ex} is estimated as the saturation concentration (solubility) of hydrogen in the sodium, for a temperature of the sodium at the outlet from the cold trap. For this, data about the solubility of hydrogen in sodium are used, or the reaction products of water with sodium. Marked differences are observed between these data, obtained by different authors. In particular, this concerns the temperature dependence of the solubility of hydrogen in sodium.

In this paper, the results are presented of experiments to determine the conditions for which the concentration of hydrogen in the sodium at the outlet from the cold trap corresponds to the solubility at this temperature, and to verify and refine the coefficient characterizing the dependence of the solubility of hydrogen in the sodium on the temperature.

It is well known that the solubility of hydrogen in sodium as a function of the temperature can be determined by an equation of the following form [1]:

$$\lg C_s = \frac{A}{T} + B, \tag{8}$$

474

where C_s is the solubility of hydrogen in the sodium, ppm, T is the temperature of the sodium, °K, and A and B are constants.

It was established also that solutions of hydrogen in sodium at concentrations less than the saturation concentration are subject to Sievert's law, i.e., the concentration of hydrogen in the sodium is related with the equilibrium pressure of hydrogen above the solution by the relation

$$C = K\sqrt{p}, \tag{9}$$

where C is the concentration of hydrogen in the sodium, ppm; K is Sievert's constant, and p is the equilibrium pressure of hydrogen above the sodium, Pa.

In the investigations of solutions of hydrogen in sodium, no significant temperature effect was detected on the Sievert constant in the range 120–500°C, and therefore it can be assumed to be independent of the temperature in this range.

For a saturated solution of hydrogen in sodium, taking account of expression (8), relation (9) assumes the form

$$\lg p_s = A_0/T + B_0, \tag{10}$$

where p_s is the hydrogen pressure above the saturated solution of hydrogen in the sodium at the temperature T;

$$\begin{aligned} A_0 &= 2A; \\ B_0 &= 2B - 2\lg K. \end{aligned} \tag{11}$$

Thus, if the measured equilibrium pressure of hydrogen corresponds to a saturated solution of hydrogen in sodium at the temperature T, then the dependence of this pressure on the temperature should be described by Eq. (10).

Measurement of the steady pressure of hydrogen in the sodium circuit (in which the source of impurities is the cold trap, containing the reaction products of water with sodium), and comparison with the existing data about the solubility of hydrogen, enables it to be established whether or not the level of the hydrogen concentration attained for this temperature regime in the cold trap, corresponds to the solubility of this element at the temperature at the outlet from the cold trap. Thereby, the operating conditions of the cold trap can be determined, for which the steady hydrogen concentration in the circuit is determined by the temperature at the outlet from the cold trap. Based on the results of these experiments, the coefficient A which characterizes the temperature dependence of the solubility of hydrogen in the sodium, also can be refined (see Eq. (8)). In this case, simultaneous monitoring of the hydrogen pressure in the circuit, enables it to be determined to what extent the readings of the plug indicator coincide with the saturation temperature of the sodium by hydrogen.

In order to determine the hydrogen pressure in the circuit, a procedure was used based on the use of a hydrogen-permeable nickel membrane, one side of the surface of which communicated with a manometer, and the other side was in contact with the sodium circuit [1]. The sodium circuit was equipped with a trap with a volume of 100 liters.

The driving-in temperature was measured with the plug indicator, the disk of which had 32 grooves with cross sections 0.4 × 0.6 mm. The content in the trap of reaction products of water with the sodium was equivalent to the amount formed by the reaction with sodium of ~1 kg of water. The experiments were conducted in the following way. A specified temperature (450 or 500°C) was maintained in the circuit and the chosen temperature regime was maintained in the cold trap, prior to the establishment of constant readings of the hydrogen pressure gauge in the circuit. The sodium flow rate through the trap was constant in all experiments. Steady values of the hydrogen pressure and the driving-in temperature of the plug indicator in the circuit were attained after approximately 1.5 h.

After measuring the steady hydrogen pressure in the circuit, in the majority of the experiments the driving-in temperature of the plug indicator also was determined. Then a new temperature regime of the cold trap was established and the steady hydrogen pressure and driving-in temperature in the circuit were measured.

Two series of experiments were carried out, in which the temperature regimes of the cold trap differed in the nature of the temperature distribution inside the trap along its length. In the first series of experiments, the temperature distribution over the length of the trap

475

was nonuniform (the temperature in the settling tank was approximately 30 C lower than the temperature at the outlet from the trap). In the second series of experiments, the change (reduction) of temperature over the length of the trap from the settling tank to the outlet did not exceed 5°C.

Figures 1 and 2 show the results of the measurements of the steady hydrogen pressure in the sodium circuit for different temperature regimes of the continuously operating cold trap, and data of the measurements of the driving-in temperature of the plug indicator.

Markedly different relations were obtained (see Fig. 1) for the two operating regimes of the cold trap — with uniform and nonuniform distribution (when the temperature inside the trap is significantly lower than at its outlet) of the temperature over its length. These relations, for the stated temperature regimes of the cold trap, on processing the data by the method of least squares are represented by the following equations. In the case of a uniform temperature distribution in the trap

$$\lg p = 13.746 - \frac{6104}{T_{ex}} ; \tag{12}$$

and in the case of a nonuniform temperature distribution in the trap

$$\lg p = 12.56 - \frac{5546}{T_{ex}} . \tag{13}$$

Figure 1 also shows the relation obtained in [2].

$$\lg p_s = 13.86 - \frac{6160}{T} . \tag{14}$$

In essence, Eq. (12) compiled from the results of our experiments for the case of a uniform temperature distribution in the trap, coincides with relation (14), which was determined in [2] by means of direct measurements of the hydrogen pressure above its saturated solutions in sodium. On the basis of the coincidence of our relation (12) and Eq. (14), it can be confirmed that in the case of a uniform temperature distribution over the length of the cold trap con-
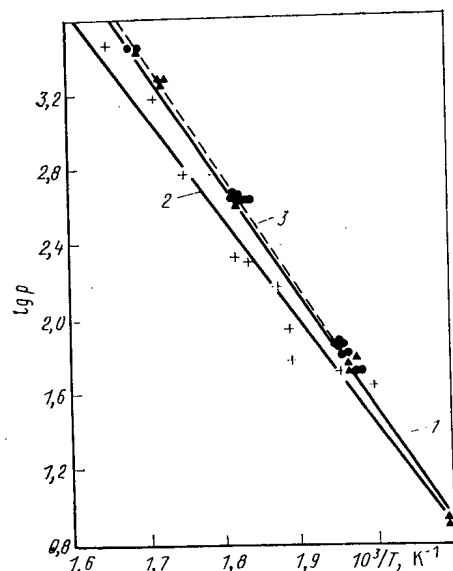
Fig. 1
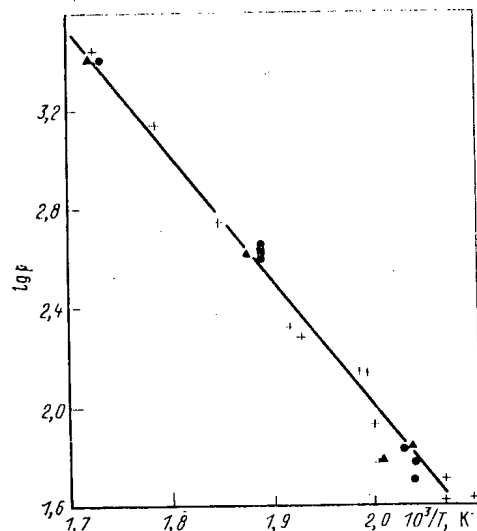
Fig. 2

Fig. 1. Dependence of the steady hydrogen pressure in the circuit on the sodium temperature at the outlet from the cold trap: +) $T_c = 450°C$, $T_{ex} > T_{i.t}$ (T_c is the temperature of the circuit; T_{ex} and $T_{i.t}$ are the temperatures at the outlet from and inside the trap); ●) $T_c = 450°C$, $T_{ex} < T_{i.t}$; ▲) $T_c = 500°C$, $T_{ex} < T_{i.t}$; 1) log (P, Pa) = 13.746 − 6104/T_{ex}; 2) log(P, Pa) = 12.56 − 5546/T_{ex}; 3) log(P, Pa) = 13.86 − 6160/T, data of [2].

Fig. 2. Dependence of the steady hydrogen pressure in the circuit on the driving-in temperature of the plug indicator: +) $t_c = 450°C$, $t_{ex} > t_{i.t}$; ●) $t_c = 450°C$, $t_{ex} < t_{i.t}$; ▲) $t_c = 500°C$; $t_{ex} < t_{i.t}$; ——) log (P, Pa) = 12.3816−5200/T_d (T_d is the driving-in temperature).

476

taining the reaction products of water with the sodium in the solid state, the concentration of hydrogen at the outlet from the cold trap is equal to the saturation concentration (solubility) for the temperature at the outlet from the trap. Equation (12) just like Eq. (14) also coincides well with the generalized relation given by different authors for saturated solutions of hydrogen in sodium, obtained in [2]:

$$\lg p = 13.82 - \frac{6122}{T}. \tag{15}$$

It can be concluded from a comparison of Eqs. (13) and (14) that in the case of a non-uniform temperature distribution over the length of the cold trap (inside it the temperature is considerably lower than at the outlet), the concentration of hydrogen at the outlet did not attain the value of the solubility corresponding to the temperature at the outlet from the trap.

Figure 2 shows the results of simultaneous measurements of the hydrogen pressure in the circuit and the driving-in temperature of the plug indicator, and also the relation between them, found by the method of least squares

$$\lg p = 12.386 - \frac{5200}{T_d}. \tag{16}$$

A comparison of relations (12) and (16) shows that the driving-in temperature, determined by means of the plug indicator, was lower than the saturation temperature of the sodium with hydrogen (the maximum difference reached 25°C with a temperature at the outlet from the trap of ~200°C, decreasing with increase of the latter). This means that the concentration of hydrogen dissolved in the sodium, determined from the driving-in temperature of the plug indicator, using the solubility temperature relations obtained by other authors can be significantly underestimated.

In order to eliminate such errors in estimates of the concentrations shown by the readings of the plug indicator, the solubility equations of hydrogen in sodium should be used, found by means of this indicator. It is interesting to note that the coefficient for $1/T_d$ in Eq. (16) proved to be a factor of 2 greater than in the equation for the solubility in sodium of its reaction products with water, found by the method of least squares, which indirectly confirms the dependence of the Sievert constant K on the temperature. This equation, obtained by introducing a known amount of water into the sodium and then monitoring the steady driving-in temperature of the plug indicator, has the form

$$\lg C_H = 5.93 - \frac{2600}{T_d}, \tag{17}$$

where C_H is the concentration in the sodium of its reaction products with water (calculated on hydrogen), ppm. Sievert's constant, determined by Eqs. (16) and (17), taking account of relation (9) was found to be equal to ~0.55 ppm/Pa$^{1/2}$.

LITERATURE CITED

1. F. A. Kozlov, E. K. Kuznetsov, G. P. Sergeev, et al., "Operation of a steam generator with sodium and water in the secondary circuit with small leakages of water into the sodium," in: Proceedings of the Physico-Power Institute [in Russian], Atomizdat, Moscow (1974), pp. 290-308.
2. A. Whittingham, J. Nucl. Mater., 60, 113-120 (1976).

HYDROGEN INDICATOR FOR MONITORING THE HERMETICITY OF SODIUM–WATER STEAM GENERATORS

F. A. Kozlov, V. A. Egorov, P. S. Kozub,
E. K. Kuznetsov, V. V. Matyukhin, V. V. Leshkov,
G. I. Laptev, and I. D. Ponimash

During the operation of sodium–water steam generators, continuous monitoring of their intercircuit hermeticity is essential. The requirements on the monitoring systems for the entry of water into the sodium mainly are determined by the stability of the structural materials in conditions of leakage of water into the sodium. In the case of leaks of more than a few tens of grams per second, the pipe-target of 10Kh2M steel, used at present, can be punctured right through in less than 1 min and the common focus of destruction of tubes in the tube bundle can spread rapidly. It is expected that in the majority of cases, leaks will develop in consequence of microleaks, the action of which on adjacent tubes is unimportant. However, microleaks are capable of self-development. The specifics of their self-development are such that in the final stage, over tens of seconds, the leak is increased by several orders of magnitude, and therefore it is desirable to detect the microleaks at the stage of self-development [1].

Taking into consideration that the modern steam generators consist structurally of quite large modules, systems for monitoring the entry of water into the sodium should be rapid-acting and highly sensitive. In order to detect the leak, different effects can be used, which accompany the interaction of water with sodium. Monitoring the concentration of hydrogen in the sodium by means of indicators, the principal element of which is a high-vacuum unit incorporating a hydrogen-permeable membrane and a magnetodischarge pump [2, 3], has received the most widespread circulation.

The operating principle of a hydrogen indicator of this type consists in the following. The hydrogen from the sodium diffuses through a nickel membrane into an evacuated cavity the pressure in which, in consequence of continuous pumping out of the hydrogen which has entered by the magnetodischarge pump, is maintained at a level much less than the equilibrium pressure of hydrogen above the sodium, p. In these conditions, the leakage of hydrogen Q through the membrane is determined by the expression

$$Q = K_p \frac{S}{\delta} \sqrt{p}, \tag{1}$$

where K_p is the coefficient of permeability; S is the area of the diffusion surface, and δ is the thickness of the membrane.

The value of p can be found by using Sievert's constant K_s

$$K_s = C/\sqrt{p}. \tag{2}$$

The dependence of K_p on the temperature is described by the expression

$$K_p = K_0 \exp\left(-\frac{E_p - \Delta H}{RT}\right), \tag{3}$$

where K_0 is the preexponential factor; E_p is the permeability energy of activation; ΔH is the heat of solution of hydrogen in sodium (according to the data of [4], $\Delta H = 0$).

Hydrogen, entering the vacuum cavity, is ionized in the gas discharge between the pump electrodes. The hydrogen ions reach the cathode, where they are neutralized and absorbed by titanium. As a result, a current I is generated, the value of which over a wide range of working pressure is directly proportional to the pressure of the gas pumped out. Taking into account that the current depends linearly on the flow of the gas pumped out, we obtain

$$I = KQ. \tag{4}$$

Combining Eqs. (1)-(4), we find

$$I = K \frac{S}{\delta} \frac{1}{K_s} C K_0 \exp\left(-\frac{E_p}{RT}\right). \tag{5}$$

Thus, the pump current in the case of a constant temperature of the membrane, is directly proportional to the concentration of hydrogen in the sodium.

An estimate of the speed of response of the indicator, due to the diffusion of hydrogen through the membrane, can be carried out by the approximate expression

$$\tau_\alpha = \frac{\delta^2}{D\pi^2} \ln \frac{2}{1-\alpha}, \tag{6}$$

obtained from the solution of the nonsteady diffusion equation. Here τ is the time of attainment of a fraction α of the steady flow of hydrogen through the membrane, after a stepwise change of the hydrogen concentration in the sodium ($\alpha > 0.2$); D is the coefficient of diffusion of hydrogen in the membrane.

In order to achieve a prolonged service life of the indicator, the working pressure in the pump must be chosen according to a lower potentiality, in order to ensure reproducibility of the dependence of the discharge current on the pressure. This pressure should also be attained easily with the use of the available technology for the manufacture of high-vacuum systems. Taking these requirements and the use of commercially produced pumps into account, the minimum working pressure was chosen as $\sim 1 \cdot 10^{-6}$ Pa ($\sim 1 \cdot 10^{-8}$ mm Hg). In the event of indication of a leak, it is necessary to ensure the measurement of the hydrogen concentration in the sodium within limits of 1-2 orders, and therefore a pressure of $\sim 1 \cdot 10^4$ Pa ($\sim 1 \cdot 10^{-6}$ mm Hg) was taken as the working pressure.

The NMDO-0.01 and NMD-0.0063 series production pumps are chosen as indicators, in which the proportionality coefficient between the discharge current and the gas pressure amounts to ~ 1 A/Pa [5], which gives

$$K = 42 \frac{A \cdot m^3 \cdot Pa}{sec}. \tag{7}$$

We note that the value of K is assumed to be independent of the pumping speed of the pump. K = 42 corresponds to the case when, for pumping out a single molecule of gas, one electron is used. The actual processes in the pump during pumping out of the hydrogen are complex: the hydrogen is absorbed by the titanium both in the form of ions after their neutralization at the cathode, and in the molecular form. It is possible that a hydrogen ion, after neutralization at the cathode, will not be absorbed by the titanium but in the form of a molecule will again enter the volume of the vacuum unit. Therefore, in the general case, it is necessary in expression (7) to insert a correction factor $\varkappa$, the value of which can be larger or smaller than unity.

Nickel was chosen as the material for the membrane, which is stable in sodium and also possesses the necessary permeability and stable coefficient of diffusion of hydrogen. The data obtained by us about the permeability coefficient of hydrogen through nickel in the range 350-550°C are described by the following expression, where K_p is measured in $m^3 \cdot m \cdot Pa^{1/2}/(sec \cdot m^2)$:

$$K_p = 3.96 \cdot 10^{-4} \exp\left(-\frac{6050}{T}\right). \tag{8}$$

Taking into account the data derived and the value of $K_s = 0.43$ ppm/Pa$^{1/2}$ [4], expression (5) can be written in the form

$$T = \varkappa 3.87 \cdot 10^{-2} \cdot \frac{S}{\delta} C \exp\left(-\frac{6050}{T}\right) \tag{9}$$

or, with $\varkappa T = $ const, $I = \overline{K}C$.

In accordance with the general situation [6], it was assumed that the limiting sensitivity of the hydrogen indicator [ΔC] is equal to

$$[\Delta C] = 2 [\Delta I]/\overline{K} = 2 [(I_{max} - I_{min})] \overline{K}, \tag{10}$$

where [ΔI] is the maximum change of current of the pump during any hour of operation of the indicator.

479

using expressions (6), (9) and the data about the diffusion coefficients of hydrogen in nickel [7], the area of the surface, the thickness and the working temperature of the membranes were chosen. For this, it was taken into consideration that the pressure in the pump cannot exceed $1 \cdot 10^{-4}$ Pa for a hydrogen concentration in the sodium of $C \approx 1$ ppm, and the corresponding fast response must be ensured (the time constant of the membrane not greater than 10 sec). The structural diaggam of the indicator is shown in Fig. 1 and the principal design data are shown below.

Membrane:

Material	Nickel NMG-0.08V TU 48-08-400-71
Area of diffusion surface, cm^2	20
Thickness, mm	0.25
Construction.	Tube with diameter 6 mm, plugged at one end
Calculated time constant (at 500°C, $\alpha = 0.63$), sec	~7

Pump:

Type	NMDO-0.01 or NMD-0.0063
Pumping speed with respect to air, liter/sec	10 or 6.3
Supply voltage, kV	4.5 ± 3%

Vacuum unit:

dimensions, mm	420 × 290 × 480
mass, kg	8-10

Technological parameters:

Sodium flow rate, m^3/h	0.8 m^3
Time of transfer of the sodium in the indicator (before the membrane), sec.	20
Sodium temperature (membrane), °C.	500 ± 2

Calibration curve:

calculation by formula (9), with $\varkappa = 1$	I (μA) corresponds to 125 sec, ppm
experiment	I (μA) corresponds to (100-300) sec, ppm.

In order to reduce the effect of the factors influencing the output signal, the temperature of the membrane is maintained at the specified level with an accuracy of ±2°C, by the thermocontrol system (see Fig. 1), and the pump power supply is effected by current from a stabilized voltage. The electronic unit provides the pump power supply in the startup and operating regime, measurement of the pump current and indication of excess of the permissible rate of increase of the current. The range of the pump current being measured is divided into several subranges with limits of 10 μA-100 mA, and the range of the specified signalization threshold is 15-600 %/h. A reliable combination of nickel with stainless steel was also developed. The heat exchanger, heater, and vacuum unit (see Fig. 1) are combined in a single system.

The characteristics of the hydrogen indicator were studied both on an experimental test-rig and in operating conditions on industrial plants. The results obtained show that the characteristics of the indicators differ significantly from the calculated relation, and for vacuum units identical in design, the sensitivity factors can differ by several times. A typical curve for the pump current versus the concentration of hydrogen in the sodium is shown in Fig. 2. It is characteristic, that with a concentration of hydrogen in the sodium of less than 0.1 ppm, the sensitivity of the indicator to hydrogen is reduced, and therefore the calibration

480
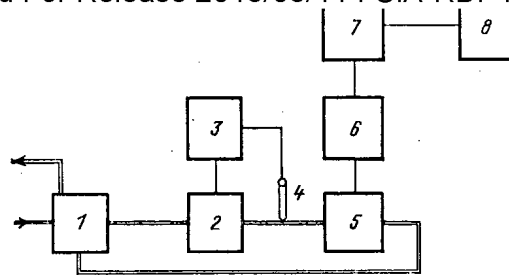
Fig. 1. Structural diagram of the hydrogen indicator: 1) recuperator; 2) heater; 3) control unit with heater; 4) thermocouple; 5) membrane; 6) magnetodischarge pump; 7) power supply, measurement, and signaling unit; 8) pen-recorder.
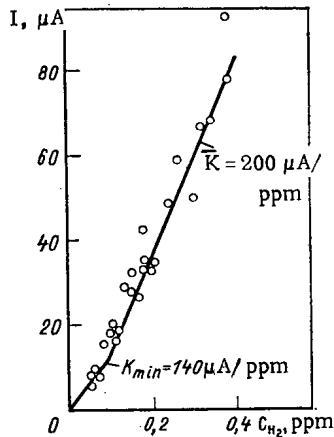
Fig. 2

Fig. 3

Fig. 2. Calibration characteristic curve of the hydrogen indicator with a NMDO-0.01 pump; O) experimental data; ———) calculation.
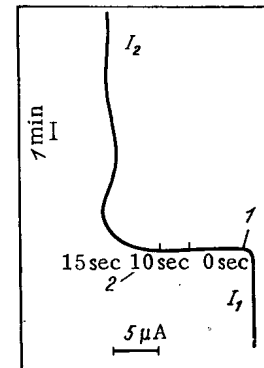
Fig. 3. Determination of the time constant of the hydrogen indicator: 1) change of concentration of hydrogen in the sodium after $\Delta t < 2$ sec; 2) time constant 63% ($I_1 - I_2$).

characteristic curve is best described by two intercepts of straight lines with slopes of 140 and 200 μA/ppm. The sensitivity is worsened in proportion with the absorption of hydrogen, and the rate of reduction of sensitivity with time is reduced, which may be related with the following pumping-out mechanism. In proportion with the pumping-out of the hydrogen, the upper layers of titanium are enriched, a titanium hydride phase is formed which has a larger specific volume than the base material. As a result, mechanical stresses originate, leading to cracking and the appearance of pure surfaces of titanium which, in its turn, leads to an increase of the molecular pumping-pout of hydrogen by the pump. This phenomenon is called hydrogen activation [2] and is assumed to be the main factor leading to the considerable reduction of sensitivity of the indicator.

The relation between ion and molecular pumping-out will depend only on the capability of titanium to sputtering, which is determined by the state and structure of the surface: oxide films, surface contamination, and impurities in the titanium.

Contamination of the vacuum unit, despite the final stage of outgassing warmup, leads to the appearance of increased noise of the pump current, which reduces the sensitivity of the indicator. A stiffening of the manufacturing technology of the vacuum units was required, with the introduction of methods of purifying the components and the requirements of vacuum hygiene, used in the production of electronic-vacuum instruments [8].

481

is the
principal factor at the present time limiting the minimum sensitivity of the indicators. Over
a long time of several thousands of hours, a sensitivity of 0.005-0.007 ppm was achieved. Over
95% of the working time, it was not less than 0.02 ppm. For the remaining time, the noise
was excessive and the threshold of sensitivity deteriorated by a factor of several. The reduc-
tion of sensitivity during operation, and the spontaneous generation of pump current noise, re-
quired the development of special methods and devices to allow operative elimination of the
noise, and the characteristics of the indicators to be checked. This allows their working life
to be prolonged and operating expenses to be reduced.

In order to determine the time constant of the indicator, the concentration of hydrogen
in the sodium washing the hydrogen probe was varied stepwise. Typical results of these exper-
iments are shown in Fig. 3. It follows from it that the time constant does not exceed 15
sec. This is a factor of two larger than the calculated value for a nickel membrane which,
evidently, is explained by the processes in the high-vacuum unit as a whole, including the
pump.

Based on the results obtained, hydrogen indicators have been developed and manufactured
by industry, which are being used in the BN-350 and BN-600 plants as the principal standard
systems for monitoring leakages of the steam generators. All cases of water leakages into the
sodium are recorded by means of them.

The authors thank the staff of A. I. Mogil'ner and V. A. Romanov for assistance in the
development of measures to reduce the pump current noise.

<div align="center">LITERATURE CITED</div>

1. F. A. Kozlov et al., in: Proceedings of an International Conference on Liquid Metal Tech-
    nology in Energy Production. ANS-AIME Meeting, CONF 760503-P (1976), p. 202.
2. R. Vissers et al., "A hydrogen monitor for detection of leaks in LMFBR steam generators,"
    Nucl. Technol., 12, 218 (1971).
3. P. Lecocq et al., "Monitoring the sodium-water hermeticity in sodium-steam generators by
    the determination of hydrogen," in: Proceedings of Symposium of Nuclear Power Plant Con-
    trol and Instrumentation [in French], Report IAEA-SM-168/E-7, IAEA, Vienna (1973), p.
    613.
4. A. Whitingham, "An equilibrium and kinetic study of the liquid sodium-hydrogen reaction
    and its relevance to sodium-water leak detection in LMFBR systems," J. Nucl. Mater., 60,
    119 (1976).
5. G. A. Vasil'ev, Magnetodischarge Pumps [in Russian], Énergiya, Moscow (1970), p. 113.
6. N. G. Farzane, L. V. Ilyasov and A. Yu. Azim-Zade, Automatic Detectors of Gases and Li-
    quids [in Russian], Énergoizdat, Moscow (1983), p. 95.
7. E. Johnson and T. Hill, "The diffusion of hydrogen in nickel," Acta Metallurgica, 3, No.
    6 (1955).
8. B. D. Luft and A. L. Shustina, Cleansing of the Components of Electronic Instruments [in
    Russian], Énergiya, Moscow (1968), p. 320.

PROGRAM COMPLEXES FOR CALCULATING CELLS OF LOCAL THERMOHYDRAULIC PARAMETERS

IN ROD CLUSTERS BY THE CELL METHOD

Yu. V. Mironov   UDC 621.039.546:536.24

As the efficiency and safety requirements of nuclear power stations become more strin-
gent, there is increased interest in the use of methods for analyzing the local parameters
of the coolant in the cores of various types of reactor. The most highly developed approach
to this problem at the moment is based upon the cell method. Investigations carried out along
these lines abroad were intensified in the mid sixties. Studies [1, 2] were begun in the USSR
at this time, but the basic development of an effective program had to wait until the 1970s,
when the introduction of the BÉSM-6 computer into research centers enabled large systems of
differential equations to be integrated. The PUCHOK 2 program [3, 4] was created at this time
and a great deal of theoretical, design, and experimental studies were carried out into its
fundamentals. This program and its variants paved the way for the study of local heat ex-
change and heat transfer crises, but the method of determining transverse coolant flows and
the matrix format of the link between cells of transverse coolant flows limited this program
to assemblies with large numbers of fuel elements. Consequently, a new PUCHOK BM (for high
power) program [5] was developed for designing multirod cores for the gas cooled reactor, in
which the problem of transverse coolant flows is dealt with in the iteration process. The
program as a whole is characterized by the following properties:

it is compiled in FORTRAN, taking the special features of the BÉSM-6 computer into ac-
count;

a steady-state system of mass balance, the momentum and the energy for channels whose
cross sections contain up to 300 element cells are solved, while this number can be
doubled if need be;

the thermohydraulic equations are integrated for systems of interrelated element chan-
nels, using the Euler method, with conversion and automatic choice of step;

the flow in the cells is determined by equating the longitudinal pressure gradient by
iteration at each step;

three mechanisms of transverse mixing of the coolant are taken into consideration: con-
vection currents, turbulent exchange, and redistribution of flows throughout the cell
via the spacer lattices;

the hydraulic and thermal nonequivalences of the cells are accounted for in detail.

Several empirical correlations are realized in the program to describe turbulent exchange,
and these can be called upon as needed. They have a flexible universal structure requiring a
minimum of exchange of information about the geometry of the cluster, the results being print-
ed in the space designated by the operator.

In recent years, a need has arisen for the detailed analysis of the thermohydraulics of
coolants in the cores of reactors of various designs and for various applications. For this
reason, a set of programs has been developed on the basis of PUCHOK BM for the thermohydraulic
design of the following types of core:

gas- and vapor-cooled clusters with intensified heat exchange through the action of arti-
ficial roughening or irregularities on the surfaces of the fuel elements;

gas-cooled assemblies with fuel elements spaced by being wound with wire;

water-cooled cores (including boiling water-cooled cores) with lattice spaced or wire-
bound fuel elements.

The integrated system of mass balances, momentum, and energy for each cell have the fol-
lowing form

$$\frac{d}{dz} \cdots \sum_n \mathit{W}_{kn} + \sum_n \mathit{W}_{kn}^{sw};$$

$$\frac{1}{F_k}\frac{d}{dz}(m_k^2\,\vartheta_{ik}) + F_k\frac{dP}{dz} = \sum_j \tau_k^j \Pi_k^j + \sum_n t_{kn}^* W_{kn} + \sum_n U_{kn}^{**} W_{kn}^{sw} + \sum_n \beta_{kn}\frac{m_k \cdots m_n}{F_k \cdots F_n}(U_n - U_k); \qquad (1)$$

$$\frac{d}{dz}\left[m_k\left(i_k + \frac{m_k^2\,\vartheta_{ek}^2}{2F_k^2} \right)\right] = \sum_j q_k^j \Pi_k^j + \sum_n i_{kn}^* W_{kn} + \sum_n i_{kn}^{**} W_{kn}^{sw} + \sum_n \beta_{kn}\frac{m_k \cdots m_n}{F_k \cdots F_n}(i_n - i_k).$$

where z is the coordinate running along the axis of the channel; m_k, flow in the k-th cell whose cross-sectional area is F_k; P and i_k, pressure and heat content of the flow in the k-th cell; ϑ_{ik} and ϑ_{ek}, specific volume of the coolant in the k-th cell obtained by averaging the impulse and energy respectively, τ_k^j and q_k^j, friction force and heat flow at the j-th wall of the k-th cell, the wetted perimeter of which is Π_k^j; W_{kn}, convective flow from the n-th cell to the k-th cell; W_{kn}^{sw}, so-called "slippage flow" along the coil between the n-th and k-th cells; β_{kn}, turbulent mixing factor between cells, given by empirical correlations; U_k, average speed throughout the section. The asterisks indicate the specific impulse and heat content of the cross flow, taken as being equal to the values in the donor cells for the flow W_{kn}. The algorithm for finding the flows is described in detail in [5]. Two asterisks indicate the parameters of slippage flow W_{kn}^{ws}, whose role in the core of average height is in reinforcing the turbulent exchange of coolant through the peripheral cells along the jacket of the core.

In order to investigate the hydrodynamics and heat exchange in cores with artificial irregularities on the surfaces of their fuel elements, a version referred to as PUCHOK BM-RIP [6] has been developed, in which the speed and temperature profiles close to the surface irregularities are approximated by universal logarithmic profiles [7]:

$$U^+ = 2.5 \ln y/h + R\,(h^+);$$
$$t^+ = 2.5 \ln y/h + G\,(h^+), \qquad (2)$$

where $U^+ = U/U^*$; U, speed of flow at a distance y from the surface; U^*, dynamic flow speed within the cell; h, height of the projections; $t^+ = c\rho U^*(t_w - t)/q$, dimensionless temperature; c and ρ, heat capacity and density of the gas; t, temperature of the flow at a distance y from the walls; t_w, wall temperature; q, heat flow; functions R and G and Eq. (2) depend upon the dimensionless height of the irregularities: $h^+ = hU^*/\nu$; ν, kinetic viscosity of the gas.

Each cell and each version is treated as part of an equivalent annular channel, for which the parameters of the logarithmic profile (2) are calculated at each step in relation to the local parameters of flow in the cell. Correlations R and G for the shape of the artificial irregularities can be obtained as generalized expressions in terms of a small number of parameters, whose numerical values can be found by experiments carried out on individual fuel elements, as was shown in [6].

Figures 1 and 2 compare the data calculated by the PUCKOK BM-RIP program with test data obtained on an ACATHE HEX cluster [8]. In these experiments, 31 rods with heating that was irregular in both section and length were placed in a hexagonal casing with a relative step of 1.3. The cluster was cooled by carbon monoxide. The calculations used relationships for $R(h^+)$ and $G(h^+)$ derived in [8] from tests with individual rods. The mixing between cells in the roughened zone was increased in line with the theoretical results of Rapier [9] in proportion to the square root of the average hydraulic friction coefficient for the cell relative to the mixing coefficient for a smooth zone, which was calculated from data given in [10]. The examples showed that the calculated and experimental results were in agreement over a wide range of Reynolds numbers.

A special version of the PUCHOK program, known as BM-VAP, was developed for steam superheater channels. In this program, the thermal and physical properties of the steam are first calculated by a program complex [11] and fed into the computer memory in the form of tables of pressure and heat content, suitable for interpolation. One version of the PUCHOK program, known as BM-SWEEP, already enables us to design gas-cooled cores with wire-wound fuel elements. We should bear in mind that as far as the specific design of the gas and steam cooled cores developed in the Soviet Union is concerned, the most urgent problems of experimental investigation are the local hydrodynamics and heat exchange in the peripheral cells of the core, where marked temperature differences can arise in the perimeter fuel elements. These

484
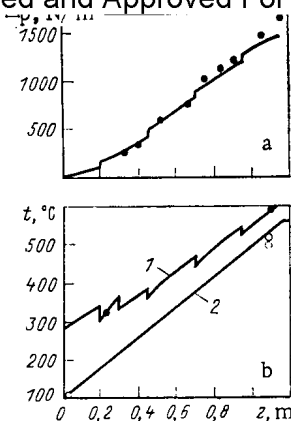
Fig. 1   Fig. 2

Fig. 1. Comparison of data calculated by the PUCHOK BM-RIP program with test data for an ACAHE HEX cluster. Test No. 138, gas pressure 0.298 MP, Re number 8426: a) pressure drop on heated section: ●) by experiment; ———) by calculation; b) temperature distribution over heated section: ●, ○) by experiment; 1, 2) by calculation; ● , 1) the temperature at the surface of the central rod; ○, 2) the gas temperature in the central cell.
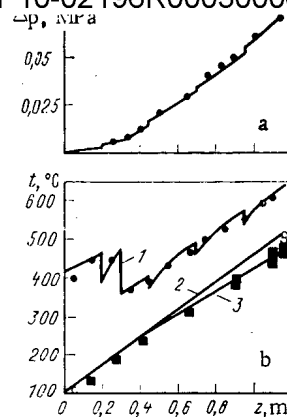
Fig. 2. Comparison of data calculated by the PUCHOK BM-RIP program with test data for an ACATHE HEX cluster. Test No. 125, gas pressure 3.97 MP, Re number 193,000: a) pressure drop on heated section: ●) by experiment; ——— by calculation; b) temperature distribution over heated part: ●, ○, ■) by experiment; 1, 2, 3) by calculation; ● , 1) the temperature at the surface of the central rod; ○, 2) the gas temperature in the central cell; ■ , 3) the temperature of the cassette jacket.

problems include the distribution of flow rates between the peripheral and central cells, the intensity of the mixing between the peripheral cells, and the law governing the heat extraction from the surfaces of the peripheral fuel elements. These problems have been inadequately studied up to the present, particularly for the case of clusters with artificial roughening. They represent an additional source of improvement in reliability that can be tapped by the methods of calculation which we are describing.

A version of the PUCHOK program, known as BM-DF (signifying two-phase) has been developed for analyzing cores cooled by water and steam—water mixtures. The physical model for this program takes account of the separate boiling of the water in the various cells and the presence of zones of surface boiling of nonuniform steam—water mixtures [12], whose steam content can be taken into consideration by means of the relationships used both for an individual cell and for an isolated channel. The two-phase hydraulic flow losses are described by an empirical correlation [2]. This program can calculate local heat-exchange crises on the basis of local steam—water flow parameters, for the most heat-stressed fuel element in each cell. Generalized correlations were derived from [13-15] for this purpose. The thermal and physical properties of the water and steam mixture are calculated as before, using program pack [11].

Calculations according to the PUCHOK 2 program have already been compared [4] with test data that existed at the time, and these have also been compared with the results achieved by similar programs abroad. Since PUCHOK 2 and PUCHOK BM-DF give similar results under the same conditions, the design possibilities of PUCHOK BM-DF will henceforth be compared with new material obtained in recent years.

The data given in (16) enable us to compare calculations made by program PUCHOK BM-DF with the results of calculations carried out by the American program COBRA II (Fig. 3). The calculations referred to electrically heated clusters of 25 rods (three of them unheated), heated uniformly along their length and nonuniformly throughout their cross sectional area. The heated length was 1.676 m. The cluster was cooled by water under a pressure of more than 13 MPa. Both programs give roughly the same flows of heat in the cells, but the mass rate of flow calculated by the PUCHOK BM-DF program proved to be 5-7% lower than that obtained by COBRA II.

485
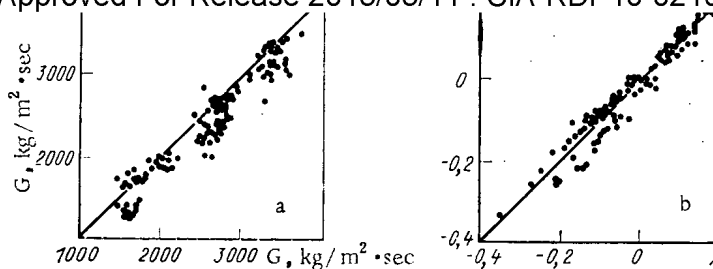
Fig. 3. Comparison of data calculated for ANC 3 clusters by means of the PUCHOK BM-DF program and COBRA II program (abscissa): a) mass rate of flow G in crisis cells; b) steam content balance x in crisis cells.
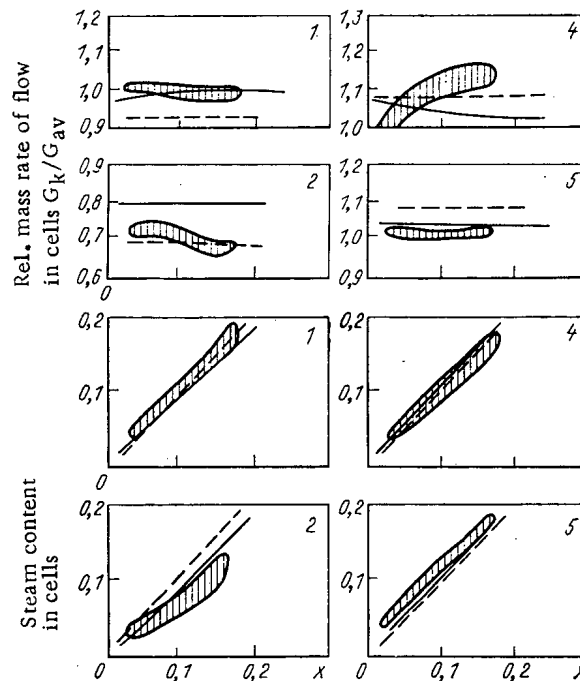
Fig. 4. Distribution of mass rate of flow (1500 kg/m^2 sec) and steam content in the cells of a PELCO-5 cluster: serial numbers of cells 1, 2, 4, 5; cross hatched area denotes experimental data; ———) data calculated by PUCHOK BM-DF program; ─────) data calculated by COBRA III-C program.

Figures 4 and 5 compare calculated and test data for a cell cluster of 16 uniformly heated rods in a square pack 3.66 m long [17]. The tests were carried out at a pressure of 17 MPa. Results achieved by the COBRA III-C are also given. The data show the accuracy of the predictions of nonuniformity in the distribution of the flow parameters throughout the cells of the cluster, with the exception of corner cell No. 2, where both programs give a somewhat increased steam content. This was apparently due to the influence of the unheated surfaces, which is more marked in the case of corner cells.

The possibility of using these programs for the prediction of heat exchange crises in cores of various designs are shown in Figs. 6 and 7. Figure 6 compares test data on heat-transfer crises for an ANC 3 cluster [16] with the calculated values of critical heat flow in cells using formulas obtained from [14]. In this case, with loads up to ∿3 MW/m^2 (which corresponds to the steam content balance in the experiments over —0.25) the general drift of the points shows a deviation of not more than 15%. A similar comparison is made in Fig. 7 between the ratio of calculated critical power N_{cr}^{calc} and critical power N_{cr}^{exp} obtained in experiments carried out on a type KS test rig for models of RMBK channels with nonuniform heating throughout both length and cross sectional area [18]. A comparison of the calculated and experimental results enables us with a high degree of reliance to employ the PUCHOK BM-DF program for analyzing the conditions of operation of fuel elements in real boiling water reactors.

486
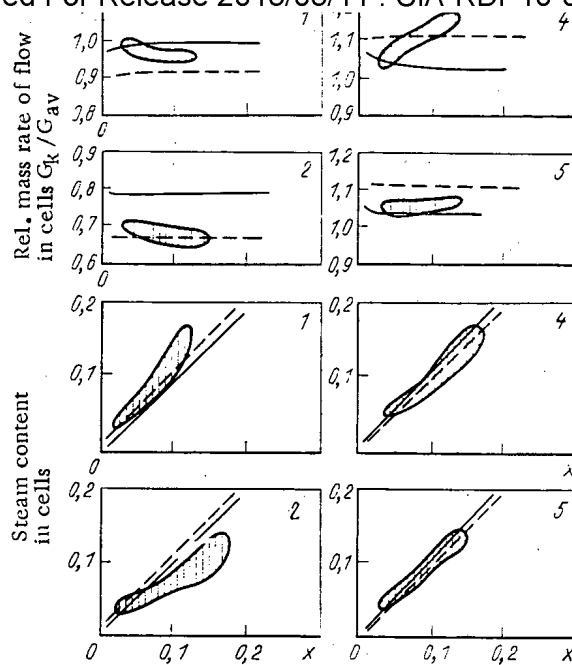
Fig. 5. Distribution of mass rate of flow (2000 kg/m²·sec) and steam content in the cells of a PELCO-5 cluster: serial numbers of cells 1, 2, 4, 5; cross hatched area denotes experimental data; ————) data calculated by PUCHOK BM-DF program; ——--—) data calculated by COBRA III-C program.
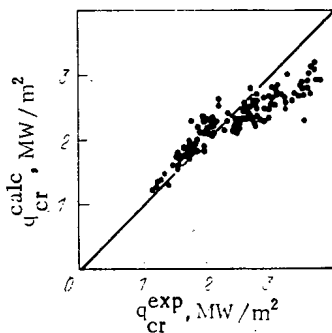
Fig. 6

Fig. 7

Fig. 6. Comparison of calculated and experimental valued of critical heat flows for an ANC 3 cluster [16].
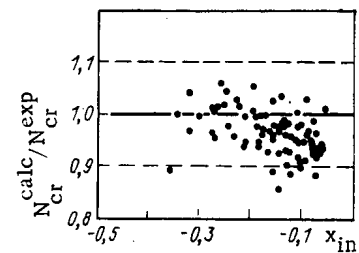
Fig. 7. Comparison of calculated and experimental critical powers for a 19-rod model of an RMBK core [18], in relation to relative heat content at input x_{in}.

In conclusion, we should note that the complex of programs described above is able to carry out the following functions for cores of various designs:

The analysis of thermal and physical experiments on the basis of local (cell) parameters of flow, leading to better-founded generalizations than can be reached by the use of parameters averaged throughout the whole cross sectional area;

the reliable application to real cores of the results obtained from models which in the general case are not exactly similar to the real designs;

the investigation of the influence of the structural parameters of the core over a wide range of operational parameters, which can greatly reduce the need for expansive large-scale experimental investigations.

487

LITERATURE CITED

1. A. N. Polyanin, "Heat and mass exchanges in rod bundles with cross currents of turbulent flows in liquids," At. Énerg., 26, No. 3, 279-280 (1969).
2. V. S. Osmachkin and V. D. Borisov, The Hydraulic Resistance of Clusters of Heat Generating Rods in a Flow of Boiling Water, Preprint IAÉ 1957, Moscow (1970).
3. Yu. V. Mironov, E. V. Sakovich, and S. V. Shpanskii, "Analyzing the hydrodynamics and heat exchange crises in clusters of smooth rods, taking nonuniformities in the distributions of thermohydraulic parameters throughout the cross section of the channel into account," in: Seminar TF-74: Investigating Critical Heat Flows in Clusters of Rods Under Steady-State and Nonsteady-State Conditions of Heat Exchange [in Russian], Moscow (1974), pp. 189-200.
4. Yu. V. Mironov and S. V. Shpanskii, "Distribution of two-phase flow parameters throughout the cross section of a channel with clusters of fuel elements," At. Énerg., 39, No. 6, 403-408 (1975).
5. G. S. Mingaleeva and Yu. V. Mironov, "Thermohydraulic calculation of multirod heat-dissipating clusters cooled by a single-phase coolant," At. Énerg., 48, No. 5, 303-308 (1980).
6. G. S. Mingaleeva, Yu. V. Mironov, N. S. Razina, and T. I. Fomicheva, "Heat exchange in gas-cooled clusters with artificial roughening," At. Énerg., 51, No. 6, 389-390 (1981).
7. M. Dalle Donne and L. Mayer, "Turbulent convection heat transfer from rough surfaces with two-dimensional rectangular ribs," Int. J. Heat Mass Transfer, 20, No. 6, 583-620 (1977).
8. M. Huggenburger, "Verification of thermal-hydraulic computer code SCRIMP by AVATHE HEX 31-rod bundle, 2: experimental data, TM-23-82-2," Eidg. Inst. für Reaktorforschung, April, 1982.
9. V. Walker, L. White, and P. Burnett, "Forced convection heat transfer for parallel flow through a roughened rod cluster," Int. J. Heat Mass Transfer, 15, No. 2, 403-424 (1972).
10. D. Rowe, "A mechanism for turbulent mixing between rod bundle subchannels," Trans. ANS, 12, No. 2, 805-806 (1969).
11. A. P. Nikonov, S. P. Nikonov, and E. A. Katkovskii, H_2O — a Packet of Applied Programs in FORTRAN for the Calculation of Thermal and Physical Properties and Their Derivatives for Water and Steam, Preprint IAÉ-3344/16, Moscow (1980).
12. Yu. S. Molochkikov and G. N. Batasheva, "Real steam content for boiling water superheated in tubes," in: Achievements in Investigating the Heat Exchange and Hydraulics of Two-Phase Flows in the Elements of Electrical Plant [in Russian], Nauka, Moscow (1973), pp.79-96.
13. V. S. Osmachkin and N. N. Lystsova, Comparing Test Data on Heat Exchange Crisis Conditions in Models of Fuel Clusters for Reactors Type VVÉR with the Results of Calculations by the IAÉ Method, Preprint IAÉ-2558, Moscow (1975).
14. V. N. Smolin and V. K. Polyakov, "Method of calculating heat-exchange crises with boiling coolant in rod clusters," in: Seminar TF-78: Thermophysical Investigations for Ensuring Reliability and Safety in Water-cooled—Water-moderated Nuclear Reactors, Budapest (1978), pp. 475-486.
15. L. Tong, Boiling Crisis and Critical Heat Flows [in Russian], Atomizdat, Moscow (1976).
16. S. Eide and R. Gottula, Evaluation and Results of Loft Steady-State Departure from Nucleate Boiling Test, TREE-NUREG-1043, Idaho National Engineering Laboratory (1977).
17. H. Herkenrath and W. Hufschmidt, "Experimental subchannel investigation in a 16-rod test section by means of the isokinetic sampling technique," in: Multiphase Transp. Fundam. React. Safety Appl., Proc. Multiphase Flow and Heat Transfer Symp. Workshop, Vol. 3, Miami Beach 16-18 Apr., 1979, pp. 1713-1736.
18. V. S. Osmachkin, Heat Exchange Crisis for Movement of Boiling Water Along Clusters of Heat Generating Rods, Preprint IAÉ-2014, Moscow (1972).

ENERGY DEPENDENCE OF THE MEAN NUMBER OF INSTANTANEOUS NEUTRONS

IN THE FISSION OF PLUTONIUM ISOTOPES BY NEUTRONS

V. V. Malinovskii, M. Z. Tarasko,
and B. D. Kuz'minov

UDC 539.173.081

The experimental results of measuring the mean number of instantaneous neutrons $\bar{\nu}_p$ in the fission of nuclei by neutrons was considered in detail in the reviews [1, 2]. For practical purposes, it is required to estimate the dependence $\bar{\nu}_p(E_n)$ allowing the value of ν_p and its indeterminacy to be determined in the given range of neutron energies (0-15 MeV). The plotting of this dependence must take account of experimental information to the fullest extent. The results selected for the estimates are from measurements of $\bar{\nu}_p$ for the nuclei [239-241]Pu performed with monoenergetic neutrons, including no less than four experimental values [3-18] and measurements with thermal neutrons [19] (Table 1, Figs. 1-5). There are no experimental data on $\bar{\nu}_p$ for fission of the nuclei [238]Pu and [242]Pu by neutrons. In this case, approximate dependences are plotted in accordance with the systematics of ν_p for various fissile nuclei and excitation energies established in [20].

The estimate of $\bar{\nu}_p(E_n)$ is sought in the form of a piecewise-linear dependence. This is because the estimate of ν_p is determined on different sections of the energy range 0-15 MeV by the fission of compound nuclei characterized by different excitation and different nucleon-
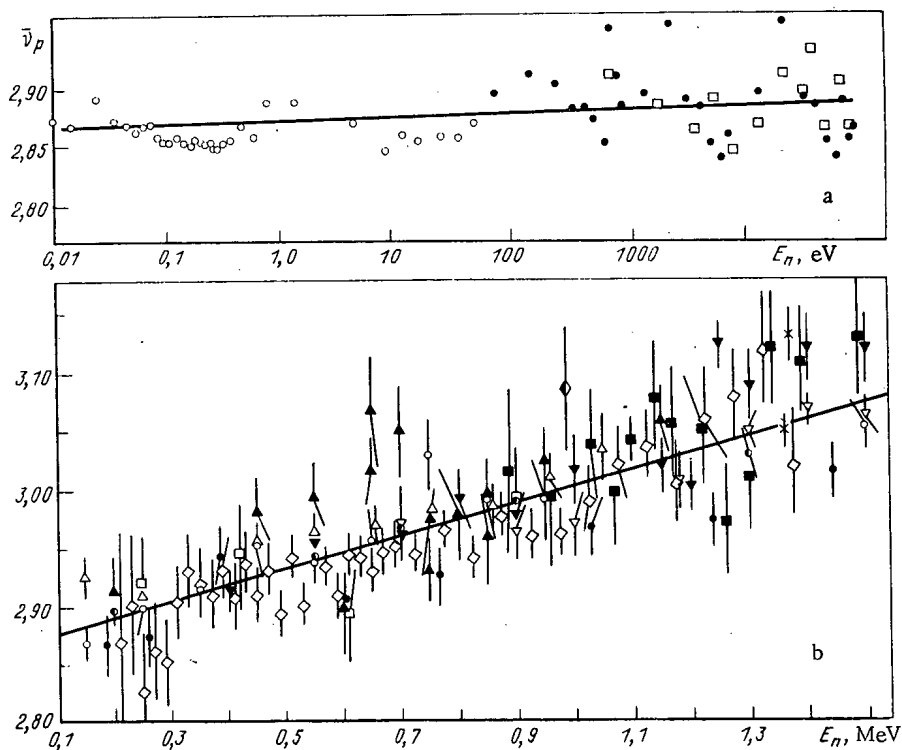
Fig. 1. Dependence of $\bar{\nu}_p$ in the fission of [239]Pu on the neutron energy E_n in the range from 0.01 eV to 0.1 MeV (a) and 0.1-1.5 MeV (b): a) results of three series of measurements in [11]; b) data of [3] (□), [4] (◆), [6] (■), [7] (▲), [8] (◑), [9] (▼), [10] (▽), [11] (o), series of measurements in the range $0.5 \cdot 10^{-3}$-10 MeV [11], series of measurements in the range $0.5 \cdot 10^{-4}$-7.2 MeV (△), [12, 13] (◇), [14, 15] (×), [17] (●); the data of [11] for energies of less than 1 MeV are grouped: the straight line shows the estimate obtained.
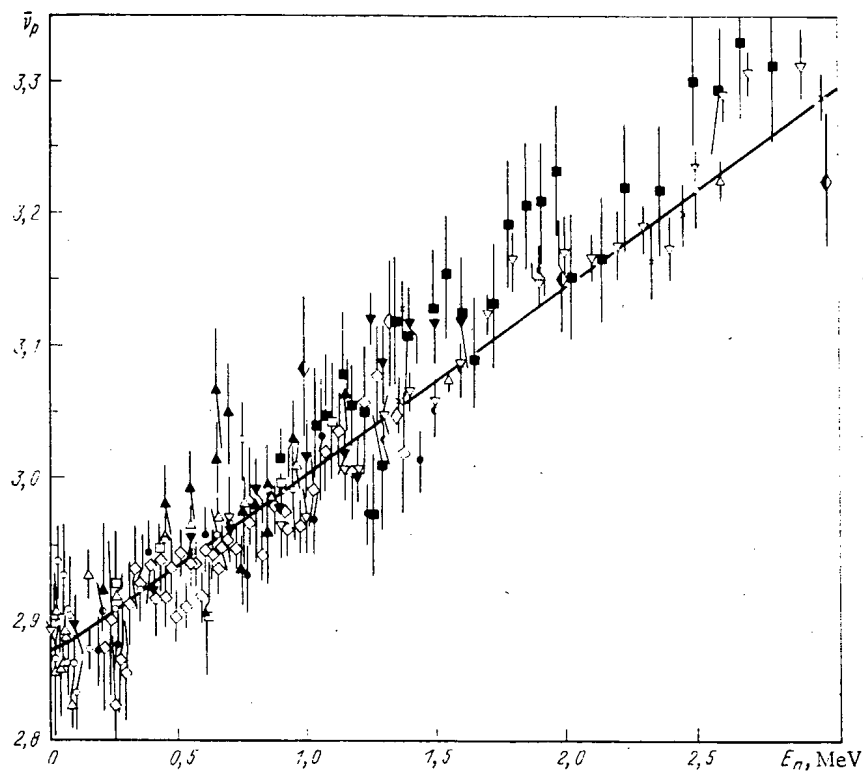
Fig. 2. Dependence of $\bar{\nu}_p$ in the fission of ^{239}Pu on the neutron energy E_n in the range 0–3 Mev. Notation as in Fig. 1b.
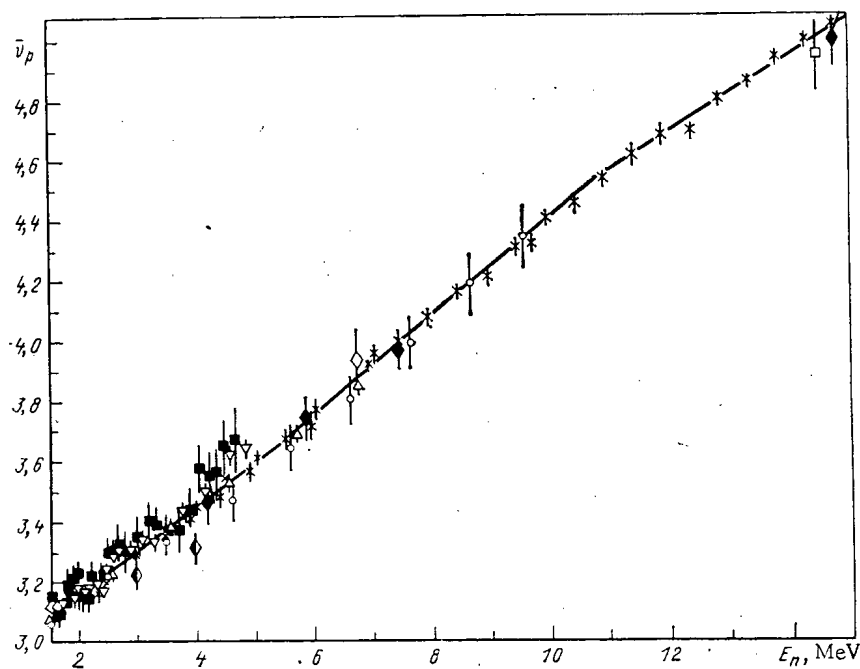
Fig. 3. Dependence of $\bar{\nu}_p$ in the fission of ^{239}Pu on the neutron energy E_n in the energy range 0–15 MeV; data of [5] (◆): the data of [6, 13] for energies below 1 MeV are grouped: remaining notation as in Fig. 1b.

490

TABLE 1. Experimental Data Used in Estimating the Energy Dependence of $\bar{\nu}_p$ for $^{239-241}$Pu

Source	Neutron energy range, MeV	Number of experimental points	Standard employed	Type of neutron detector	Systematic error taken in estimate, %
			^{239}Pu		
[3]	0,25—14,5	6	ν_p (^{252}Cf) = 3,771	Large liquid scintillator	1,0
[4]	0,99—4,02	4	$\bar{\nu}_p$ (^{252}Cf) = 3,782	The same	1,3
[5]	4,22—14,8	5	$\bar{\nu}_p$ (^{252}Cf) = 3,764	"	1,0
[6]	0,89—4,70	41	$\bar{\nu}_p$ (^{252}Cf) = 3,772	"	1,1
[7]	0,0775—1,15	11	$\bar{\nu}_p$ (^{252}Cf) = 1	"	1,1
[8]	0,2—1,9	8	$\bar{\nu}_p$ (^{252}Cf) = 3,724	"	0,5
[9]	0—1,6	16	$\bar{\nu}_p$ (^{252}Cf) = 3,756	^{3}He counter in moderator and fission chamber with ^{232}Th	1,1
[10]	0—4,89	27	$\bar{\nu}_p$ (^{252}Cf) = 3,756	^{3}He counter in moderate	1,0
[11]	0,5·10^{-3}—10 0,5·10^{-3}—7,2 (0,05—6)·10^{-7}	32 43 33	$\bar{\nu}_p$ (^{252}Cf) = 1	Large liquid scintillator	0,6
[12, 13]	0,21—1,375	40	$\bar{\nu}_p$ (^{252}Cf) = 3,732	The same	0,5
[14, 15]	1,36—14,79	34	$\bar{\nu}_p$ (^{252}Cf) = 3,732	"	
[16]	22,79—28,28	6	$\bar{\nu}_p$ (^{252}Cf) = 3,782	"	
[17]	0,186—1,44	8	Absolute measurements	"	0,9
Weighted mean of the measurement results with thermal neutrons [19]	< 0,3·10^{-7}	From four values			
			^{240}Pu		
[6]	1,08—3,94	24	$\bar{\nu}_p$ (^{252}Cf) = 3,772	"	1,2
[18]	1,87—14,79	22	$\bar{\nu}_p$ (^{252}Cf) = 3,732	"	0,6
			^{241}Pu		
[5]	0,52—14,8	5	$\bar{\nu}_p$ (^{252}Cf) = 3,764	"	1,3
[18]	1,87—14,79	23	$\bar{\nu}_p$ (^{252}Cf) = 3,732	"	0,6

TABLE 2. Result of Estimating the Energy Dependence of $\bar{\nu}_p$ for the Fission of ^{239}Pu Nuclei by Neutrons

Neutron energy, MeV	2,53·10^{-8}	0,1	1,54	5,12	10,8	15,0	20,0
$\bar{\nu}_p$	2,870	2,878	3,078	3,587	4,510	5,039	5,574 *
Error in fitting	0,005	0,010	0,009	0,015	0,020	0,027	
Error when the indeterminacy of the standard is taken into account	0,007	0,012	0,012	0,019	0,025	0,033	
Correlation matrix	1						
	—0,03	1					
	0,01	—0,35	1				
	0,00	0,07	—0,20	1			
	0,00	—0,02	0,06	—0,27	1		
	0,00	0,01	—0,03	0,06	—0,26	1	

Note. χ^2 = 25.33; 33 degrees of freedom.

*Value obtained taking into account the results of [16].

ic composition and by the contribution of inelastically scattered neutrons from (n, n'f) and (n, 2n'f) reactions. Correspondingly, the sections of transition from one linear segment to another are found, and refined from the condition of best description of the data, as well as by taking account of the number of measured values of $\bar{\nu}_p$ in different parts of the range.

The data obtained by each author are described by the least-squares method by means of a multipart broken curve. The values of $\bar{\nu}_p$ at the chosen neutron energy are found here. The

491
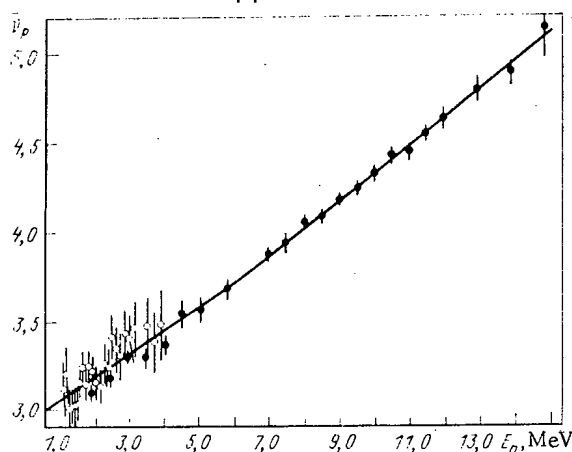
Fig. 4

Fig. 5

Fig. 4. Dependence of $\bar{\nu}_p$ in the fission of ^{240}Pu on the neutron energy E_n: data of [6] (○); data of [18] (●); the continuous curve shows the estimate obtained.
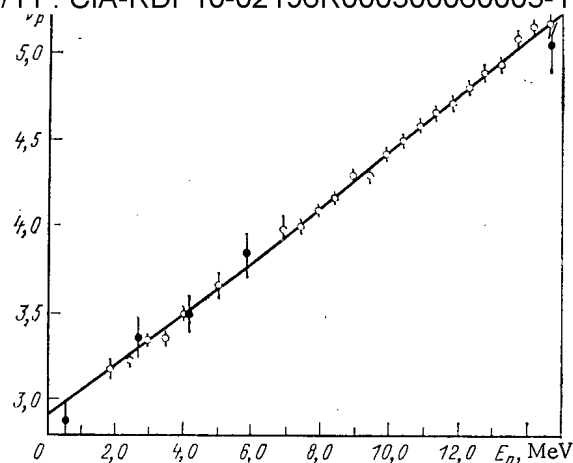
Fig. 5. Dependence of $\bar{\nu}_p$ for the fission of ^{241}Pu on the neutron energy E_n: data of [5] (●); data of [18] (○); the continuous curve shows the estimate obtained.

statistical error of the parameters obtained in this way is small, and the difference between them reflects the systematic deviation from the desired dependence. In this case, the final estimate is determined under the hypothesis of random deviation of the parameters obtained, as recommended in [21]. From the representation of the error in measuring $\bar{\nu}_p$ given in [22], it may be established that the correlation of data obtained by different authors is negligibly small. The final estimate is obtained by the least-squares method, taking account of the co-variational matrices of the parameters derived from each set of data, neglecting the correlation between the results of different authors. At this stage, account must be taken of the error most completely reflecting the indeterminacy of the given data. This results in the correct relative "weights" for the given individual authors and the reliability of the errors in the parameters. It follows from the nature of the systematic errors that the parameter values derived from each set of experimental data are determined with an error which is at least no worse than the sum of the statistical (characterized by the covariation matrices of the parameters obtained in description by the least-squares method) and systematic errors of the given measurement. This is weakly dependent on the number of experimental points. In the first approximation, the energy dependence of the systematic error may be neglected. Therefore, in the least-squares method, the input covariational matrices of the parameters are multiplied

$$\gamma^{(k)} = (1 + \sigma^2_{\text{system}} / \sigma^2_{\text{statist.}}), \tag{1}$$

where σ_{system} is the systematic error of the measurements; $\sigma^2_{\text{statist}}$ is the minimal diagonal term of the covariation matrix of the parameters obtained in describing the data of the k-th author. In taking account of the systematic errors in this way, the error of the estimate is reduced in accordance with the number of independent measurements but not the number of individual experimental points.

Tables 2 and 3 give the values of χ^2 individual experimental points, and the corresponding number of degrees of freedom (NDF). If $\chi^2/$NDF ≤ 1, the sets of parameters employed at least do not contradict the assumption of a normal distribution law, and the errors assumed, taking account of Eq. (1) take satisfactory account of the existing discrepancies. If the discrepancy significantly exceeds the input errors and there is no basis for increasing the error of a particular set of data, the recommendation of [23] must be used: an increase in the error of the estimate obtained until the existing discrepancies are covered is proposed. This has been done in estimating $\bar{\nu}_p$ for ^{240}Pu. As yet, the approach of taking account of the systematic discrepancies within the framework of statistical methods has not been developed [23]; therefore, their proposed use may be regarded as one of the possible options. The systematic errors of individual sets of data are shown in Table 1.

The data and results of estimation are normalized in accordance with the mean number of spontaneous neutrons in the spontaneous fission of ^{252}Cf [24]

492

Tables 2-3 give estimates of $\overline{\nu}_p$ for the chosen neutron energy; the errors obtained in fitting; the errors when the indeterminacy of the standard is taken into account; the correlational matrix of the values of $\overline{\nu}_p$; values of χ^2 and the number of degrees of freedom corresponding to the number of parameters derived from each set of data.

The indeterminacy of the standard is taken into account by means of multiplication of all the fitting errors by

$$\gamma^{(st)} = (1 + \sigma^2_{stand}/\sigma^2_{fit})^{1/2}, \tag{3}$$

where σ_{stand} is the error of $\overline{\nu}_p^{SP}(^{252}Cf)$ in Eq. (2); σ^2_{fit} is the smallest diagonal term of the covariational matrix of the parameters obtained in fitting.

Results for ^{239}Pu

The data employed and the results of the estimate are shown in Tables 1 and 2 and in Figs. 1-3. Six parameters are chosen for the description of the dependence $\overline{\nu}_p(E_n)$. At energies less than 0.1 MeV, as well as the data of [11] (Fig. 1), results have been obtained only for energies <100 eV. More detailed description in this range is inexpedient (see Fig. 1, where the results of three series of measurements from [11] are shown).

In estimating $\overline{\nu}_p$ for neutrons of energy <0.3 eV, the weighted mean obtained in [19] from the results of measuring $\overline{\nu}_p$ in fission by thermal neutrons renormalized to take account of the correction for the thickness of the fissile material layer are used. In accordance with [25], the preliminary results of [11] are reduced by 0.25%. The data of [17], obtained with absolute calibration of the detector efficiency, are renormalized to take account of the value of $\overline{\nu}_p(^{252}Cf)$ measured on the same experimental apparatus [26].

In the estimate, the systematic errors of [4, 5, 7] are slightly increased. At a neutron energy of 20 MeV, $\overline{\nu}_p$ is calculated in the range 15-20 MeV, taking account of the slope of the dependence $\overline{\nu}_p(E_n)$ obtained from the data of [16].

It follows from Table 2 and Figs. 1-3 that the sets of data employed are in agreement with one another and the errors obtained for the estimates are realistic. The relative error of the estimates of $\overline{\nu}_p$ in the range 0-15 MeV is no more than 0.5%. The error in $\overline{\nu}_p$ at 20 MeV is 1.5-2%. For ^{240}Pu and ^{241}Pu, the experimental data are insufficiently detailed, and therefore only three parameters corresponding to the description of $\overline{\nu}_p$ below and above the threshold of (n, n'f) reaction are estimated.

Results for ^{240}Pu

The discrepancy between the two sets of data employed (Table 3, Fig. 4) exceeds the experimental error. There is no sufficient basis for the assertion that the results of a particular measurement are correct, and the final errors are increased.

TABLE 3. Result of Estimating the Energy Dependence of $\overline{\nu}_p$ in the Fission of ^{240}Pu and ^{241}Pu Nuclei by Neutrons

Parameter	^{240}Pu			^{241}Pu		
Neutron energy, MeV	0,5	6,0	15,0	$2,53 \cdot 10^{-8}$	6,0	15,0
$\overline{\nu}_p$	2,990	3,711	5,104	2.922	3,782	5,175
Error in fitting	0,029	0,025	0,032	0,007	0,028	0,030
Error when the indeterminacy of the standard and the discrepancy of the data are taken into account	0,058	0,050	0,064	0,008	0,032	0,034
Correlation matrix	1			1		
	-0,47	1		-0,06	1	
	0,22	-0,47	1	0,03	-0,41	1

Note. $\chi^2 = 8.96$ with five degrees of freedom for ^{240}Pu and $\chi^2 = 4.53$ with seven degrees of freedom for ^{241}Pu.

TABLE 4. Estimated Dependence of ν_p for
for ^{238}Pu and ^{242}Pu

Parameter	Neutron energy, MeV			
	0,0	0,5	6,0	15,0
$\bar{\nu}_p$ (^{238}Pu)	2,840	2,910	3,674	5,006
$\bar{\nu}_p$ (^{242}Pu)	2,869	2,949	3,829	5,224

Results for ^{241}Pu

Since the sets of data considered (Table 3, Fig. 5) agree, only the indeterminacy of the standard is taken into account in Table 3. In estimating ν_p in the thermal energy range, as for ^{239}Pu, the results of [19] are used. Both for ^{239}Pu and for ^{241}Pu, the values and errors of ν_p obtained in the thermal energy range agree with the estimates of [24].

In obtaining estimated dependences for ^{238}Pu and ^{242}Pu, parameters of the systematics of [20] are used, taking account of the value of $\bar{\nu}_p^{SP}$(^{252}Cf) in Eq. (2) and the agreement of the values of ν_p with the estimates obtained for the other plutonium isotopes. The systematics of [20] is based on Taylor-series expansion of $\bar{\nu}_p$ with a center corresponding to the fission of the ^{235}U nucleus by neutrons. Comparison of the values of $\bar{\nu}_p$ for nuclides of adjacent nucleonic composition refines the estimate obtained. The error in $\bar{\nu}_p$ (Table 4) is ~3%, in accordance with [20].

The results of the present work may be compared with the estimates of [27]. The values of $\bar{\nu}_p$ obtained in [27] are renormalized in accordance with Eq. (2). For ^{239}Pu, the difference in the estimates of ν_p in the neutron-energy range 0-1.5 MeV is no greater than 0.2%; in the range 1.5-15 MeV, the difference is no more than 1.2%. Estimates of ν_p for ^{240}Pu differ by 0.9-1.9% at neutron energies of 6 MeV and by 0.8% at a neutron energy of 15 MeV. This is because of the difference in taking account of the diverging data (Fig. 4). The difference in the estimates of $\bar{\nu}_p$ for ^{241}Pu is no greater than 0.2% at a neutron energy of 6 MeV and reaches 0.7% at 15 MeV.

LITERATURE CITED

1. F. Manero and V. Konshin, At. Energ. Rev., 10, No. 4, 637 (1972).
2. V. V. Malinovskii, V. G. Vorob'ev, and B. D. Kuz'minov, Vopr. At. Nauk. Tekh., Ser. Yad. Konst., No. 5(54), 19 (1983).
3. J. Hopkins and B. Diven, Nucl. Phys., 48, 433 (1963).
4. D. Mather, P. Fieldhouse, and A. Moat, Nucl. Phys., 66(1), 149 (1965).
5. H. Conde, J. Hansen, and M. Holmberg, J. Nucl. Energ., 22, 53 (1968).
6. M. V. Savin, Yu. A. Khokhlov, Yu. S. Zamyatnin, and I. N. Paramonova, in: Nuclear Data for Reactors. Proceedings of a Conference in Helsinki, 1970, Vol. 2, IAEA, Vienna (1970), p. 157.
7. D. Mather, P. Bampton, G. James, and P. Nind, AWRE Report 042/70 (1970).
8. R. Walsh and J. Boldeman, Ann. Nucl. Sci. Eng., 1, 353 (1974).
9. K. E. Bolodin, V. F. Kuznetsov, V. G. Nesterov, et al., At. Énerg., 33, No. 5, 901 (1972).
10. B. Nurpeisov, K. E. Volodin, V. G. Nesterov, et al., At. Énerg., 39, No. 3, 199 (1975).
11. R. Gwin, R. Spenser, R. Ingle, et al., ORNL/TM-6246 (1978).
12. M. Soleilhac, J. Frehaut, J. Gauriau, and G. Mosinski, in: Nuclear Data for Reactors, Proceedings of Confernece, Helsinki, 1970, Vol. 2, IAEA, Vienna (1970), p. 145.
13. M. Soleilhac, J. Frehaut, J. Gauriau, and G. Mosinski, "Average number of prompt neutrons and relative fission cross sections of ^{235}U and ^{239}Pu in the 0.3 to 1.4 MeV range," Data EXFOR 20.568 (1980).
14. M. Soleilhac, J. Frehaut, and J. Gauriau, J. Nucl. Energ., 63, 257 (1969).
15. J. Frehaut, G. Mosinski, and M. Soleilhac, "Recent results on nu-prompt measurements between 1.5 and 15 MeV," DATA EXFOR 20.490 (1980).
16. J. Frehaut, "Nu-bar results at Bruyeres-le Chatel (March 1976)," Data EXFOR 21.685 (1980).
17. Zhang Huan-Qiao, Xu Jin-Cheng, Liu Zu-Hua, et al., J. Chin. Nucl. Phys., 2, No. 1, 29 (1980); Data EXFOR 30.600 (1981).
18. J. Frehaut, G. Mosinski, R. Bois, and M. Soleilhac, Rapport CEA-R-4626 (1974).
19. J. Boldeman and J. Frehaut, Nucl. Sci. Eng., 76, 49 (1980).

21. L. N. Usachev, Single Determination of the Error of Nuclear Data. Preprint FÉI-537 [in Russian], Obninsk (1974).
22. V. V. Malinovskii, B. D. Kuz'minov, and V. G. Vorob'eva, Vopr. At. Nauk. Tekh. Ser. Yad. Konst., No. 1(50), 4.
23. R. Peelle, in: Nuclear Data for Science and Technology. Proceedings of an International Conference, Antwerp, 1982, D. Reidel, Dordrecht (1983), p. 694.
24. H. Lemmel, Status of the Thermal Cross Sections and Neutron Yields of ^{233}U, ^{235}U, ^{239}Pu, ^{231}Pu, and nu (^{252}Cf), INDC/P(83)-37 (1983).
25. R. Gwin, R. Spenser, and R. Ingle, Report ORNL/TM-7988 (1981).
26. Zhang Huan-Qiao and Liu Zu-Hua, J. Chin. Nucl. Phys., 1, 1 (1971).
27. G. V. Antsipov, V. A. Kon'shin, and E. Sh. Sukhovitskii, Nuclear Constants for Plutonium Isotopes [in Russian], Nauka i Tekhnika, Minsk (1982).

CONTROL OF THE ^{235}U CONTENT OF GRANULATED FUEL

I. I. Kreindlin, V. S. Novikov, S. A. Popov,   UDC 621.039.542:620.16:621.039.542.342
A. A. Pravikov, B. A. Solov'ev, and A. S. Shtan'

Recently, interest has developed in microspherical fuel [1]. In particular, it can be used in high-temperature, gas-cooled reactors, HTGCR [2]. The microspherical fuel in this case consists of fuel particles — granules — of practically spherical shape, having several layers of pyrolytic carbon and silicon carbide coatings [3]. The advantages of such a fuel, often called "microscopic fuel elements," lie in the very small leakage of fission products to the surrounding matrix or coolant, good thermal conductivity, and also comparative ease of preparation.

In an HTGCR, microspherical fuel is used in the form of pin or pebble fuel elements [4]. In the construction of the active core of this reactor the assurance of identical fuel content in each fuel element is of supreme importance, and this requires accurate dosing of the fissionable nuclide during fuel element manufacture. Dosing can be carried out on the basis of mass, volume, or number of microscopic fuel elements. However, in the use of such methods the accuracy of dosing is mainly dependent on the invariability of the manufacturing process as regards variation in diameter and density of the granules, and the thickness and density of the coating.

The effects of the scatter of the parameters of the microscopic fuel elements on the accuracy of dosing can be minimized by the use of radiation methods to check the amount of nuclear fuel [5-8]. For checking the amount of ^{235}U, active neutron and spontaneous-emission methods are mainly used.

Neutron methods, in which the high penetrating power of neutrons is utilized, gained popularity as a means of checking a large quantity of fissile material, completed fuel elements and fuel assemblies, and also as a means of checking irradiated fuel.

Spontaneous-emission methods, which are based on the use of γ-radiation radiometry or spectrometry, are widely used in the production, conversion, and enrichment of unirradiated uranium, and in fuel element fabrication and the solution of quite a few problems in radiochemistry [5]. The high specific yield of γ-radiation from the α-decay of ^{235}U results in a high efficiency, better metrological conditions, and spontaneous-emission methods as against neutron methods, especially when checking small nuclear fuel doses.

Among the shortcomings of these methods can be mentioned their sensitivity to the presence of extraneous γ-emitters in the samples to be analyzed and the need to calculate the self-absorption of the emitted γ-radiation because of the great density and high atomic numbers of the fissile materials.

As is known, the α-decay of ^{235}U and the β-decay of its daughter product ^{231}Th are accompanied by intense γ-radiation. In the collective spectrum there appear 102 analytical

495

lines, 50 of which are linked to the α-decay of the ^{235}U [6]. The most intense line is the one corresponding to an energy of 185.6 keV, while the yield of γ-quanta amounts to $4.3 \cdot 10^4$ $g^{-1} \cdot sec^{-1}$, or 54% of the total number of γ-quanta originating in the decay of the ^{235}U.

Additional sources of γ-radiation in the fuel are the decay products of ^{238}U, ^{234}Th, and ^{234}Pa, which have high specific activity. Their decay is accompanied by intense γ-radiation in the 60–120 keV energy range and negligible radiation in the 185-keV region and above. In addition, over the whole of this spectrum are superimposed the β-decay bremsstrahlung and the characteristic uranium radiation with energies of 94.6, 98.5, 111.3, and 114.5 keV.

Measurement of the intensity of the γ-radiation with 185.6-keV energy underlies several methods for the determination of a ^{235}U content. The most popular is the method of comparison with a standard specimen with specimen and detector having identical measurement geometries [7]:

$$C_x = C_0 \frac{N_x}{N_0}, \tag{1}$$

where C_x is the sought-for content of ^{235}U in the specimen, C_0 is the content of ^{235}U in the standard, and N_x, N_0 are the intensities of the 185.6-keV lines of the specimen and the standard, respectively.

This method is very often used with a considerable thickness of specimen, where the γ-radiation level is determined only by the contribution from the outermost layers and is intended to check specimens with fixed geometric dimensions and density. The shortcomings of the method indicated are the guarantee of a small error only within a narrow range of measurements and the necessity of employing a large number of standard.

Another popular method, which is based on the measurement of the intensity of the γ-radiation from the fuel in the 185 and 250–400-keV regions, is the one where the γ-radiation lines of the ^{238}U decay products are observed [8]. In this case, the width of the second region is chosen, as a rule, in such a way that the average frequency of the succession of impulses (hereinafter referred to as the "average frequency") from the recording of the ^{234}Th and ^{234}Pa γ-radiation in this region is equal to the average frequency of the succession of impulses from the recording of the γ-radiation from these isotopes in the 185-keV region. The ^{235}U content is then determined by the formula

$$C_x = A(N_1 - N_2), \tag{2}$$

where C_x is the sought-for content of ^{235}U in the specimen, A is the proportionality factor, N_1 is the average frequency in the 185-keV region, and N_2 is the average frequency in the 250–400-keV region. Among the advantages of the method is the fact that account is taken of the contribution of the γ-radiation from the ^{238}U decay products.

The methods described can be used to check the ^{235}U content of a batch of microscopic fuel elements intended for the fabrication of pebble fuel elements. However, in such a case no account is taken of the γ-radiation self-absorption in each microscopic fuel element or in the batch as a whole. Self-absorption in the batch can be reduced by laying out the microscopic fuel elements in a layer having the thickness of one microscopic fuel element, i.e., by creating a monolayer. The γ-radiation self-absorption in the microscopic fuel elements is governed by the high atomic numbers and high density of the material. In the case of uranium dioxide with a surface density of 10 g/cm^2, the specific yield of γ-radiation of 185.6-keV energy varies by more than 20% when the diameter of the granules is raised from 0.2 to 0.8 mm [5], making an accurate direct measurement of the ^{235}U content impossible in view of the intensity of this line.

In order to establish the possibility of compensating self-absorption by means of apparatus, an analysis of the microspherical fuel's γ-radiation spectrum is necessary. Figure 1 shows the γ-radiation spectrum of a monolayer of microscopic uranium dioxide fuel elements containing 20% ^{235}U. The monolayer was laid out on the end face of a NaI(Tl) single-crystal scintillation detector. Such a choice is explained by the high efficiency and adequate resolving power of the detector, and also by the possibility of laying out the layer of microscopic fuel elements on its face.

As follows from Fig. 1, in the spectrum two regions of high γ-radiation intensity stand out: one corresponds to the 185.6-keV γ-radiation accompanying the ^{235}U α-decay, the other in the 60–120-keV energy region consists of a bundle of lines of γ-radiation from the decay of ^{235}U, ^{231}Th, ^{234}Th, and ^{234}Pa, and of bremsstrahlung, and also of the radiation character-

istic of the β-decay of ²³⁵U, ²³⁸U, and ²²⁶Ra. The first and second regions have their maxima around 90 and 185 keV, respectively. The intensity of the γ-radiation in the 250–400-keV region and above is very small and can hardly be used for the operational control of the ²³⁵U content.

In Fig. 2 is shown the form of the spectrum versus diameter d and density ρ of the microscopic fuel element granules. The intensity of the radiation in the 90- and 185-keV regions depends mainly on the diameter and density of the microscopic fuel elements, but the character of these relationships is different. In the 185-keV region, the drop in yield of γ-radiation with increase in diameter and density is linked to the rise in self-absorption. In the 90-keV region, the rise in self-absorption with increase in diameter and density also leads to a drop in γ-radiation, but to a somewhat smaller extent. This is because the increase in the contribution of bremsstrahlung and characteristic radiation is proportional to the increase in diameter and density of the microscopic fuel-element granules. The different slope of the γ-radiation yield versus the diameter and density of the microscopic fuel elements for the various parts of the spectrum makes it possible to obtain compensation of the self-absorption by suitable apparatus.

The intensity of the γ-radiation from the monolayer of microscopic fuel elements in the 60–120- and 160–210-keV regions (customarily taken as the intensities at the 90- and 185-keV peaks) is given by the following expressions:

$$n_1 = k_1 (\alpha_5 C_5 + \alpha_8 C_8) e^{-\mu_1 \rho d}; \tag{3}$$

$$n_2 = k_2 (\beta_5 C_5 + \beta_8 C_8) e^{-\mu_2 \rho d}, \tag{4}$$

where n_1 and n_2 are the average frequencies in the 90- and 185-keV regions, respectively, in counts/sec; k_1 and k_2 are proportionality constants taking into account the actual configuration of the source and the detector, and also the latter's characteristics; α_5 is the yield of γ-radiation with an energy of 90 keV from 1 g of ²³⁵U, in quanta/(g•sec); α_8 is the yield of γ-radiation from the decay products of 1 g of ²³⁸U with an energy of 90 keV, in quanta/(g• sec); C_5 and C_8 are the ²³⁵U and ²³⁸U contents of the batch of microscopic fuel elements, respectively, in grams; μ_1 and μ_2 are the mass attenuation factors of the γ-radiation with energies of 90 and 185 keV, in cm²/g; β_5 is the yield of γ-radiation with an energy of 185 keV from 1 g of ²³⁵U, in quanta/(g•sec); β_8 is the yield of γ-radiation from the decay products of 1 g of ²³⁸U with an energy of 185 keV, in quanta/(g•sec); ρ is the density of the microscopic fuel element granules, in g/cm³; and d is the average diameter of the microscopic fuel elements, in centimeters.

The condition governing compensation of self-absorption is the solution of the system of equations (3) and (4) with respect to C_5 with the simultaneous elimination of ρd:

$$C_5 = K \frac{n_1^{\frac{\mu_2}{\mu_2 - \mu_1}}}{n_2^{\frac{\mu_1}{\mu_2 - \mu_1}}}, \tag{5}$$

where

$$K = \frac{\left[k_2 \left(\beta_5 + \frac{1 - \eta}{\eta} \beta_8 \right) \right]^{\frac{\mu_1}{\mu_2 - \mu_1}}}{\left[k_1 \left(\alpha_5 + \frac{1 - \eta}{\eta} \alpha_8 \right) \right]^{\frac{\mu_2}{\mu_2 - \mu_1}}}, \tag{6}$$

and η is the degree of enrichment of the fuel.

For the determination of C_5, knowledge of the mass attenuation factors μ_1 and μ_2 is necessary. These factors are determined experimentally by measuring two batches with different products ρd known a priori:

$$\mu_1 = \ln \frac{n_{11}}{n_{12}} \Big/ \Delta \rho d; \tag{7}$$

$$\mu_2 = \ln \frac{n_{21}}{n_{22}} \Big/ \Delta \rho d,$$

497
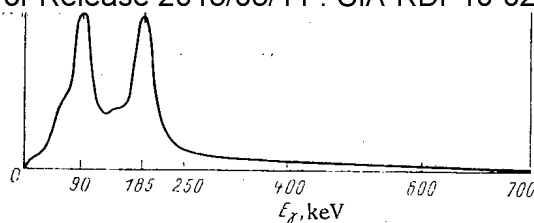
Fig. 1. γ-Spectrum of a batch of micro-
scopic fuel elements obtained on a 150-mm-
diameter NaI(Tl) scintillation detector.
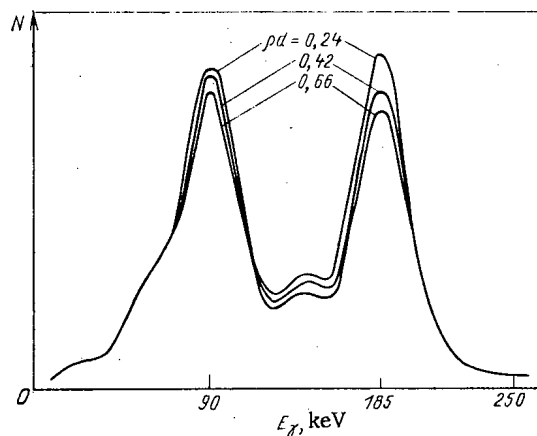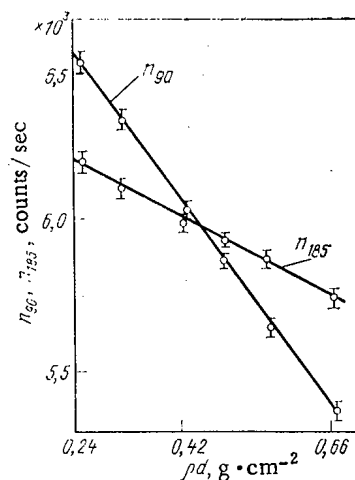
Fig. 2   Fig. 3

Fig. 2. Form of the γ-spectrum of batches of microscopic fuel elements with a 20%
^{235}U enrichment for various values of ρd.

Fig. 3. Average frequencies in various parts of the γ-radiation spectrum versus ρd.

where n_{11} and n_{12} are the average frequencies in the 90-keV region for batches with a small
and large ρd, respectively, in counts/sec; n_{21} and n_{22} are the average frequencies in the 185-
keV region for batches with a small and large ρd, respectively, in counts/sec; Δρd is the dif-
ference between the large and small values of ρd, in g/cm². In the given case, μ_1 is not the
true mass attenuation factor because it is obtained on the basis of not merely the attenuation
of the γ-radiation, but also of the generation of the bremsstrahlung and the characteristic
radiation.

The experimental verification of the method was carried out on a scintillation discrimin-
ating gamma-radiometer with a 150-mm-diameter detector using a NaI(Tl) single crystal. The
radiometer was equipped with a transformation-coefficient autostabilization system ensuring
less than 0.5% instability. At the same time, we used a pulse-height analyzer to analyze the
spectrum. For the measurements, we used six batches of microspherical fuel with a 20% ^{235}U
enrichment and ρd = 0.24-0.66 g/cm². During the measurements of a batch, it was laid out in
the form of a monolayer in the center section of the end face of the detector.

The measurements gave approximately equal average frequencies in the 90- and 185-keV re-
gions, whereas in the 250-400-keV region this frequency was approximately one order of magni-
tude less. In Fig. 3 are shown the average frequencies versus ρd in various parts of the en-
ergy spectrum, and the results of the measurements of six batches are given in Table 1. The
processing of the results was carried out by the method of comparison with standards and com-
pensation of the self-absorption. In the first case the batch with an average ρd value of
~0.42 g/cm² was taken as the standard. According to Table 1, the error amounts to approximately
10% over the range of variation of ρd when Eq. (1) is used. It is important to note that the
preparation of additional specimens with known values of ρd within the limits of the range of
interest does not make it possible to reduce the error, while the determination of the values
of ρd for the batches being checked demands labor-intensive measurements. When the method of
compensating the self-absorption in accordance with Eq. (5) is used, the error in the measure-
ment of the ^{235} content is reduced to ±1% over the entire range of ρd values.

498

TABLE 1. Results of Measurements of the ^{235}U Contents of Batches of Microspherical Fuel

Batch number	m_0, g	ρd, g/cm^2	m_1	Δm_1, %	m_5	Δm_5, %
1	0,4968	0,2418	0,5407	+8,83	0,4968	---
2	0,4932	0,3069	0,5202	+5,48	0,4893	—0,79
3	0,4956	0,4182	0,4956	--	0,4914	—0,84
4	0,4952	0,4802	0,4831	—2,43	0,4934	—0,35
5	0,4934	0,5494	0,4623	—6,3	0,4974	+0,80
6	0,4980	0,6633	0,4427	—11,09	0,4980	---

Note. m_0, mass of the batches with respect to ^{235}U; m_1, results of the measurements in accordance with Eq. (1); Δm_1, measurement error due to Eq. (1); m_5, results of measurements in accordance with Eq.(5); Δm_5, measurement error due to Eq.(5).

The method outlined for compensating self-absorption makes it possible to obtain operational control of ^{235}U content with high efficiency and low error in the pebble fuel-element production process and also in the case of microspherical fuels.

LITERATURE CITED

1. Present Scope and Prospects for the Use of Microspherical Fuel for the Manufacture of Reactor Fuel Elements Abroad [in Russian], TSNIIatominform, Moscow (1983).
2. D. Bedenig, High-Temperature Gas-Cooled Reactors [in Russian], Atomizdat, Moscow (1975).
3. R. B. Kotel'nikov et al., High-Temperature Nuclear Fuel [in Russian], Atomizdat, Moscow (1978).
4. L. E. Kostikov and V. V. Lozovetskii, Design of Fuel Elements for High-Temperature Gas-Cooled Reactors [in Russian], Énergoatomizdat, Moscow (1983).
5. V. V. Frolov, Nuclear-Physical Methods for the Control of Fissile Materials [in Russian], Atomizdat, Moscow (1976).
6. S. A. Baranov, V. M. Shatinskii, A. G. Zelenkov, and V. A. Plechin, "Study of the γ-radiation accompanying the α-decay of ^{235}U and the β-decay of ^{231}Th," Institute of Atomic Energy Preprint, Moscow (1978).
7. L. Sarkes and N. Mackinon, "Uranium enrichment can be checked by gamma-ray spectrometry," Nucleonics, 18, No. 3, (1960).
8. H. Ottmar and P. Matussek, "In-process control of ^{235}U enrichment in a WR fuel fabrication plant," Nuclear Fuel Quality Assurance, 1976 (Proc. Seminar Oslo, May 23-27, 1976) IAEA, Vienna (1976), 191-205.
9. L. S. Zazhigaev, A. A. Kish'yan, and Yu. I. Romanikov, Methods of Planning and Processing the Results of a Physical Experiment [in Russian], Atomizdat, Moscow (1978).

MIGRATION OF RADIONUCLIDES FROM THE COOLANT OF A BR-10 REACTOR

INTO STAINLESS STEEL AND THE DEACTIVATION METHOD

I. A. Efimov, A. S. Zhilkin,
A. P. Kondrashov, A. N. Mezentsev,
and A. N. Tseba

UDC 621.039.534

The process of migration and deposition of the long-lived radionuclides present in the coolant of the first circuit of nuclear reactors makes it necessary to take measures for their removal and for surface deactivation of the pipelines and the equipment.

In the fast reactors working with a sodium coolant, the maximum contribution to the radio-activity of the first circuit (after the decay of ^{24}Na) is made, as a rule, by ^{137}Cs, ^{54}Mn, ^{22}Na, ^{58}Co, ^{60}Co, ^{65}Zn, ^{95}Nb, ^{95}Zr, ^{140}La, etc.

The earlier experimental studies [1, 2] under ampul conditions showed that the radionu-clides of manganese, cesium, and zinc can penetrate from sodium into stainless steel up to a depth of 20 μm at temperatures ranging from 256 to 569°C within an experimental duration up to 1500 h. It is evident that the conditions of the ampul experiments significantly differ from those existing in a reactor. Therefore, it is difficult to apply the results of the am-pul experiments to the reactor conditions.

In this paper we present the radionuclide distribution measured across the wall thickness of the pipelines of the first circuit of a BR-10 reactor and the measured deactivation of the specimens cut out from different segments (portions) of the pipelines of the first circuit. The pipelines worked in sodium for nearly 120,000 h, and were thrice deactivated (in 1961, 1971, and 1980). The only exception was a pipeline segment (extending from the reactor up to the branching point of the circuit into two loops) which was fitted into the circuit in 1972 and in which sodium was circulated for 50,000 h. The pipelines of BR-10 were made from the 12Kh18N9T steel. In all, 12 specimens were cut out.

Table 1 shows the main parameters, characterizing the experimental conditions. We note that during the operation of the reactor the oxygen content in sodium is maintained, as a rule, at a level of $(3-10) \cdot 10^{-6}$. Other impurities in sodium (carbon, hydrogen, silicon, iron, nick-el) were periodically monitored using sodium samples; their concentration was found to be $(2-30) \cdot 10^{-6}$.

During the experiment the radioactivity of the specimen was directly measured as a func-tion of the thickness of the metal layer removed. For this purpose, metal layers were ground off from the specimen surface (over which sodium was flowing) using a microemery paper fixed in a special mold. After grinding the specimens were washed with ethyl alcohol and water. In order to avoid contamination, a new emery paper was used after each grinding operation. The minimum controllable thickness of the removed metal layer was 3–4 μm. The radionuclide con-tent in the specimens was measured based on the intensity of different lines of the γ-radia-tion spectrum. For this purpose we used a gamma-spectrometer based on a semiconductor detec-tor and an AI-4096 pulse amplitude analyzer. The error in measurements is accumulated from the errors in measuring the γ-radiation intensity and the specimen thickness. The maximum er-ror in determining the slope of the attenuation (absorption) curve of radioactivity was found to be nearly 13%.

The specimens were cut out from the pipelines and were studied after a lapse of about one year after shutting down the reactor. By this time, the short-lived radionuclides must have disintegrated. The specimens contained ^{54}Mn, ^{137}Cs, ^{134}Cs, and ^{60}Co. No other long-lived radionuclide was observed. Table 2 shows that the ^{54}Mn has the maximum activity. Deposition of the cesium and cobalt radionuclides on the wall of the pipeline was found to a less extent. The distribution of radioactivity along the segments of the circuit is different for different radionuclides. Inspection of the pipelines showed that the product on their internal surface

---

TABLE 1. Characteristics of the Segments of the BR-10 Circuit from which Specimens were Cut OUt

Segment number	Temp., °C	Circulation period of sodium, 10^3 h	Av. pumping rate of sodium, m/sec	No. of specimens
1	450	120	4	2
2	450	50	4	2
3	450	120	4	4
4	350	120	4	4

TABLE 2. Specific Radioactivity of the Precipitates on the Specimens Taken from Different Segments of the First Circuit of BR-10, 10^6 Bq/m^2

Segment number	Nuclide			
	^{54}Mn	^{137}Cs	^{134}Cs	^{60}Co
1	450	4,1	—	30
2	290	2,1	—	11
3	650	96	19	32
4	170	115	—	22
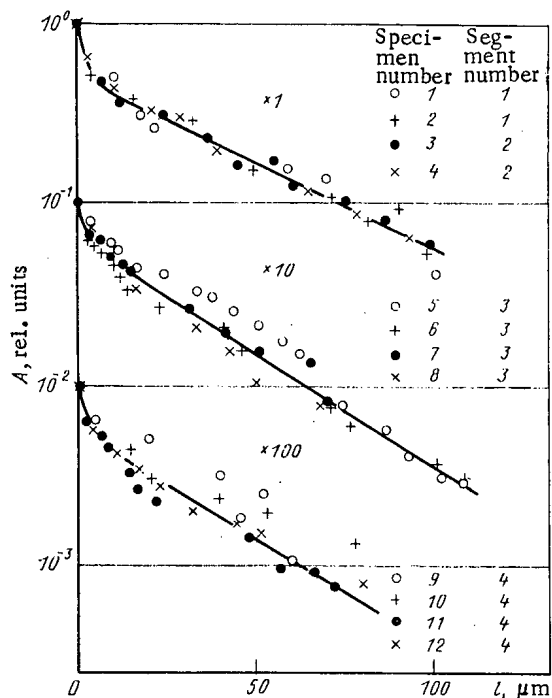
Fig. 1
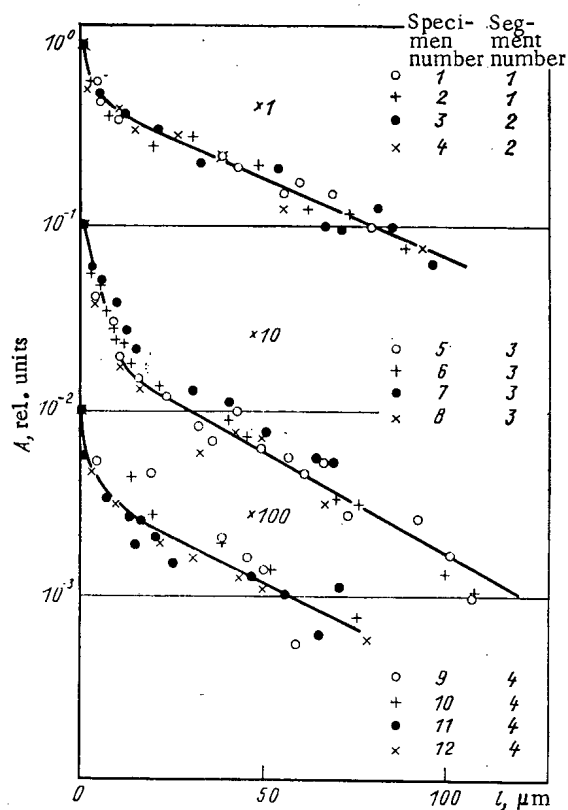
Fig. 2

Fig. 1. Radioactivity of ^{54}Mn in the specimens taken from different segments of the pipeline of the first circuit of BR-10 as a function of the thickness l of the layer removed from the surface.

Fig. 2. Radioactivity of ^{60}Co in the specimens taken from different segments of the pipeline of the first circuit of BR-10 as a function of the thickness of the layer removed from the surface.
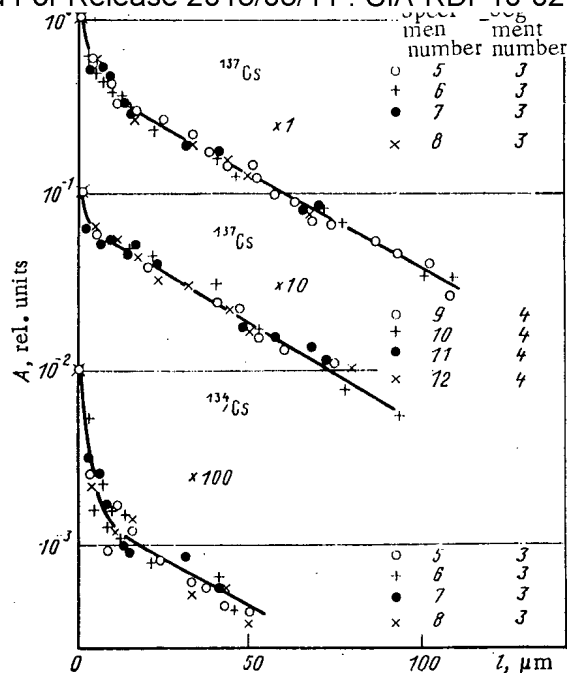
Fig. 3. Radioactivity of the cesium isotopes in the specimens taken from different segments of the pipeline of the first circuit of BR-10 as a function of the thickness of the layer removed from the surface.

TABLE 3. Relaxation Length for the 10-100-μm-Thickness Range of the Removed Layers, μm

Segment number	^{54}Mn	^{60}Co	^{137}Cs	^{134}Cs
1	46	50	—	—
2	46	50	—	—
3	35±2	39±2	43±1	41±5
4	40±4	43±4	39±3	—

has a dark and rough structure, and strongly adheres to the wall. The lustrous surface of the base metal is gradually revealed after removing a ~100 μm-thick layer. Here, dark specks (dissemination) are found on the bright surface of the metal.

Figures 1-3 show the relative change in the radioactivity of the specimen as a function of the thickness of the layer removed. It is seen from the plots that the radioactivity decreases by 3-7 times on removing a 10-μm-thick layer. In the 10-100-μm-thickness range, the variation of radioactivity of the specimen obeys an exponential law $A = A_0 \cdot \exp(-x/L)$, where A_0 is the initial activity of the specimen, L is the relaxation length, and x is the thickness of the removed layer. We note that for the first two segments of the reactor circuit, the slopes of the attenuation curves of specimen activity (the semilog plots yield straight lines) are found to be identical within the limits of experimental errors. The slope of the curves changes during the transition to the third and the fourth segments. The relaxation length for the first and the second segments amounts to 46-50 μm, and for the third and the fourth segments it varies from 33 up to 47 μm (Table 3).

In order to explore the possibility of removing the radionuclides deposited on the internal surface (decontamination) of the pipelines of the first circuit, some of the specimens were subjected to cyclic acid-deactivation. Each cycle consists of washing the specimens in the aqueous solutions of 0.3% potassium permanganate, 1% oxalic acid, and 5% nitric acid at a temperature of 90°C for a period of one hour in each solution. After one or two cycles the lustrous surface of the base metal is exposed. Table 4 shows that there is a 100 times reduction in the radioactivity of the specimen after two deactivating cycles. The corrosion prod-

TABLE 4. Effectiveness of Deactivation of the Segments of the Primary Pipelines of the First Circuit of BR-10, rel. units

Deactivating reagent	'Hot' segment (450°C)			'Cold' segment (350°C)		
	^{137}Cs	^{54}Mn	^{60}Co	^{137}Cs	^{54}Mn	^{60}Co
Steam-water wash	1	1	1	1	1	1
$KMnO_4$ treatment	0,43	0,95	0,94	0,92	0,96	1
$H_2C_2O_4$ treatment	0,33	0,49	0,73	0,32	0,22	0,28
HNO_3 treatment	0,12	0,12	0,02	0,1	0,06	0,13
After two cycles	0,01	0,01	0,007	0,01	0,05	--

ucts (manganese and cobalt) are affected to a less extent by deactivation than cesium. Such a deactivation method was tested in 1971. It showed a high degree of decontamination of the first circuits of BR-5 and BR-10 [3]. But in this case, there were large volumes of liquid radioactive wastes and surface corrosion because of the shortcomings of the method. Nevertheless, it may be recommended as an effective deactivating method for the individual parts of the first circuit system of the industrial fast reactors.

Thus, during long-term operation of a reactor with a sodium coolant, the radionuclides migrate into stainless steel up to a depth of 100–110 μm. They can be removed from the surface by acidic deactivation.

LITERATURE CITED

1. W. Brehm, P. Koehmstedt, E. Kovacevich, and D. Shannon, "Radioactive material transport in flowing sodium," in: Proc. IAEA Specialists' Meeting on Fission and Corrosion Product Behavior in Primary Systems of LMFBR's, Bensberg, FRG, Sept. 20–22 (1971), pp. 97–113.
2. N. Sagawa, M. Urata, and Y. Ozawa, "Transport and deposition of metals in sodium–stainless steel systems," Nucl. Sci. Technol., 13, No. 7, 358–364 (1976).
3. I. A. Efimov, M. P. Nikulin, A. P. Smirnov-Averin, et al., "Deactivation of the first circuit of the BR-5 reactor," in: Proc. IAEA Specialists' Meeting on Fission and Corrosion Product Behavior in Primary Circuits of LMFBR's, Dimitrovgrad, USSR, Sept. 8–11 (1975), pp. 163–172.

PREPARATION OF HOT FLUORIDE WASTES FOR STORAGE BY THE FUSION METHOD

Yu. G. Lavrinovich, A. P. Kirillovich,
M. P. Vorobei, and A. N. Lukinykh

Radioactive wastes forming during fluorine-gas regeneration of uranium oxide and uranium-plutonium fuel, are solid materials (granules, powder) based on fluoride compounds, spent sorbents (sodium fluoride), chemical absorbers (aluminum or calcium fluorides), residues of fluoridation — "cinders" (fluorides of fission and corrosion products). The spent absorber contains up to 5 mass % of calcium hydroxide or aluminum oxide which did not react with the fluorine.

The possibility of safe storage of fluorides of hot wastes (without their being reprocessed) in sealed containers with the appropriate removal of heat has been demonstrated [1-4]. Since these wastes have a low bulk density (800-1300 kg/m^3) and low heat and chemical resistance and a tendency to form dust, and since the fluoride compounds of sodium, calcium, and aluminum can also form, at the appropriate temperature and in the appropriate ratios, melts between one another and the oxides of the metals, we posed the problem of developing a method for complex reprocessing of hot wastes, which makes it possible to decrease their initial volume and increase the safety and reliability of their storage.

The results of the studies of the method of high-temperature reprocessing of fluoride wastes, obtained during regeneration of spent oxide fuel for the BOR-60 reactor, are described in this paper.

Study Method

We carried out the study of the method of thermal reprocessing of hot wastes in two stages: using model materials (fine-crystalline, chemically pure grade sodium, calcium, and aluminum fluorides; pure-grade aluminum oxide; low-activity residues of fluoridation, whose chemical composition is presented in Table 1) and using real samples (Table 2).

We studied the radiation, heat, and chemical resistance, the emergence of the radionuclides into the gas phase, and the composition of the gas phase using the methods described in [1-5]. We determined the moisture-absorbing capacity of the melts from the change in the mass of the sample after holding for 1 month in open air (moisture content from 40 to 70%). We studied the corrosion process using flat 25 × 20 × 2.5 mm samples consisting of austenitic (12Kh18N10T) and carbon (St.3) steels and NP-1 nickel, processed based on the sixth class of purity, in the medium of the melt and of the solidified melt at 1000 and 20-300°C, respectively. We made a quantitative estimate of the corrosion by using the weighing method [6].

We measured the thermal conductivity of the melts by the cylindrical-layer method [7] from the average temperature of the sample. The functional diagram of the experimental setup for fusing hot wastes is shown in Fig. 1.

Results and Discussion

We studied the meltability of the triple system NaF—CaF$_2$—cinders first for the mixture NaF—CaF$_2$ and then for the mixture NaF—cinders. The high melting temperature of CaF$_2$ (1410°C) and of the residues of fluoridation (<1100°C) did not permit studying the system CaF$_2$—cinders under our conditions. The results concerning the meltability of the system NaF—CaF$_2$, presented in Fig. 2, are in good agreement with the data in [8].

A thermal analysis of the melts based on the components NaF—cinders (Table 3) shows that samples with 40 mass % cinders have the lowest melting temperature (800°C). Visual observations established that the melts containing 40 mass % cinders have a dense homogeneous structure. In the remaining cases, gas-filled voids were observed in the structure. Based on the data obtained on the meltability of the systems NaF—CaF$_2$ and NaF—fluoridation-residues, we

TABLE 1. Chemical Composition of the Residues of Fluoridation

Component	Content, mass %	Component	Content, mass %
F	37,5	Na	0,1
Fe	50	Cr	0,1
Al	3,0	Si	0,1
Ni	5,0	U	0,4
Ca	2,1	H_2O	1,7

TABLE 2. Characteristics of the Hot Wastes

Form of wastes	Bulk density, kg/m^3	Extractability of ^{137}Cs, $g/(cm^2 \cdot days)$	Thermal conductivity, $W/(m \cdot °C)$	Heat resistance, °C
Residues of fluoridation (powder with particle sizes of 0.01-0.1 mm)	1000—1300	$(0,5—1,5) \cdot 10^{-4}$	0,24—0,5	До 200
Sorbent NaF (granules (5-6) × 6 mm in diameter)	800—900	$(1,9—8) \cdot 10^{2}$	0,33—0,48	До 500
Chemical absorber CaF_2 (granules (5-8) × 4 mm in diameter)	850—1000	$(1,4—6,9) \cdot 10^{-3}$	0,28—0,44	До 500

Note. The extractability is calculated for the apparent (end face) surface of the wastes.

TABLE 3. Heat Resistance of Melts of NaF—Ashes

Comp. of the sample, mass %		Melting temp., % °C
NaF	cinders	
90	10	985
80	20	960
70	30	905
65	35	850
60	40	800
55	45	855
50	50	910
40	60	1012
30	70	1100

separated on the triangle of the compositions of the pseudoternary system NaF—CaF_2—fluoridation-residue (Fig. 3) a region (solid line) which it is of practical interest to study and which we can study under our conditions. A thermal analysis of samples from 7 polythermal sections of the ternary system showed that a phase transition occurs at a temperature of 750-760°C. The complexity of the phase composition of the systems studied precludes an unequivocal determination of the nature of this transition. The melting temperature of the samples was equal to 770-1100°C. Using the method of isothermal sections, bounding the systems and seven polythermal sections, we constructed the liquidus surface of the system NaF—CaF_2—cinders (Fig. 4).

Since the spent chemical absorber contains some calcium hydroxide, we prepared samples containing 2, 3, 5, and 10 mass % $Ca(OH)_2$. The additions of calcium hydroxide did not significantly change the behavior of the system. The density of the samples varied from 2700 to 3000 kg/m^3 and the samples were nonhygroscopic. The optimal region of compositions of the components, determined based on model materials, was used in fusing the fluorides of hot wastes. The samples obtained for study also had a dense homogeneous structure, and their volume was 2.5-3 times lower than that of the starting materials.

Heat Resistance. The thermal stability of the melts is attributable primarily to the ratios of the components in the charge, and in the interval of optimal concentrations the melting temperature of the samples varies from 760 to 800°C.
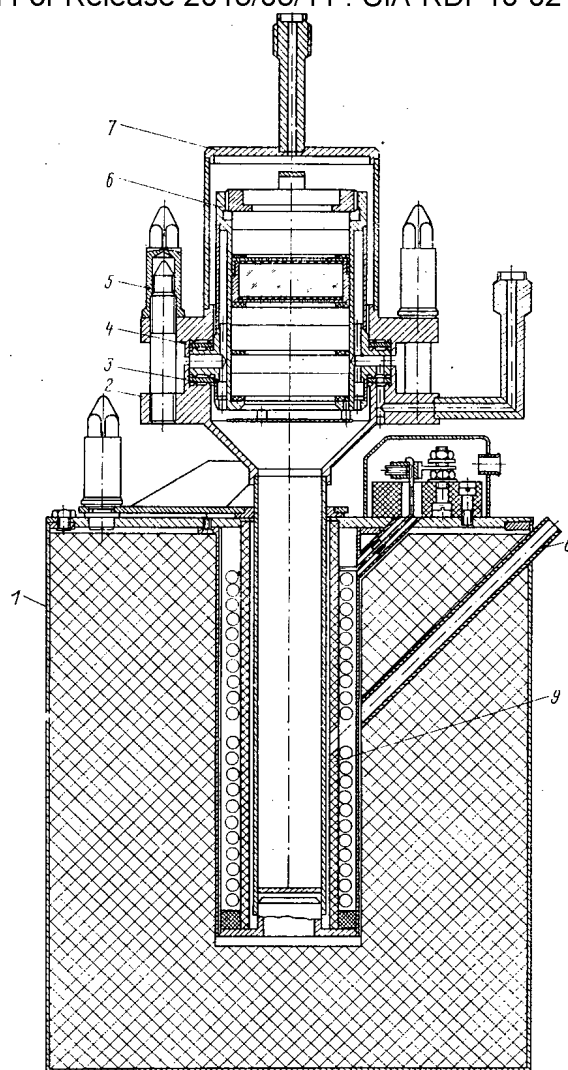
Fig. 1. Setup for studying the melting of hot wastes: 1) housing of the electric furnace; 2) crucible; 3, 4) linings; 5) clamping nut; 6) filter; 7) cover; 8) pocket for thermo-couple; 9) heater.
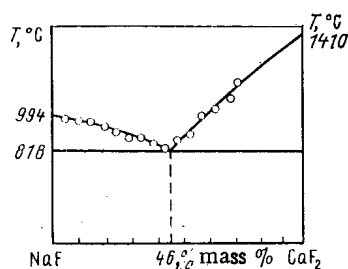
Fig. 2. Diagram of the meltability of the system.

Radiation Resistance. Liberation of gas in the container with the wastes was not observed over the period of the study with an integrated irradiation dosage of $4.4 \cdot 10^5$ Gy.

Evaporation of Radionuclides. It was experimentlly established (Table 4) that the evaporation of ^{137}Cs from the wastes increases with the temperature, but the rate of its evaporation is less than the values obtained separately for the sorbent [$4.7 \cdot 10^{-6}$-$3.1 \cdot 10^{-7}$ g/(cm$^2 \cdot$ days)], the chemical absorber ($1.3 \cdot 10^{-4}$-$1.8 \cdot 10^{-5}$ g/(cm$^2 \cdot$days) and the cinders [$1.8 \cdot 10^{-8}$-$1.8 \cdot 10^{-10}$ g/(cm$^2 \cdot$days)]. This confirms the advantage of complex reprocessing of wastes in order to improve the conditions for their safe storage.

506

TABLE 4. Evaporation of ^{137}Cs from the High-Activity Melt $(1.54 \cdot 10^{11}$ Bq/kg) as a Function of Temperature

Exptl. conditions		Rate of evaporation, $g/(cm^2 \cdot days)$
T, °C	τ, h	
20	100	$2,5 \cdot 10^{-11}$
100	100	$4,1 \cdot 10^{-11}$
200	100	$6,2 \cdot 10^{-11}$
300	100	$9,1 \cdot 10^{-11}$
400	100	$1,0 \cdot 10^{-10}$
500	100	$3,0 \cdot 10^{-10}$
600	100	$7,0 \cdot 10^{-10}$

TABLE 5. Rate of Penetration of Corrosion into the Material in Stored Fluoride Melts $(43.2\% \ NaF + 36.8\% \ CaF_2 + 20\% \ ashes)$, mm/yr

Conditions of experiment		St. 3	12Kh18N10T
T, °C	τ, ч		
20	5	9,00	7,80
20	1500	0,04	0,03
200	360	$\dfrac{0,23}{0,10}$	$\dfrac{0,15}{0,04}$
300	360	$\dfrac{0,34}{0,21}$	$\dfrac{0,21}{0,11}$

Note. The results neglecting corrosion of samples at the moment that they are filled with the melt with T = 1000°C are shown in the denominator.

Chemical Resistance. For all the complexity of the mechanism of transfer of radionuclides into the water, the degree of their extractability will be determined by the solubility of both the matrix itself and the compounds of the radionuclides. The rate of extraction of ^{137}Cs from high-activity melts with different composition is equal to $(1.6-8.8) \ 10^{-2} \ g/(cm^2 \cdot days)$.

In order to increase the chemical resistance of the samples, we studied the addition of different additives to the charge. The best results were obtained with the use of AlF_3 as well as the compounds $AlF_3 + Al_2O_3$, $AlF_3 + mica$ (muscovite), with whose help it was possible to lower the extractability of ^{137}Cs by 2-3 orders of magnitude. The melting temperature of the samples increased at the same time up to 920-940°C. One way to compensate for the introduction of the additional component (AlF_3) is to replace in the reprocessing technology the calciferous chemical absorber by alumogel, which in the process of trapping fluorine forms aluminum fluoride

Thermal Conductivity. The measured thermal conductivity of melted wastes in the range 100-400°C was equal to 0.51-0.79 W/(m·°C). Fusing the wastes increased somewhat the thermal conductivity of the final product as compared with that of the starting materials [0.2-0.5 W/(m·°C) in the interval 100-700°C]. However, the melts obtained also have a low thermal conductivity. Thus must be taken into account when selecting a system for heat removal during storage.

Corrosion studies, performed in order to select a material for the container and the melting crucible, showed that 12Kh18N10T stainless steel can be used as the structural material for containers for storing fluoride melts. The temperature of the container wall should not exceed 300°C (Table 5).

The tests of the material in the fused fluorides of the wastes (Table 6) produced significant corrosion of the St.3 and 12Kh18N10T steel samples, exceeding the indicators for simple interaction of oxygen in the air at 1000°C with these materials. The good stability of nickel,

507
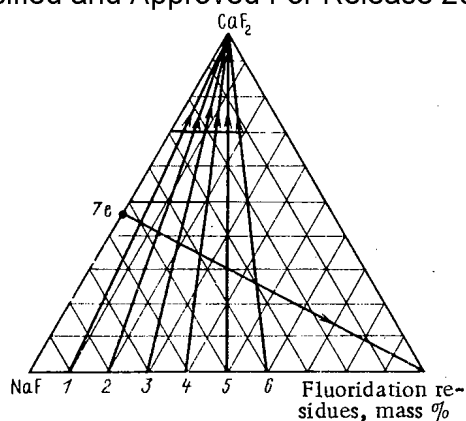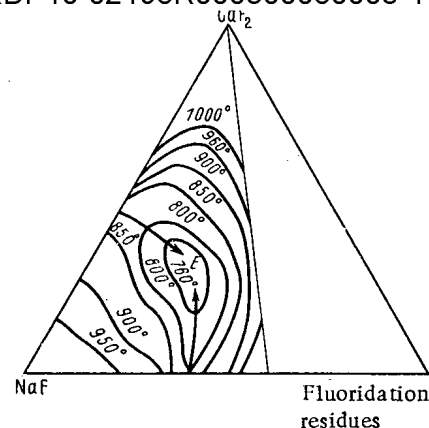
Fig. 3

Fig. 4

Fig. 3. Concentration triangle of the system $NaF-CaF_2$-fluoridation-residues; the polythermal sections and the region of compositions studied are marked.

Fig. 4. Melting diagram of the system $NaF-CaF_2$-fluoridation-residues.
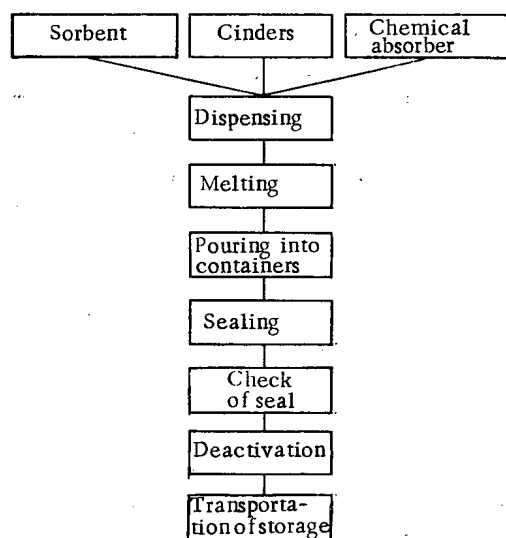
Fig. 5. Block diagram of the preparation of hot solid wastes for storage.

TABLE 6. Rate of Penetration of Corrosion into the Material in Fluoride Melts, mm/yr

Medium tested	Conditions of expt.		St. 3	12Kh18N10T	NP-1
	T, °C	τ, h			
Melt 43.2% NaF +36,8 % CaF$_2$+20 % cinders	1000	3	1240	825	11,8
Air	1000	5	716	11,4	5,6

which is the recommended material for melting crucibles, should be noted. Based on the studies performed, we proposed a scheme for preparing fluorides of hot wastes for storage (Fig. 5).

LITERATURE CITED

1. A. P. Kirillovich, Yu. G. Lavrinovich, O. V. Skiba, et al., "Study of the behavior of hot wastes from reprocessing of fuel elements from fast reactors by the gas-fluoride method," At. Énerg., 42, No. 2, 94-98 (1977).

508

2. A. P. Kirillovich, Yu. G. Lavrinovich, M. P. Vorobei, et al., "Study of the properties and behavior of hot wastes by an experimental gas-fluoride reprocessing of spent uranium–plutonium and uranium fuel for BOR-60," At. Énerg., 53, No. 1, 22-25 (1982).

3. A. P. Kirillovich, R. K. Gazizov, Yu. G. Lavrinovich, et al., "Corrosion of St. 3, 12Kh-18N10T steels and nickel (NP-1) in hot wastes from gas-fluoride reprocessing of fuel elements from fast reactors," At. Énerg., 53, No. 5, 35-39 (1982).

4. Yu. G. Lavrinovich, A. P. Kirillovich, M. P. Vorobei, et al., "Radiative, thermophysical, and physicochemical properties of wastes from experimental reprocessing of irradiated fuel for the BOR-60 reactor by the gas-fluroide method," Preprint No. NIIAR-P49(564), Dimitrovgrad (1982).

5. Method for Selecting Safe Conditions for Storing Solidified Wastes Depending on Properties and Specific Activity [in Russian], SÉV, Moscow (1973).

6. V. V. Romanov, Methods for Studying Corrosion of Materials [in Russian], Metallurgiya, Moscow (1965).

7. V. A. Osipova, Experimental Study of Heat Exchange Processes [in Russian], Énergiya, Moscow (1969).

8. Melting Diagrams of Salt Systems [in Russian], Metallurgiya, Moscow (1977), Pt. 2.

POLLUTION OF ARCTIC SEAS BY RADIOACTIVE WASTES FROM WEST EUROPEAN

NUCLEAR REPROCESSING PLANTS

S. M. Vakulovskii, A. I. Nikitin,   UDC 551.464.6.02
and V. B. Chumichev

Studies of radioactive pollution of the Norway and Barents Seas, performed by the Hydrographic Institute (FRG) in 1972 [1], revealed that in a narrow strip along the Norwegian coast and in the southwestern part of the Barents Sea the concentration of ^{137}Cs is higher than in the northern part of the sea and in the open Atlantic. This fact was explained by the flow of the radionuclide with the waters of the Norway current, polluted by radioactive wastes from nuclear reprocessing plants at Windscale and Dunree (Great Britain) and on Cape Hague (France). In 1978 an expedition of the Institute of Experimental Meteorology (USSR) discovered ^{134}Cs (concentration 0.3-0.6 Bq/m^3), which does not occur in the global fallouts and which is a significant part of the liquid radioactive wastes from the Windscale plant, in the waters of the southwestern part of the Barents Sea [2].

For purposes of establishing the characteristics of the transport and determining the limits of propagation of radioactive pollutants, created by the nuclear power industry, in the western Arctic Seas, the Barants, Kara, and Greenland Seas were inspected in August–October of 1982 during the 12th voyage of the research vessel the icebreaker *Otto Shmidt*. The basic results are presented in this paper.

The distribution of the sampling stations is shown in Fig. 1. To determine low values of the concentration of ^{134}Cs, used as tracer for studying the propagation of pollutants, samples of surface waters with volumes ranging from 1000 to 3000 liters were taken at most stations and concentrated.

We concentrated ^{137}Cs and ^{90}Cr from volumes of 100-200 and 10-30 liters, respectively. At most stations water was also taken at depths of 50, 100, and 300 m and in the bottom layer. The basic means for obtaining samples, the method used for concentrating, and the measuring apparatus was described previously in [3]. For a 2200-liter sample and with a measurement time of 480 min the minimum detectable concentration of ^{137}Cs or ^{134}Cs was equal to 0.08 Bq/m^3. The data on the concentration of industry-produced radionuclides in surface waters of the water atea studied are presented in Table 1. Figure 2 gives examples of the depth profiles of ^{137}Cs and ^{90}Sr concentrations.

The study confirmed that in the western Arctic Seas the radiation environment is affected by inflow of water from the Norwegian coastal flow, polluted with radioactive wastes. The an-
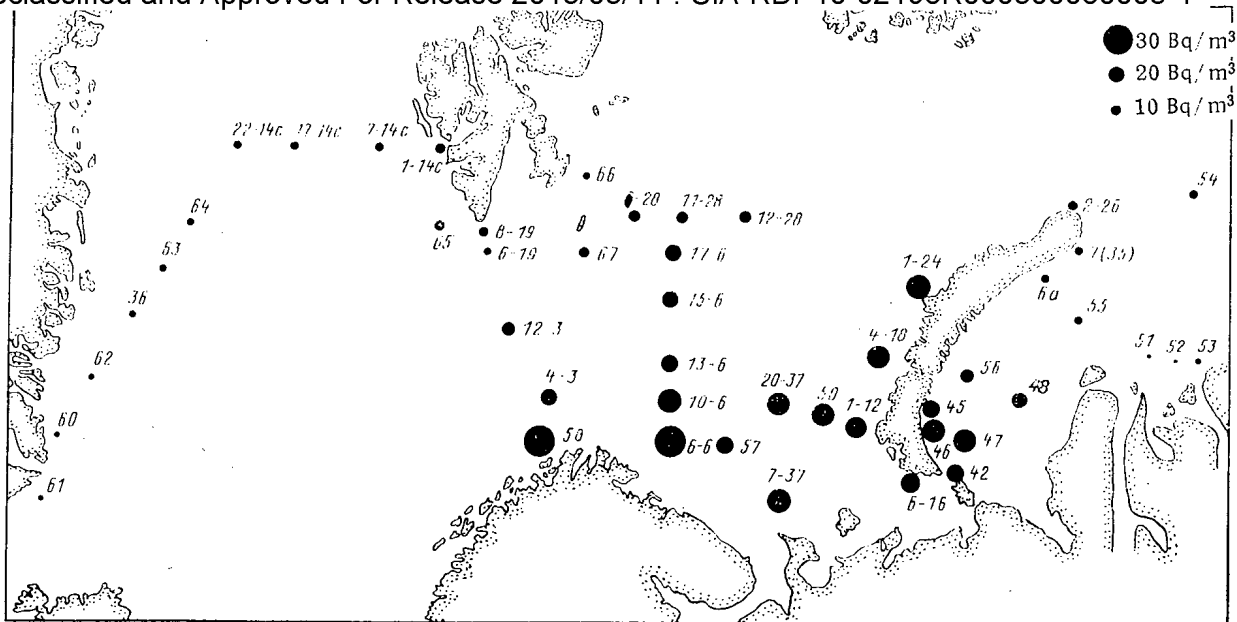

Fig. 1. Distribution of the sampling stations and the distribution of the ^{137}Cs concentration in surface waters (the diameter of a circle is proportional to the concentration). For stations on standard hydrological sections the station number is shown on the left and the section number is shown on the right.
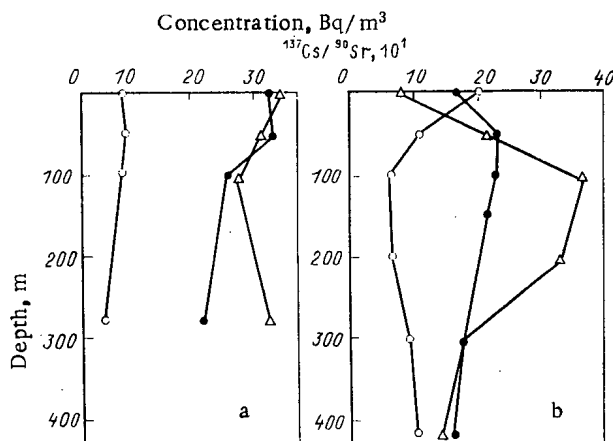

Fig. 2. Depth profiles of the concentration ^{137}Cs and ^{90}Sr as well as the ratio ^{137}Cs/^{90}Sr for the stations 6-6 (a) and 56 (b): ●) ^{137}Cs; ○) ^{90}Sr; △) ^{137}Cs/^{90}Sr.

omalously high concentrations of ^{137}Cs were recorded in the southern part of the Barents, Kara, and in the eastern part of the Greenland Seas. ^{134}Cs was also present in the water. The ^{134}Cs content in waters flowing into the Barents Sea exceeds 30 Bq/m^3, which is 6 times higher than the level of global pollution of the waters of the north Atlantic. Most of the pollutants enter the Barents Sea with the waters of the coastal branch of the North Cape current. Thus, the ^{134}Cs concentration in the surface waters at station 58 (coastal branch) is 1.7 times higher than the concentration at station 4-3 (the North Cape current itself). The spreading of the pollutants in the Barents Sea is determined by the direction of the dominant flows (Fig. 3). The highest ^{137}Cs concentrations are characteristic for the southern and southeastern parts of the sea.

Polluted water masses enter the Kara Sea through the southern Novaya Zemlya Straits. Practically the same values of the ^{137}Cs concentration are observed in the waters of the southwestern part of this sea as in the southern part of the Barents Sea. The ^{137}Cs concentrations in the freshened surface waters at the center of this sea are low and near the estuaries of the Ob' and Enisei rivers are equal to only 3-6 Bq/m^3. An analysis of the depth profiles of the ^{137}Cs concentration in the Kara Sea showed that the polluted waters of the Barents Sea flow
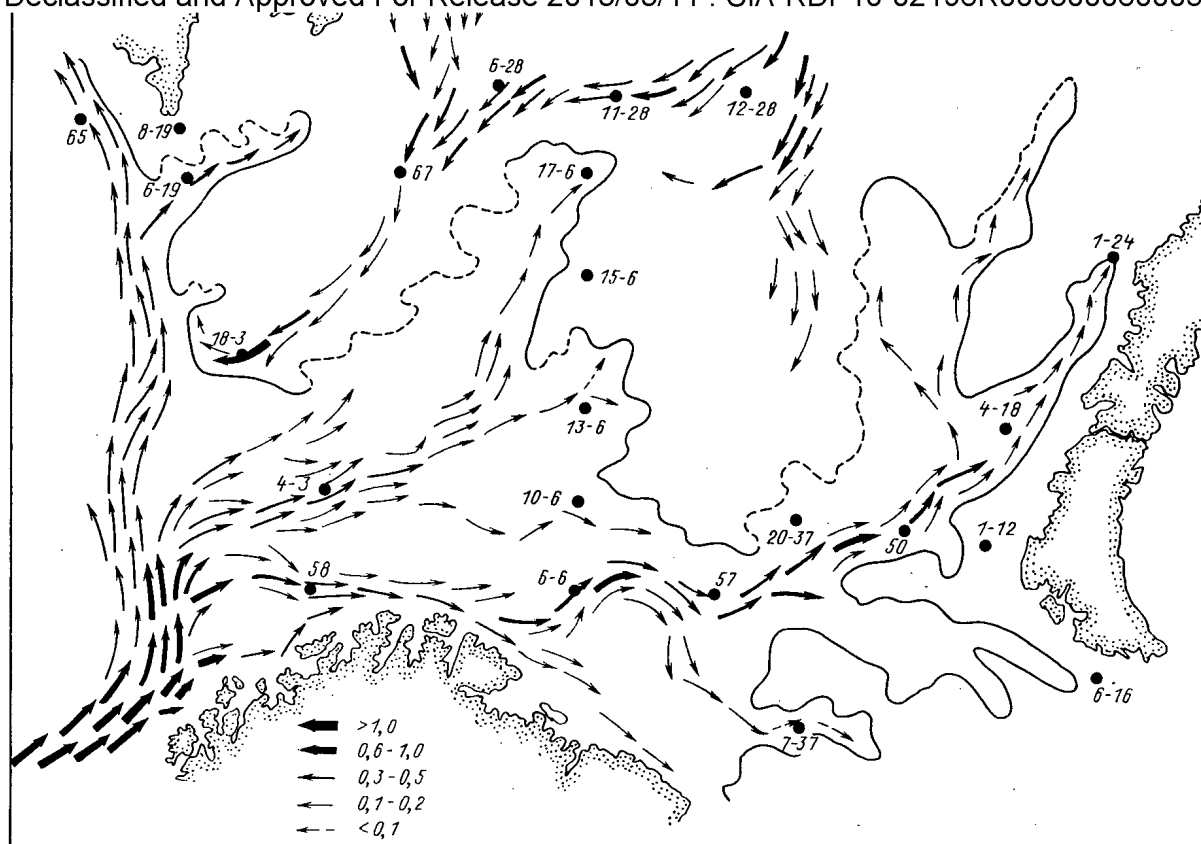
Fig. 3.   Diagram of the predominant surface flows of the Barents Sea.   The arrows in-
dicate the direction and velocity (at the nodes) of the flows.

out under the layer of freshened surface waters and flow toward the northeast at a depth of
50-100 m. ^{134}Cs was also recorded at the extreme northern point of the water area investiga-
ted (station 54).   Additional field studies will be required to make a final determination of
the boundaries and propagation paths of radioactive pollutants.

The effect of the transport of polluted water masses on the radiation environment is not
as sharply manifested in the Greenland Sea as in the Barents and Kara Seas, but it is still
very noticeable against the background of the global source. The ^{137}Cs concentration in the
northern and eastern parts of the sea is 1.5-2 times higher than in the western part, while
^{134}Cs has been observed at the shores of Spitzbergen (stations 7-14).

An analysis of the concentration fields of ^{90}Sr leads to the conclusion that emissions
from radiochemical plants are beginning to affect the pollution of the southwest Barents Sea,
which has still not been observed.   In view of the much lower emission of this radionuclide
[4], however, this effect is not as sharply manifested as the effect noted for ^{137}Cs. The max-
imum ^{90}Sr concentrations in waters flowing into the Barents Sea are approximately two times
higher than the global level.

The depth profiles of the concentrations of ^{137}Cs and ^{90}Cr in different parts of the wa-
ter area studied are different, depending on the ratio of the Arctic, Atlantic, and river wa-
ters.   We shall study as examples two profiles which are characteristic for the southwestern
part of the Barents and western part of the Kara Seas.   In the zone of the coastel branch of
the North Cape current (see Fig. 2a) practically the entire thickness of the water is polluted.
The ^{137}Cs/^{90}Sr ratio varies over depth from 2.7 to 3.4 with an average value of 3, which is
two times higher than the value characteristic for global pollution. The depth profile of the
concentrations of ^{137}Cs and ^{90}Sr in the Kara Sea (Novozemel'skiy deep) is more complicated
(Fig. 2b).   The behavior of the curve of the parameter K, equal to the concentration ratio
^{137}Cs/^{90}Sr, indicates that the water masses are separated into three layers.   For the fresh-
ened surface waters values K < 1 are characteristic, and Barents Sea water with K ≈ 3 with
a high concentration of ^{137}Cs is found at depths of 100-200 m.   At depths greater than 300 m
K ≈ 1.5, i.e., equal to the global value. It is possible that the bottom waters of the Novaya
Zemlya trough have a different origin than the waters at depths of 100-200 m, namely, they

511

TABLE 1.   Content of ¹³⁷Cs, ¹³⁴Cs and ⁹⁰Sr
in Surface Waters of the Barents, Kara, and
Greenland Seas in August–October 1982

Station number	Date of sample, 1982	Concn., Bq/m³			Ratio	
		^{137}Cs	^{134}Cs	^{90}Sr	$^{137}Cs/^{134}Cs$	$^{137}Cs/^{90}Sr$
7—37	10.08	29	0,6	14	48	2,1
6—16	11.08	27	0,5	10	54	2,7
42	12.08	23	0,4	12	57	1,9
48	14.08	18	0,2	10	90	1,8
47	14.08	27	0,5	11	54	2,5
46	15.08	24	0,6	8	40	3,0
45	15.08	22	0,5	8	44	2,8
51	17.08	3,4	—	7	—	0,5
52	17.08	4,6	—	9	—	0,5
53	17.08	6	—	9	—	0,7
54	19.08	9	0,08	8	110	1,1
55	21.08	7	—	20	—	0,35
56	22.08	17	—	21	—	0,8
6a	24.08	8	0,07	—	110	—
7—35	24.08	13	—	—	—	—
2—26	25.08	15	—	9	—	1,7
1—24	26.08	28	—	9	—	3,1
4—18	27.08	32	—	9	—	3,6
1—12	27.08	26	—	—	—	—
50	27.08	30	0,7	—	43	—
20—37	28.08	26	0,5	7	52	3,7
57	28.08	22	0,5	8	44	2,8
6—6	29.08	33	0,7	10	47	3,3
58	30.08	37	0,9	11	41	3,4
4—3	31.08	24	0,5	6	48	4,0
12—3	1.09	17	0,2	7	85	2,4
6—19	3.09	8	—	3,6	—	2,2
8—19	4.09	6	—	3,4	—	1,8
1—14c	4.09	12	—	6	—	2,0
7—14c	6.09	9	0,09	3,5	100	2,6
17—14c	8.09	9	—	5	—	1,8
22—14c	8.09	8	—	3,6	—	2,2
36	12.02	6	—	4,6	—	1,3
60	15.09	5	—	7	—	0,7
61	18.09	4,4	—	4,1	—	1,1
62	2.10	6	—	6	—	1,0
63	3.10	8	—	3,9	—	2,0
64	4.10	4,8	—	4,8	—	1,0
65	8.10	12	—	6	—	2,0
66	9.10	8	—	3,5	—	2,3
67	10.10	11	—	3,0	—	3,7
6—28	10.10	12	—	5	—	2,4
11—28	11.10	13	—	4,2	—	3,1
12—28	12.10	14	—	6	—	2,3
17—6	12.10	18	—	7	—	2,6
15—6	13.10	21	—	7	—	3,0
12—6	13.10	22	—	13	—	1,7
10—6	13.10	25	—	7	—	3,6

consist of Atlantic waters flowing into the sea through the St. Anne Channel.   On the other hand, they could also be older Barents Sea waters with a lower ¹³⁷Cs content.

It should be noted that the presence of a radioactive indicator such as ¹³⁴Cs in measurable quantities in the waters of the Arctic Seas can be used to solve the problem of the dynamics of waters in and to identify the water masses of the Arctic Basin. We shall use this tracer to determine the transport time of the pollutants from the sampling location to the seas investigated. The method is based on the change in the values of the coefficients m, equal to the concentration ratio ¹³⁷Cs/¹³⁴Cs, as a function of time as a result of the large difference in the half lives of these radionuclides (30.1 and 2.1 years, respectively).   According to the data in [5], for emissions from the plant at Windscale in 1970–1978 the average value is m = 5.8 ± 0.6; we shall assume that the global pollution of the region with ¹³⁷Cs is equal to 6.2 Bq/m³ (the average concentration in the 0–50 m layer in the western part of the Greenland Sea).   Subtracting the value of the global pollution with ¹³⁷Cs, we obtain for the southwestern part of the Barents Sea (station 58) m ≈ 34, and the transport time is T ≈ 5.8 years.   For the southwestern part of the Kara Sea (stations 42, 45, 46, 47) including the global contamination with ¹³⁷Cs, m ≈ 39, which corresponds to T ≈ 6.2 years.

512

emis-sions from the plant at Windscale which occurred in 1976. To evaluate the fraction of annual emission of ^{137}Cs at Windscale entering the Barents Sea, we used the yearly inflow of Atlantic water $74 \circ 10^3$ km^3, determined by Timofeev [6] from observations on the section North Cape — Medvezhe Ostrova. Using the data on the depth distribution of ^{137}Cs at the southwestern bound-ary of the Barents Sea (seations 6-6, 12-3, 4-3) and taking into account the global ^{137}Cs, the average concentration of industrially generated ^{137}Cs in the water flowing into the Barents Sea (due only to radioactive emissions) is equal to 12 ± 4 Bq/m^3, while the yearly inflow of industrial ^{137}Cs ~ $0.9 \cdot 10^{15}$ Bq. The emission of ^{137}Cs at Windscale in 1976 was equal to $4.44 \cdot 10^{15}$ Bq [5]. Thus, approximately one-fifth of the yearly emission of ^{137}Cs ultimately ends up in the Barents and Kara seas. A larger fraction of the emission should be expected for ^{90}Sr because of the lower sorption of the radionuclide by bottom deposits than for ^{137}Cs [7]. The depth-averaged concentration of local ^{90}Sr at the southwestern boundary of the Barents Sea is equal to 1.8 ± 0.9 Bq/m^3 (the global level of 5.1 Bq/m^3 is subtracted out), while the yearly inflow is equal to $1.3 \cdot 10^{14}$ Bq. In 1976 the emission of ^{90}Sr at Windscale and at Cape Hague was equal to ~$4.2 \cdot 10^{14}$ Bq (the fraction corresponding to the plant on Cape Hague comprised ~10% of this amount) [4]. It is easy to see that almost 30% of the emitted ^{90}Sr flows into the Arctic Sea.

To compare the contributions of the global and local sources with the radioactive pollu-tion of the Barents Sea, we shall use the data on the fallout of ^{137}Cs and ^{90}Sr on Finland in 1980 [8] and we shall extend these data to the Barents Sea. We shall also assume that the level of fallout in 1982 was the same as in 1980: 3.6 Bq/m^2 for ^{90}Sr and 4.0 Bq/m^2 for ^{137}Cs. The fallout on water area of 1,405,000 km^2 [9] was equal to $5.1 \cdot 10^{12}$ Bq of ^{90}Sr and $5.6 \cdot 10^{12}$ Bq ^{137}Cs per year. It was shown above that due to the local source ~$0.9 \cdot 10^{15}$ Bq ^{137}Cs and ~$1.3 \cdot 10^{14}$ Bq ^{90}Sr enters the sea per year. Thus, the yearly inflow due to local pollution exceeds the inflow from fallout by a factor of 150 for ^{137}Cs and approximately 30 for ^{90}Sr.

Over the entire period from the beginning of nuclear testing up to 1978 the total deposi-tion of ^{137}Cs on the earth's surface was equal to 2740 Bq/m^2 and 1150 Bq/m^2 for the latitude belts 60-70°N lat. and 70-80°N lat. [10], respectively. These values can be used to estimate the total inflow of ^{137}Cs from the atmosphere onto the water area of the Barents Sea as a re-sult of the global radioactive fallout. Because the Barents Sea is located in both latitude belts we shall assume that an average of 1850 Bq/m^2 of ^{137}Cs was deposited on the surface of the sea, which for the surface area of the sea is equal to $2.6 \cdot 10^{15}$ Bq. Thus, the inflow of local ^{137}Cs from the Norway Sea for 1982 only is equal to ~35% of the total fallout of the radionuclide as a result of all nuclear tests performed before 1978.

The results of the studies performed in the Greenland, Barents, and Kara seas lead to the conclusion that the radioactive wastes observed there also spread into other parts of the Arc-tic Ocean. It is therefore desirable to organize systematic observations of the propagation of waters marked with the radioactive tracers in order to obtain new information about the dynamics of water masses in this extensive and inadequately studies part of the world oceans.

LITERATURE CITED

1. H. Kautsky, in: Isotope Marine Chemistry, Tokyo (1980), p. 9.
2. A. Preston, D. Jefferies, and N. Mitchell, in: Proceedings of Seminar on Radioactive Effluents from Nuclear Fuel Reprocessing Plants, Luxembourg (1978), p. 401.
3. S. M. Vakulovskii, E. N. Davydov, A. I. Nikitin, et al., "Hardware-method complex for monitoring radioactive pollution of seas and oceans," in: Proceedings of the Institute of Experimental Meteorology [in Russian], No. 6(107), Gidrometeoizdat, Moscow (1983), p. 47.
4. N. Kautsky and C. Murray, At. Energy Rev., No. 2, 63 (1981).
5. D. Jefferies, A. Steele, and A. Preston, Deep-Sea Res., 29, No. 6A, 713 (1982).
6. V. T. Timofeev, Water Masses of the Arctic Basin [in Russian], Gidrometeoizdat, Lenin-grad (1960).
7. S. M. Vakulovskii, Yu. V. Krasnopevtsev, A. I. Nikitin, and V. B. Chumichev, "Distribu-tion of ^{137}Cs and ^{90}Sr between the water and bottom deposits in the Black Sea in 1977," Okeanologiya, 22, No. 6, 966 (1982).
8. Studies on Environmental Radioactivity in Finland, 1980, Annual Report STL-A38, Insti-tute of Radiation Protection, Helsinki (1982).

9. A. D. Dobrovol'skii, and B. S. Zalogin, Seas of the USSR [in Russian], Mysl', Moscow (1965).

10. "Radioactive pollution as a result of nuclear explosions," Document OON A/AS, 82/P, 360 (1979).

SPACE–ANGULAR CHARACTERISTICS OF SECONDARY ELECTRONS
DURING GAMMA IRRADIATION

A. F. Adadurov, V. T. Lazurik,
and Yu. V. Rogov   UDC 539.124.17

Let a uniform flux of quanta be incident on a flat target of thickness h. Then the angle between the direction of quantum propagation z and the normal **n** to one of the target surfaces (Fig. 1) will be called the angle of target orientation θ. At the present time, the yields* — forward, $\eta(0)$, and backward, $\eta(\pi)$ — are sufficiently well understood (e.g., see [1-3]). However, these data are insufficient for conducting calculations of radiation effects in real structures because, for targets of complex geometry, it is necessary to know the yield dependences on the thickness and orientation of the target. This work is dedicated to the study of these dependences.

In order to perform numerical calculations of yields as functions of target thickness for various orientation angles, a computer code "UGOL" has been written. In this case, one of the realizations of the localized valuations method has been utilized [4]. The electrons generated in the process of noncoherent quantum scattering, photoelectrons from K- and L-shells, and electrons corresponding to the Auger transitions have been examined. In a single code run an assembly of 1000 electron trajectories was utilized.

A series of calculations was done for aluminum, copper, gold and silver plates, irradiated by γ-quanta of 20-, 50-, 100-, 663-, 1250-, and 2000-keV energy. Figure 2 shows the dependences of fast secondary electrons from the equilibrium aluminum and gold targets on the orientation angle. The relative statistical errors for yields $\eta(\theta)$ at $0 < \theta < \pi/2$ and $\pi/2 < \theta < \pi$ do not exceed 3 and 10%, respectively. We note that in the computational model the assumption of a steady γ-quantum flow throughout the target thickness is violated at angles close to $\pi/2$. Therefore, the angle region $\Delta\theta = \delta_e/l_\gamma \leqslant 10^{-3}$ (δ_e is the mean electron path, l_γ is the mean quantum path near angle $\pi/2$) cannot be calculated using this method.

The following empirical relations can be used for the description of yield dependences of secondary electrons on orientation angles in a broad energy interval (20 keV–2 MeV)

$$\eta(\theta) = \begin{cases} \eta(0)\,[a + (1-a)\cos\theta] & 0 < \theta < \pi/2; \\ a\eta(0) + [a\eta(0) - \eta(\pi)]\cos\theta & \pi/2 < \theta < \pi; \end{cases}$$

$$a = \left(\frac{\eta\pi}{\eta(0)}\right)^{0.35},$$

(1)

where $\eta(0)$ and $\eta(\pi)$ are the forward and backward yields for normal quantum incidence, respectively.

Analysis of the calculated results show that the proposed empirical relation describes a whole aggregate of existing data with a relative error not exceeding 10%.

The yield dependence of secondary electrons on the thickness of a silver target is shown in Fig. 3 (curve 2). The vertical lines (calculated by the Monte Carlo method) show the range of yield change as a result of target orientation angle change. It follows from Fig. 3 that the ratio of yield value $\eta(\theta, h)$ to the equilibrium one $\eta(\theta)$ is practically independent of orientation angle; therefore,

---

*Here the yield $\eta(\theta)$ is the ratio of the number of electrons emerging from the surface to the number of incident quanta.
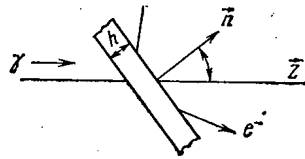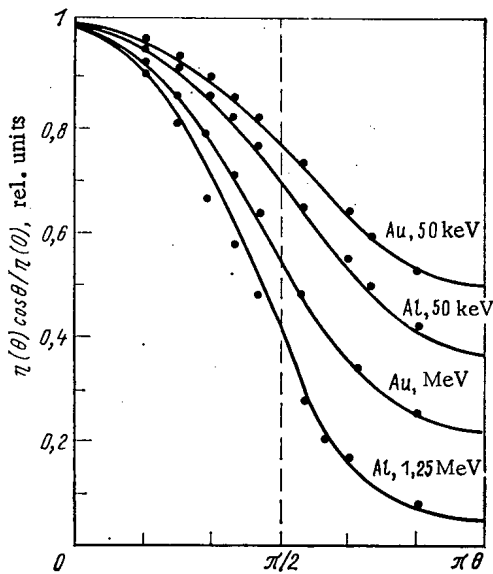
514

Fig. 1.   Calculation
diagram.

Fig. 2

Fig. 3

Fig.   2.   Dependence of secondary electron yield on target orientation angle; •)
Monte Carlo calculations; curves are calculations from expression (1); [$\eta(0)$ is the
forward yield for normal quantum incidence].
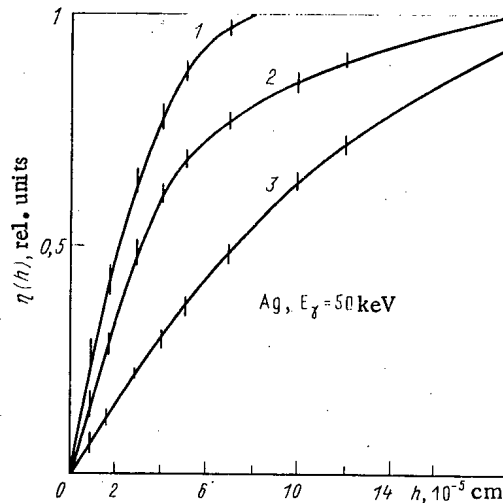
Fig.   3.   Dependence of secondary electron yields on target thickness for a quasi-
isotropic source: 1, 3) calculations from expression (3) for K- and L-photoelectrons;
2) average yield.

$$\eta(\theta, h) = \eta(\theta) f(h). \tag{2}$$

To describe the dependence of the secondary electron yield on the target thickness, we
use the following relation:

$$f(h) = \frac{2h}{R_e} - \frac{h^2}{R_e^2}, \tag{3}$$

which is correct for the case where the generated secondary electrons are monoenergetic and
isotropically distributed.   Here, R_e is the extrapolated electron path.

Figure 3 shows quantitative data and calculated dependences [using expression (3)] of
yields on target thickness for K- and L-photoelectrons generated in a silver target. Curve 2
was obtained by averaging yields for K- and L-photoelectrons in accordance with the probabil-
ity of their formation.

Analysis of the calculation results show that in the case where the photoeffect is the
dominant factor in yield formation, the proposed relations (2) and (3) describe the yield
dependence of fast electrons with a relative spread of data not exceeding those obtained with
the Monte Carlo method.

Figure 4 shows the yield dependences of secondary electrons on aluminum target thickness
for various orientation angles with irradiation by 1.25 MeV γ quanta. It follows from Fig.
4 that the division of dependences on the orientation angle and target thickness does not
occur. It is apparently, a consequence of sufficiently high anisotropy of the electron com-

515

Fig. 4. Dependnece of the secondary electron yields on thickness and orientation angle of the target in the case of an anisotropic source: o) $\theta = 0°$; Δ) $\theta = 60°$; $\square$) $\theta = 80°$; $\bullet$) $\theta = 180°$.

TABLE 1. Maximum Relative Error of the Analytical Approximations of Forward Yields, %

Energy, keV	Al	Cu	Ag	Au
100	10	10	10	10
662	25	10	10	10
1250	30	21	10	10
2000	36	27	15	13

ponent, which is observed when the fundamental process of electron formation is the Compton effect. In such a case, the simple analytical expressions could not be derived.

The relative error of yields was calculated by using the proposed empirical relations for evaluating the regions of applicability (see Table 1).

The obtained values of relative error show that expressions (1)–(3) can be used for determination of quantitative yield values in a broad range of atomic numbers and quantum energies.

LITERATURE CITED

1. M. Ya. Grudskii et al., Zh. Tekh. Fiz., 46, No. 2, 302–309 (1976).
2. P. Ebert and A. Lauson, IEEE Trans. Nucl. Sci., NS-13, No. 2, 735 (1966).
3. F. A. Adadurov and V. T. Lazurik, At. Énerg., 50, No. 3, 211–212 (1981).
4. F. A. Adadurov and V. T. Lazurik, Probl. Yad. Fiz. Kosm. Luch., No. 18, 70 (1983).

516

NEUTRON RESPONSE OF HYDROGENOUS-SCATTERER DETECTORS

M. P. Ivashkina and S. V. Chuklyaev   UDC 539.1.074.8+621.387.426(088.8)

This paper gives a calculation of the energy—angular sensitivity of hydrogenous-scatterer detectors (HSD) [1] with polyethylene dielectric and evaluates the error involved in representing the sensitivity as the product of two functions: one proportional to the neutron energy, and the other to the cosine of the angle of incidence on the detector. Nuclear-reactor measurements of the gamma sensitivity of HSDs with polyethylene dielectric of varying thickness are presented, and account is taken of the contribution of gamma radiation in the neutron signal.

Energy—Angular Neutron Sensitivity of HSDs. When an HSD with a hydrogenous scatterer of thickness d is irradiated with neutrons of energy E_n propagating at an angle Ψ to the dielectric/hydrogen-free interface (Fig. 1), the charge passing in the external circuit of the detector is composed of the charge $Q(d, E_n, \Psi)$ of recoil protons transported to the electrode, the charge induced by the dielectric space charge with a density $q(x, E_n, \Psi)$, and the charge produced by conduction currents in the dielectric; the contribution of the latter in the initial amplitude response is negligible. The space charge can then be represented as the sum of two charges distributed over the dielectric with densities $q_1(x, E_n, \Psi)$ and $q_2(x, E_n, \Psi)$. The first arises in the scatterer near the hydrogenous/hydrogen-free interface as a result of recoil-neutron transport, and the second is due to neutron attenuation throughout the dielectric. Bearing in mind that $Q(d, E_n, \Psi) + \int_0^d q(x, E_n, \Psi)\, dx = 0$, the detector sensitivity can be related to the space charge by the equation

$$K_n(d, E_n, \Psi) = -\int_0^d \left(1 - \frac{x}{d}\right) q(x, E_n, \Psi)\, dx. \tag{1}$$

Figure 1 shows that the parameters $q_1(x, E_n, \Psi)$ and $q_2(x, E_n, \Psi)$ are given by

$$q_1(x, E_n, \Psi) = -en_H \int_{\Omega_1(x)} \frac{d\sigma}{d\Omega}\, d\Omega$$

and, if $\cos \Psi \gg \mu \overline{R}_n$,

$$q_2(x, E_n, \Psi) = en_H \overline{R}_n(E_n, \Psi) \mu \cos^{-1}\Psi \exp\left(-\mu x \cos^{-1}\Psi\right),$$

where e is the electron charge; n_H is the number of hydrogen nuclei per unit scatterer volume; $d\sigma/d\Omega$ is the differential proton/neutron scattering cross section in the laboratory system; $\Omega_1(x)$ is the solid angle within which the projections of the recoil-proton paths on the direction of the unit vector $\mathbf{n}$ normal to the hydrogenous/hydrogen-free interface are larger than the scattering x from the interface; μ is the linear neutron attenuation factor of the scatterer; $R_n(E_n, \Psi)$ is the mean projection of recoil-neutron paths on the direction of $\mathbf{n}$.

The HSD energy—angular sensitivity is not in general the product of two independent functions, one of the angular and the other of the energy sensitivity. If the scatterer thickness $d \gg R_n$ (where R_n are the recoil-proton path projections on the direction of $\mathbf{n}$), however, the inductive contribution of the space charge to the detector sensitivity becomes negligible, and the sensitivity can then be separated into two functions with sufficient accuracy. In fact, setting the expressions for q_1 and q_2 in Eq. (1) and changing the order of integration, we obtain

$$K_n(d, E_n, \Psi) = en_H \sigma_t(E_n) \overline{R}_n(E_n, \Psi) \left\{1 - \frac{\cos \Psi}{\mu d}[\mu d \cos^{-1}\Psi + \exp(-\mu d \cos^{-1}\Psi) - 1]\right\},$$

imated by the following expression,disregarding neutron attenuation in the scatterer:

$$K_n(d,\ E_n,\ \Psi) = e n_H \sigma_t(E_n)\,\overline{R}_n(E_n,\ \Psi).$$

In this case it is necessary to introduce the component error of approximation θ_{ap}^{Ψ} for $K_n(d, E_n, \Psi)$. The value of θ_{ap}^{Ψ} is given by

$$\theta_{ap}^{\Psi} = \frac{\cos\Psi}{\mu d}\,\{\mu d\cos^{-1}\Psi + \exp(-\mu d\cos^{-1}\Psi) - 1\}.$$

Clearly, $\overline{R}_n(E_n,\ \Psi) = \overline{R}_Z(E_n)\cos\Psi$, and thus the approximation yields for the energy-angular sensitivity

$$K_n(E_n,\ \Psi) = e n_H \sigma_t(E_n)\,\overline{R}_z(E_n)\cos\Psi. \tag{2}$$

Here $\overline{R}_Z(E_n)$ is the mean projection of the recoil-proton paths on the direction of neutron propagation.

For neutron propagation along the normal $\mathbf{n}(\Psi = 0)$, the detector sensitivity $K_n^N(d,\ E_n)$ was calculated by assuming isotropic neutron scattering in the center-of-mass system, using the equation

$$K_n^N(d,\ E_n) = e n_H \sigma_t(E_n)\,[L(d,\ E_n) - C(d,\ E_n)],$$

where

$$L(d,\ E_n) = \frac{1}{2}\,[1-\cos^2\theta'(d,\ E_n)]\,d + 2\int_{\theta'(d,\ E_n)}^{\pi/2} R_z(E_p)\left(1 - \frac{R_z(E_p)}{2d}\right)\sin\theta\cos\theta\,d\theta;$$

$$C(d,\ E_n) = \overline{R}_z(E_n)\,[\mu d + \exp(-\mu d) - 1]/\mu d;$$

$R_Z(E_n)$ is the projection of the initial-energy recoil proton path on the direction of neutron propagation; $\theta'(d,\ E_n)$ is the recoil-proton emission angle for which $R_Z(E_p) = d$.

Taking into account the relationship between E_p and E_n ($E_p = E_n\cos^2\theta$), the value of θ' was found from the condition $R(E_n\cos^2\theta')\cos\theta' = d$ for $d < R(E_n)$ and was taken equal to zero when $d \geq R(E_n)$. In calculating $K_n(d,\ E_n)$ for a polyethylene scatterer with a density of 0.935 g/cm^3, use was made of the total proton paths $\{R(E_p^i)\}$ calculated in [2] by the Monte Carlo method for different initial energies $\{E_p^i\}$. The appropriate values of $R(E_p)$ for the energy E_p in the intervals (E_p^i, E_p^{i+1}) were found by means of the function $R(E_p) = aE_p^b$, in which the constants a and b were determined for each interval from the values of $R(E_p^i)$ and $R(E_p^{i+1})$ at the boundaries. The variation of K_n^N with E_n for different d is plotted in Fig. 2.

Figure 2 shows that the HSD energy sensitivity may be conveniently represented by an effective function proportional to E_n, i.e.,

$$K_n^N(d,\ E_n) = e n_H m_N^{eff}(d)\,E_n, \tag{3}$$

where $m_N^{eff}(d)$ is a proportionality factor.

The values of m_N^{eff} for different d were calculated for six sets of neutron spectra given in the BKS-1 library [3]. The first set consists of a classification of analytic spectra (except the $1/E_n$ spectrum) and the spectra of open-core reactors and nuclear explosions. The second, third, fourth, and fifth sets contain the classifications of fast-neutron spectra, hydrogen spectra, carbon, beryllium, and boron spectra, and metal spectra; the sixth set includes all the spectra of the other five sets. The variation of the factors m_{Ni}^{eff} with d was calculated for each neutron spectrum $f_i(E_n)$ of a set by the equation

$$m_N^{eff}(d) = \int_{E_R} K_n^N(d,\ E_n)\,f_i(E_n)\,dE_n / e n_H \overline{E}_n^i \int_{E_n} f_i(E_n)\,dE_n,$$

where $\overline{E}_n^i$ is the mean energy of the i-th neutron spectrum.

The value of $m_N^{eff}(d)$ selected for a given spectrum set was the median, $\{m_{Ni}^{eff}(d)\}$. The component error of approximation $\theta_{ap}(d)$ was introduced here, equal to the maximum relative
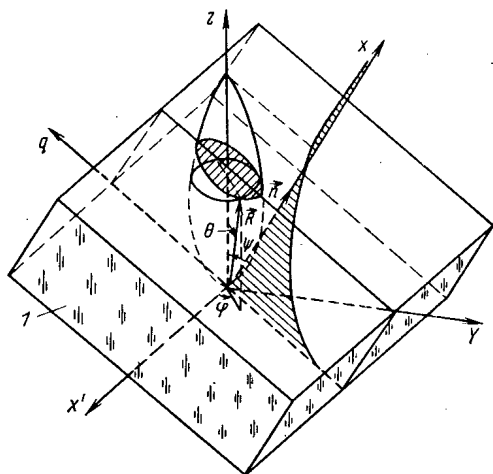
518

Fig. 1

Fig. 2

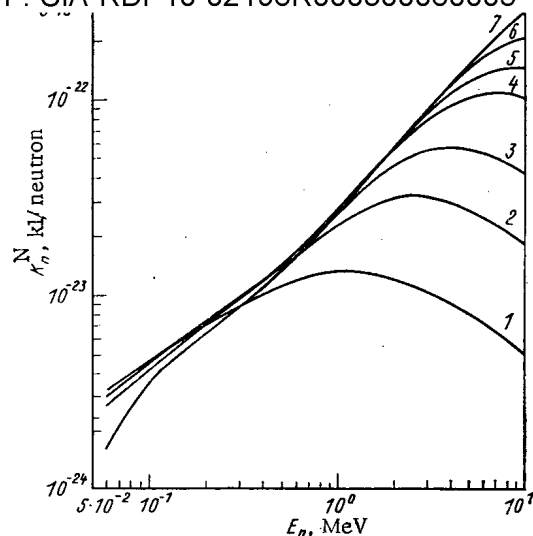Fig. 1. Diagram for the calculation of HSD sensitivity: 1) hydrogenous scatterer.

Fig. 2. Sensitivity of HSDs with polyethylene scatterer thicknesses of 0.001 (1): 0.004 (2); 0.01 (3); 0.03 (4); 0.05 (5); 0.1 (6); 0.3 (7) cm, plotted against the neutron energy for the case of normal incidence.
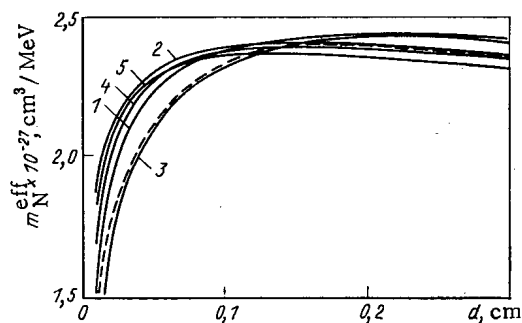
Fig. 3

Fig. 4

Fig. 3. Variation of m_H^{eff} with the polyethylene scatterer thicknesses d, plotted for the first (1), second (2), third (3), fourth (4), fifth (5), and sixth (---) neutron spectrum sets.
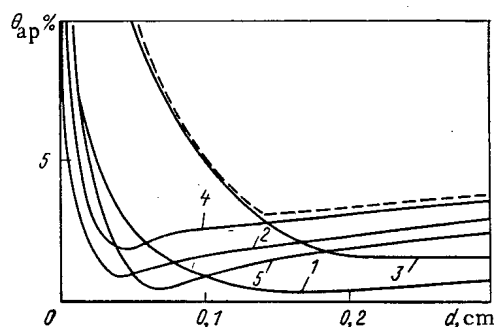
Fig. 4. Component error of approximation in representing $K_n^N(d, E_n)$ by an effective function with proportionality factor m_N^{eff}, plotted against the polyethylene scatterer thickness. The designations are the same as in Fig. 3.

deviation of $m_N^{eff}(d)$ from the median value $\{m_{Ni}^{eff}(d)\}$. The variation of m_N^{eff} and θ_{ap} with d is plotted in Figs. 3 and 4. As the figures show, the values of m_N^{eff} peak off at $d \approx 0.13$ cm, and for $d \gtrsim 0.13$ cm they slowly decrease as a result of neutron attenuation in the scatterer; at that thickness the value of θ_{ap} is within 4%. The slopes η of the m_N^{eff} vs. curves for the six spectrum sets range within 0.07, 0.18, 0.1, 0.14, 0.19, and 0.17 cm^{-1}, respectively. In view of the fact that at $d \gtrsim 0.13$ cm the values of m_N^{eff} are the highest and $\eta d \ll 1$, then for $d \gtrsim 0.13$ cm the inductive contribution of the dielectric space charge to the response becomes insignificant, and according to (2) and (3) the HSD energy—angular sensitivity for the spectrum sets considered can be described by the equation

$$K_n(E_n, \Psi) = e n_H m_{N0}^{\text{эф}} E_n \cos \Psi, \tag{4}$$

where m_{No}^{eff} is the maximum value of $m^{eff}(d)$.
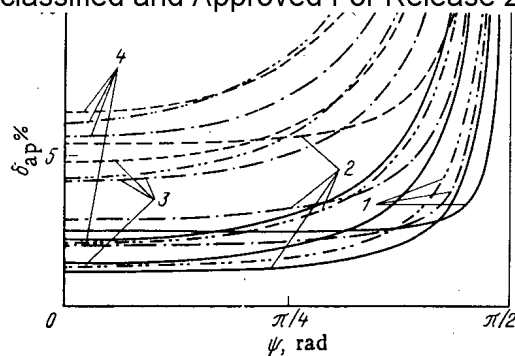
519

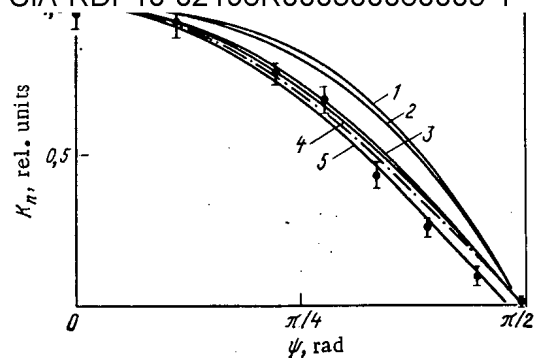Fig. 5   Fig. 6

Fig. 5. Total error of approximation in representing $K_n(d, E_n, \Psi)$ by an effective function with proportionality factor m_N^{eff}, plotted against the neutron angle of incidence on detectors with polyethylene scatterer thicknesses of 0.05 (1), 0.1 (2), 0.2 (3), and 0.3 (4) cm for several neutron spectrum sets: ———) first set; —•—•—) fourth set; —•••—) fifth set: -----) sixth set.

Fig. 6. Variation of HSD sensitivity with the neutron angle of incidence: ●) measurement data for an HSD with a polyethylene scatterer thickness of 0.032 cm; 1, 2, 3, 4, 5) calculated results for HSDs with scatterer thicknesses of 0.0005, 0.001, 0.003, 0.01, and 0.3 cm, respectively, at a neutron energy of 0.9 MeV; —•—•—) cosine of the angle of incidence.

The total error of approximation for $K_n(E_n, \Psi)$ was evaluated from

$$\delta_{ap} = \sqrt{\theta_{ap}^2 + \theta_{ap}^{\Psi^2}},$$

wherein $\theta_{ap}^{\Psi} = \eta d \cos^{-1} \Psi$. The variation of δ_{ap} with Ψ is plotted in Fig. 5. This diagram provides the means of determining the error of approximation involved in calculating the HSD sensitivity by Eq. (4) in a given geometry of irradiation.

Figure 6 shows the response curves of HSDs with polyethylene scatterers of varying thickness, plotted against the neutron angle of incidence, as calculated by the Monte Carlo method. The figure also gives the angle-of-incidence variation of the signal of an HSD with a polyethylene scatterer $3.2 \cdot 10^{-2}$ cm thick, as measured at a distance of ~1 m from the core surface of a pulsed nuclear reactor. It may be seen that as the scatterer thickness increases the HSD angular neutron sensitivity approaches a cosine curve, and fits it fairly closely when the thickness exceeds the mean projection of the recoil-proton path on the direction of neutron propagation. The experimental data are in satisfactory agreement with the calculated results.

HSD Sensitivity to Nuclear-Reactor Gamma Radiation. When an HSD is irradiated with gamma quanta, the electronic equilibrium between materials with different atomic numbers is disturbed; this occurs primarily between the hydrogenous and hydrogen-free dielectrics. As a result a signal is induced in the detector electrodes by the space charge in the dielectrics. The accuracy with which the neutron radiation characteristics of nuclear reactors can be determined thus depends to a large extent on the detector sensitivity to the accompanying gamma radiation.

Figure 7 shows the HSD signal plotted as a function of d, the signal being normalized to unit electrode area and neutron flux density; the detector had polyethylene and Teflon dielectrics of about the same thickness, in grams per square centimeter, and its electrodes were made of 0.01-cm aluminum foil. The neutron flux density and gamma dose rate were monitored in the measurements by means of a KNVK-2-5 vacuum ^{235}U fission chamber [4] placed in a 2-g/cm^2 ^{10}B shield and a vacuum secondary-emission detector with a stainless-steel emitter [5]; the mean neutron density $\overline{E}_n$ was calculated from the readings of an $^{32}S(n, p)^{32}P$ activation detector and a ^{239}Pu track detector, placed in a 1.1-g/cm^2 ^{10}B shield, by the empirical relation derived in [6] for a wide range of neutron spectra. The measurement of E_n at the location of the detectors was accurate to within 7%. Given in the figure is also the HSD specific neutron sensitivity $\overline{K}_n^N$ plotted against d, as calculated for the first and fifth spectrum sets by the equation

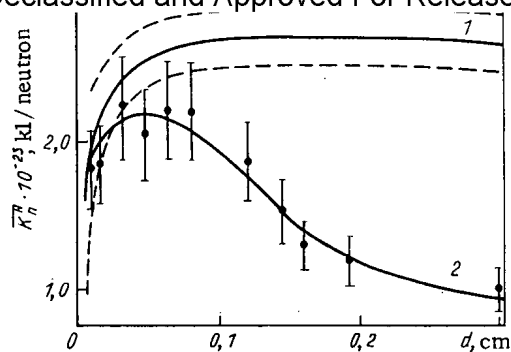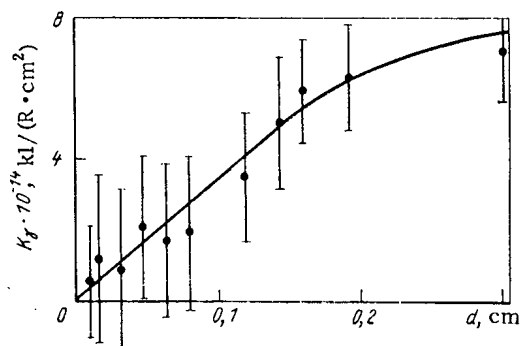$$\overline{K}_n^N(d) = e n_H n_N^{eff}(d) \overline{E}_n.$$

520

Fig. 7

Fig. 8

Fig. 7. HSD specific neutron sensitivity (1) and normalized signal per unit electrode area and neutron-flux density (2) in a pulsed nuclear reactor, plotted against the polyethylene scatterer thickness: -----) error of determination in the specific neutron sensitivity; ●) measurement data.

Fig. 8. HSD specific gamma sensitivity in a pulsed nuclear reactor, plotted against the polyethylene scatterer thickness.

The difference between the calculated and measured values is clearly due to the HSD gamma sensitivity, which is plotted against d in Fig. 8. The figure shows that when $d \leqslant 0.03$ cm the contribution of the gamma signal is under 10%, for a neutron-flux to gamma-dose ratio of $\sim 4 \cdot 10^9$ cm$^{-2} \cdot$R^{-1} $(1.55 \cdot 10^{13}$ cm$^{-2} \cdot$C$^{-1} \cdot$kg).

If an HSD with a hydrogenous catterer thickness $d \gtrsim 0.03$ cm is used, the gamma contribution to the detector signal may be appreciable. In that case it is convenient to make use of a detector design in which a gamma-sensing electrode is built into one of the dielectrics. The space charge arising in the dielectric under the effect of gamma radiation induces a signal in this electrode, which enables the gamma contribution to the signal of the neutron-sensing electrode to be taken into account by means of an oscillographic difference amplifier. Thus, for instance, in a pulsed nuclear reactor the specific gamma sensitivity of a 0.01-cm aluminum-foil electrode placed in a 0.4-cm polyethylene dielectric at a distance of 0.1 cm from the neutron-sensing electrode was (1.4 ± 0.2) 10^{-14} C/(cm$^2 \cdot$R) $[(0.54 \pm 0.008) \cdot 10^{-10}$ kg/cm$^2]$. Its neutron sensitivity is due only to neutron attenuation in the scatterer and has a value of $1 \cdot 10^{-24}$ C per neutron, i.e., a few percent that of the neutron-sensing electrode.

LITERATURE CITED

1. Yu. P. Bakulin and S. V. Chuklyaev, "A hydrogenous-scatterer detector," Prib. Tekh. Éksp., No. 4, 77-80 (1983).
2. J. Parker, P. White, and R. Webster, Nucl. Instrum. Methods, No. 23, 61-68 (1963).
3. R. D. Vasil'ev, E. I. Grigor'ev, and G. B. Tarnovskii, in: Metrology of Neutron Measurements in Nuclear-Physics Installations [in Russian], Vol. 1, TSNIIatominform, Moscow, pp. 226-252.
4. Yu. P. Bakulin, E. K. Malyshev, S. V. Chuklyaev, and O. I. Shchetinin, "A vacuum fission chamber with gamma-current compensation," At. Énerg., 54, No. 2, 123-124 (1983).
5. S. V. Chuklyaev and I. O. Shchetinin, "An externally powered vacuum emission detector for γ radiation monitoring in nuclear reactors," At. Énerg., 56, No. 4, 226-228 (1984).
6. A. Kantz, J. Appl. Phys., 34, No. 7, 1944 (1963).

POSSIBILITY OF REDUCING THE MAXIMUM DESIGN PRESSURE IN THE

CONTAINMENT VESSEL OF THE VVER-1000

N. I. Kolev   UDC 621.039.58.68

The purpose of the present paper is to show up to what extent the pressure can be reduced in the case of an accident with rupture of the main circulation pipeline in the containment vessel of a nuclear power station with a VVER-1000, by the use of a bubbling plant. An air space of 60,000 m^3 is considered, separated into a dry and a wet compartment in the ratio C = V_D/V_W, where $V_D + V_W$ = 60,000 m^3. A system is analyzed with a ring-shaped reservoir for water, the outer vertical wall of which is the inside wall of the containment vessel (Fig. 1). The connection between the dry and wet (in which the tank is located) compartments is effected by means of an annular vertical channel, joined with three vertical parallel pipelines with a length of 1.5 m and a diameter of 0.5 m, located in a single plane one above the other. Every three vertical pipes are located in 80 azimuthal sectors. The amount of water in the tank affects first and foremost its maximum heating at the end of the efflux phase (Fig. 2). The numerical results were obtained by means of the CONTEMPT-LT-26 program [1].

Rupture of the main circulatory pipeline at the inlet in the immediate vicinity of the reactor was considered. The discharge of the escaping coolant and its enthalpy are taken from [2]. Figure 3 shows the change of pressure in the dry and wet compartments in the first minute of the accident. The ratio C is used as a parameter. Figure 4 shows the dependence of the maximum pressure in the dry and wet compartments on the ratio C.

The following conclusions can be drawn from the results of the calculations.

1. For C > 2 sec, with increase of C the pressure in both compartments is increased. The difference between the values of the pressure is determined by the height of the hydroseal in the tank (distance from the water level to the uppermost point along the diameter of the highest vertical pipeline). With C ≈ 11, the pressure maximum approaches the pressure in the dry compartment of the containment vessel. Consequently, installation of the bubbler is advantageous only when C < 11.

2. With V_W = 11,000 m^3, the maximum pressure in the containment vessel is reduced by approximately 0.1 MPa by comparison with the design value of the dry safety pressure vessel. Structurally, this volume is achieved in the dry containment vessel above the crane. The separating structure, besides the inherent mass, experiences the stresses originating in consequence of the pressure difference Δp_{diff} ≈ 0.08 MPa in the course of the accident. During condensation, the pressure difference can be limited by means of return valves.

3. With V_W = 40,000 m^3, the maximum pressure is reduced by approximately 0.2 MPa. The stresses from the pressure difference increase, as in this case Δp_{diff} ≈ 0.28 MPa. Further increase of the volume of the wet compartment leads to an increase of the difference of the pressure values, which the separating structure should withstand.

By analyzing the change of pressure in the dry and wet compartments as a function of the time, with the condition of division of the discharge of the designed sprinkler device into two equal parts (50% in the dry and 50% in the wet compartment), we obtain that over approximately 2.5 min after the onset of the accident, a vacuum can be created in the dry compartment.

In conclusion, we note that the creation of a passive facility in order to reduce the maximum pressure in the containment vessel of the VVER-1000, can reduce the cost of construction of the pressure vessel, or its reliability can be increased for the same cost. With the construction of the wet compartment, with a volume corresponding to 2 < C < 11 in the contain-
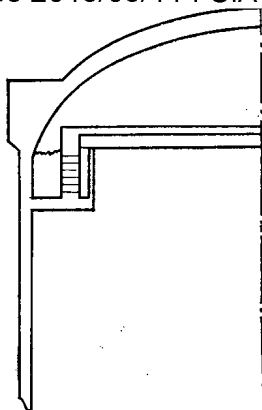

Fig. 1. Design of the ring-shaped water
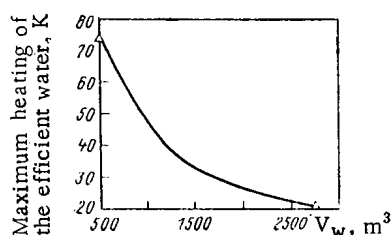reservoir.

Fig. 2. Water temperature
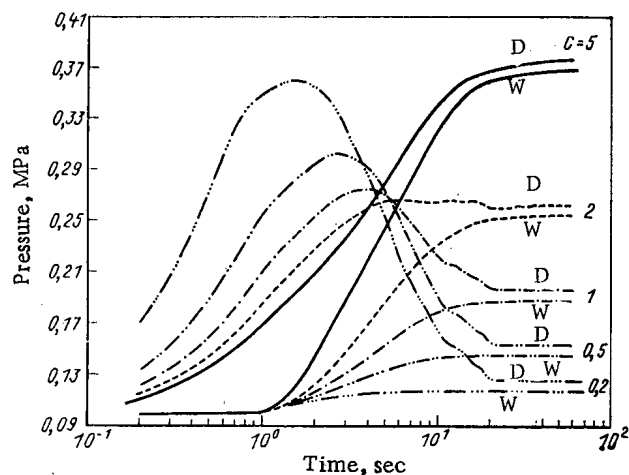at the end of the efflux
phase.

Fig. 3. Change of pressure in the dry
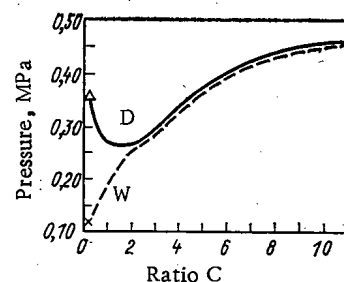(D) and wet (W) compartments.

Fig. 4. Maximum pressure in the dry (Δ)
and wet ($\times$) compartments.

ment vessel of the commercially manufactured VVÉR-1000 unit, the separating structure must be designed with consideration of both the inherent mass and also the difference of the pressure values, 0.1 MPa < $\Delta p_{diff} \leqslant$ 0.28 MPa.

LITERATURE CITED

1. L. Wheat, R. Wagner, G. Niederauer, and C. Obenhein, CONTEMPT-LT-A Computer Program for Predicting Containment Pressure-Temperature Response to a Loss-of-Coolant Accident, ANCR-1219, TID-4500.
2. A. Boyadzhiev and S. Stefanova, Investigation of the Efflux Phase in the Case of Rupture of the Main Circulatory Pipeline of the VVÉR-1000 Reactor by means of the RELAP-4 MOD 6 Program: Report of the Institute of Nuclear Investigations and Nuclear Power Generation [in Russian], Sofia (1983).

CONTENT OF ARTIFICIAL RADIONUCLIDES IN THE BODY OF SERVICING
PERSONNEL OF THE MR RESEARCH REACTOR

A. A. Moiseev, V. P. Stolyarov,   UDC 577.3:539.12.4
V. P. Polunin, I. B. Drabkina,
and V. K. Fishevskii

The MR reactor of the I. V. Kurchatov Institute of Atomic Energy is a multiloop material
testing research reactor with a 60-MW capacity, immersed in a tank with distilled water. The
reactor is intended mainly for testing the fuel elements of fuel-element assemblies and mater-
ials for new nuclear power generation plants (NPGP).

In order to conduct the tests in the reactor, loop facilities (loops) with their cooling
circulation circuits are installed, which are independent of the reactor primary circuit. While
conducting the tests, conditions are established and maintained in the loops (type and composi-
tion of the coolant, pressure, temperature, etc.) similar to the operating conditions of those
NPGP for which the tests are being conducted. During testing of the fuel elements and fuel-
element assemblies in experimental conditions, breakdown of hermeticity of the fuel-element
cans and the entry of fission products into the loop circuit is observed. In cases of the
leakage of coolant from the circuit, and also in the case of depressurization of the circuits
during recharging and maintenance operations, the fission products and activated corrosion
products can cause contamination of the working surfaces and of the air medium in the reactor
compartments, creating the conditions for the implantation of the various radionuclides in the
body of the MR reactor servicing personnel.

At the end of 1983 — beginning 1984, a representative group of personnel from this reac-
tor was investigated by means of a fixed SICh-2.2 body radiation spectrometer of the Institute
of Biophysics, Minzdrav, SSSR.

The SICh-2.2 facility, built in 1964, consists of a steel shielded chamber with dimen-
sions 1800 × 1600 × 1100 mm and a wall thickness of 150 mm. A 203YFE 102 Scintiflex with a
NaI(Tl) crystal with a diameter of 203 and a height of 102 mm, was used as the detector unit.
The energy resolution over the peak of the total absorption of photons of ^{137}Cs with an energy
of 0.662 MeV is 8%; the background count rate is 0.78 and 0.77 pulses/sec, respectively, for
the energy ranges 0.617-0.703 MeV (^{137}Cs recording channel) and 1.393-1.538 MeV (for ^{40}K re-
cording channel). The lower sensitivity threshold of the facility when measuring the content
of ^{137}Cs in the human body is $\sim$20 Bq (0.5 nCi) with a measurement duration of 30 min. The
principal error of the determination of the activity of the radionuclides in a human phantom
does not exceed 25%. In order to calibrate the SICh-2.2 facility, different types of phantoms
and canisters were used, which were filled with standard radioactive solutions of primary cat-
egory, prepared and certified in accordance with TU-I-170-71.

At the end of 1983, 131 staff were examined on the facility and, in the first quarter of
1984 — 91 staff. The analysis of the radiation spectra of the staff examined showed that
three radionuclides are detected clearly in their body: ^{134}Cs, ^{137}Cs, and ^{60}Co (Figs. 1-5).
The summarized results of the investigations carried out at the end of 1983 are given in Table
1. It was not possible to detect any other radionuclides in the bodies of the persons exam-
ined. These data agree well with the results of examinations of the staff of Soviet nuclear
power stations of a different type. Only in rare cases, in the radiation spectra originating
from a group of staff of a nuclear power station and taken by means of a semiconductor detec-
tor, can barely noticeable traces of ^{95}Zr, ^{110m}Ag and a number of other radionuclides be de-
tected.

An analysis of the data of Table 1 confirms the totally satisfactory radiation environ-
ment in the MR reactor. Even for staff carrying out work on recharging fuel elements in the
central hall, and maintenance and decontamination of plant, the content of ^{134}Cs in practice
did not exceed 30 nCi (1.1 Bq). Only in four cases out of 49 were higher levels of it record-

TABLE 1. Results of Examination of MR Reactor Staff in the Fourth Quarter of 1983

| Nature of the work performed	No. of persons examined	Content of nuclide in the body, nCi (kBq)								
		^{134}Cs			^{137}Cs			^{60}Co		
		min	max	av.	min	max	av.	min	max	av.
Recharging fuel elements, maintenance work, plant decontamination	49	<1 (0,04)	109 (4,03)	13,4 (0,49)	<1 (<0,04)	106 (3,92)	11,5 (0,42)	<1 (<0,04)	32 (1,18)	6,4 (0,24)
Maintenance and operation of technological plant of the thermal facilities in the reactor	43	<1 (<0,04)	37 (1,37)	5,5 (0,20)	<1 (<0,04)	18 (0,67)	3,0 (0,11)	<1 (<0,04)	20 (0,74)	3,3 (0,12)
Electrical plant maintenance	14	<1 (<0,04)	6 (0,22)	1,5 (0,06)	<1 (<0,04)	2 (0,07)	1 (0,04)	<1 (<0,04)	3 (0,11)	1 (0,04)
Maintenance of control and safety system and measuring instrument assembly	12	<1 (<0,04)	5 * (0,18)	1 (0,04)	<1 (<0,04)	4 * (0,15)	1 (0,04)	<1 (<0,04)	3 * (0,11)	<1 (<0,04)
Dose monitoring	11	<1 (<0,04)	30 * (1,11)	4,7 (0,17)	<1 (<0,04)	21 * (0,78)	3,5 (0,13)	<1 (<0,04)	18 * (0,67)	3,3 (0,12)
Physics and other experiments	2	<1 (<0,04)	<1 (<0,04)	<1 (<0,04)	<1 (<0,04)	<1 (<0,04)	<1 (<0,04)	<1 (<0,04)	<1 (<0,04)	<1 (<0,04)

*These extreme levels were observed for one and the same person.
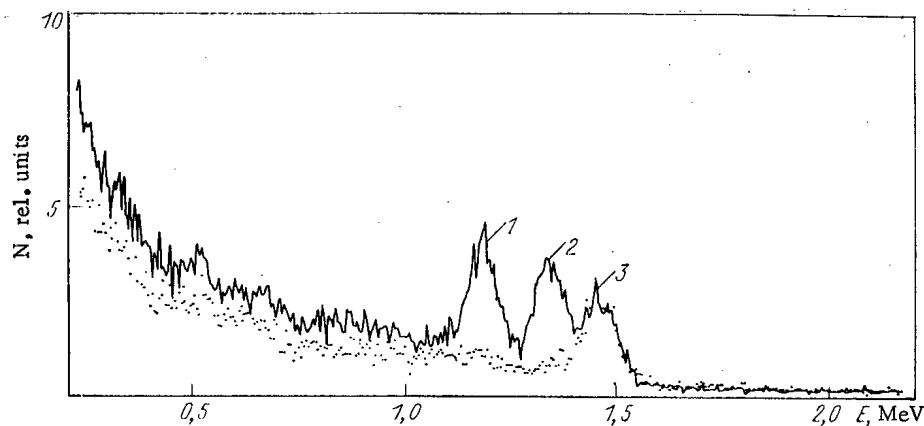
Fig. 1. Spectrum of a "clean" man (points) and an operator A (solid line): 1, 2) ^{60}Co (1.17 and 1.33 MeV); 3) ^{40}K (1.46 MeV).
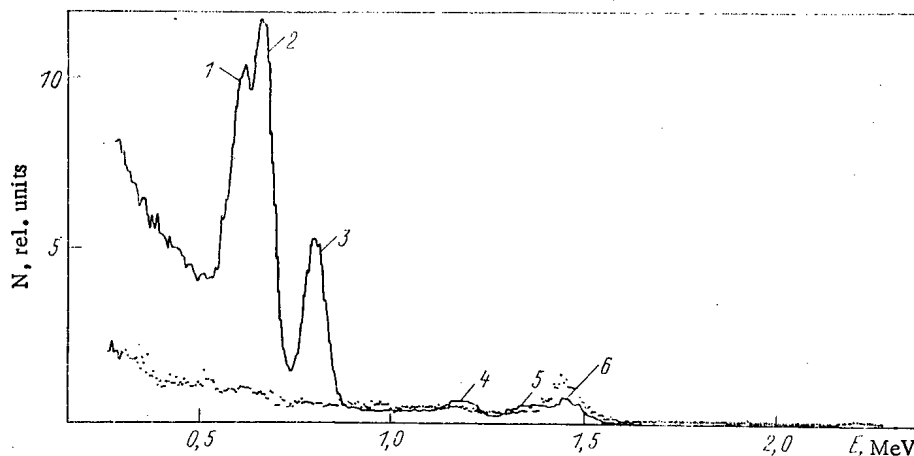
Fig. 2. Spectrum of a "clean" man and operator B: 1, 2) ^{134}Cs (0.60 and 0.79 MeV); 3) ^{137}Cs (0.66 MeV); 4, 5) ^{60}Co (1.17 and 1.33 MeV); 6) ^{40}K (1.46 MeV).

525
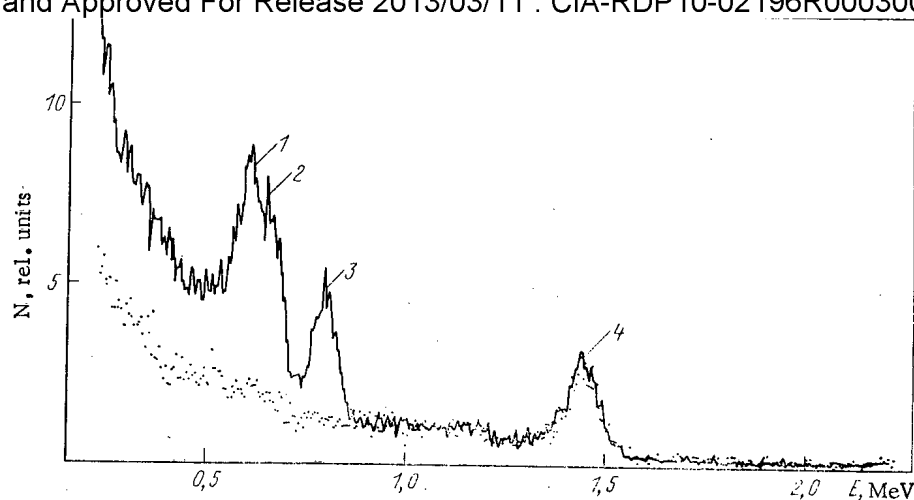
Fig. 3. Spectrum of a "clean" man and operator C: 1, 3) ^{134}Cs (0.60 and 0.79 MeV); 2) ^{137}Cs (0.66 MeV); 4) ^{40}K (1.46 MeV).
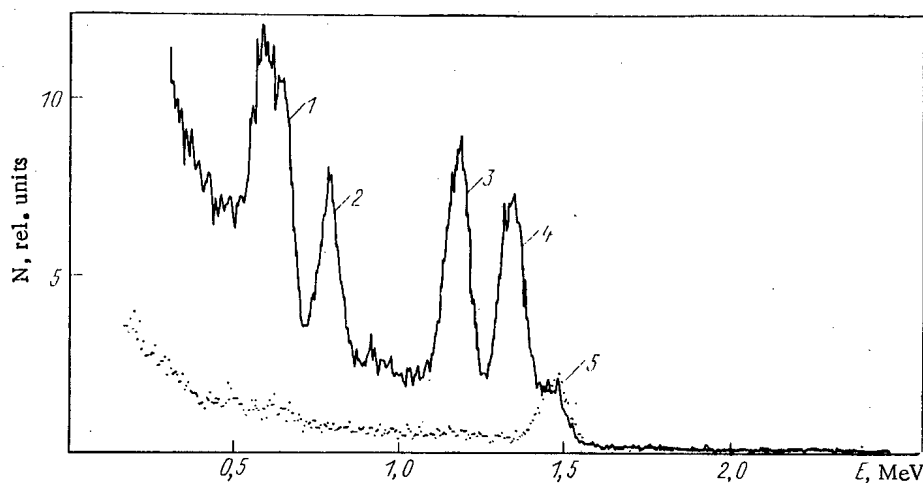
Fig. 4. Spectrum of a "clean" man and operator D: 1) ^{134}Cs and ^{137}Cs (0.60 and 0.66 MeV; 2) ^{134}Cs (0.79 MeV; 3, 4) ^{60}Co (1.17 and 1.33 MeV); 5) ^{40}K (1.46 MeV).
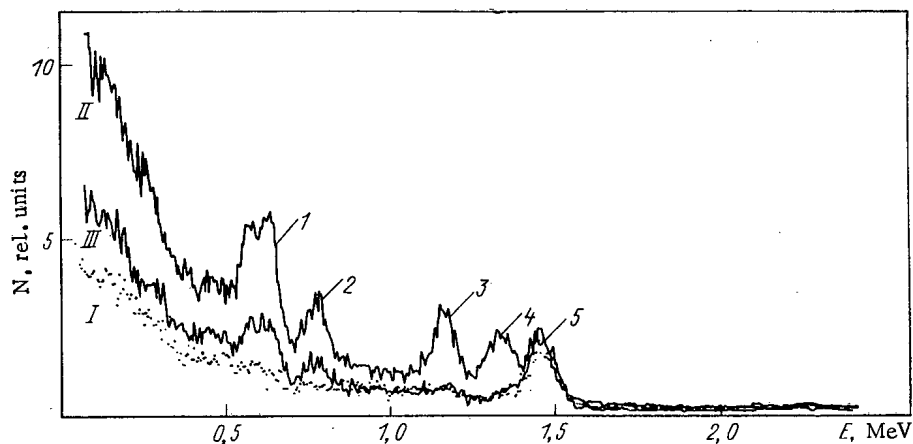
Fig. 5. Spectrum of a "clean" man (I) and the spectra of reactor staff after carrying out maintenance operations (II) and after 30 d (III): 1) ^{134}Cs, ^{137}Cs (0.60 and 0.66 MeV); 2) ^{134}Cs (0.79 MeV); 3, 4) ^{60}Co (1.17 and 1.33 MeV); 5) ^{40}K (1.46 MeV). Spectrum II contains ^{137}Cs (0.66 MeV) and ^{134}Cs (0.79 MeV) to 12 nCi (440 Bq); spectrum III contains correspondingly up to 4 nCi (150 Bq); Spectrum II contains ^{60}Co (1.17 and 1.33 MeV) 10 nCi (370 Bq).

526

^{137}Cs and ^{60}Co. In 92% (45 out of 49 cases), the content in the body of the staff examined of the first group of MR reactor personnel was less than 30 nCi (1.1 kBq); the greater part of the values lay in the range from 1 (37) to 10 nCi (370 BQ), and only in four cases are higher values noted: 38 (1.4), 47 (1.7), 48 (1.8), and 106 (3.9) nCi (kBq). As the permissible content of ^{134}Cs, ^{137}Cs, and ^{60}Co for personnel (MPC$_A$) is equal to 18 (670), 33 (1220), and 13 (480) μCi (kBq), the conclusion can be drawn that the levels revealed of the content of these three radionuclides detected in the body, in 92% of cases do not exceed 1/400 MPC$_A$, and only in individual cases does the ^{137}Cs content attain 1/100 MPC$_A$, and for ^{60}Co — 1/300 MPC$_A$. The content of these radionuclides in the body of staff of other jobs on the MR reactor (staff occupied with maintenance and operation of the technological plant of the reactor thermal facilities) is less by far. For staff engaged on the maintenance of electrical plant, automation and control systems, conducting physics and other experiments in the reactor, the contamination is almost nil.

The content of these radionuclides in the body of other staff attending the MR reactor, examined in the first quarter of 1984, on the whole was somewhat lower however, even here extremal values were noted, attaining 75 nCi (2.8 kBq) ^{134}Cs; 91 nCi (3.4 kBq) ^{137}Cs and 21 nCi (0.8 kBq) ^{60}Co.

EFFECT OF REFINEMENT OF THE NUCLEAR DATA FOR ^{238}U AND ^{239}Pu
ON THE CALCULATED CHARACTERISTICS OF A FAST REACTOR TEST MODEL

A. A. Van'kov, A. I. Voropaev,   UDC 621.039.51
and O. P. Chukhlova

New information has appeared recently concerning the resonance structure of the neutron cross sections of the heavy-element nuclides in the region of forbidden resonances. This information has been revealed as a result of an analysis of experimental data about the transmission and self-indication functions, and also the average values within the scope of the multigroup model of neutron cross sections. In particular, resonance self-screening factors and their temperature increments were refined for ^{238}U and ^{239}Pu [1, 2]. The following changes were made to the estimates of the constants by comparison with the data of BNDL-78 [3]. In groups 11 and 12, σ_γ for ^{238}U was increased by approximately 7%, the corresponding resonance self-screening factors were reduced by 2-3%, and their Doppler increments were increased by 10-30%. For ^{239}Pu in the region of forbidden resonances (groups 11-15), a tendency is observed to an increase of the resonance self-screening factors of the resonance capture and fission cross sections, and also a strong reduction (by a factor of 2 approximately) of the Doppler increment for a combination of the cross sections $(\nu - 1)\sigma_f - \sigma_\gamma$.

In order to assess the effect of these changes of nuclear data on the principal physical parameters of a fast reactor, calculations were performed on a test R-Z-model of a fast reactor [4, 5]. The core in the model has a volume of 10^3 and contains two equal-sized subzones of different enrichment. The fuel is a homogeneous mixture of UO_2–PuO_2. The thickness of the end screen is 33 cm and of the lateral screen — 47 cm. The calculated model corresponds to the start of operation of a reactor of the "Superphoenix" type on nominal power, i.e., in the breeding zone of the reactor there are no fission and plutonium products. The specification of the model is given in [5].

Further, the results are given, obtained by means of the NF-6 system (1982 version), used in the Scientific-Research Institute of Nuclear Reactors for design calculations. Two series of calculations were performed, using the BNDL-78 constants and using the group constants and self-screening factors recommended in [1, 2] in the region of forbidden resonances (11-15 groups) for ^{238}U and ^{239}Pu. For brevity, we shall denote this calculation BNDL-78N.

TABLE 1. Comparison of the Principal Phys-
ical Characteristics

Parameter	BNDL-78	BNDL-78-N
k_{eff}	1,0094	1,001
B.F.R.	1,40(1,42)	1,43(1,43)
C.B.F.	0,99(1,00)	1,01(1,01)
Effect of removal of so-dium from the core and the end breeding zone of a "cold" reactor, $\% k_{eff}$	2,04	2,40
Same, for a "hot" reac-tor,† $\% k_{eff}$	2,25	2,60
Fuel heated up from 1100°K to 2200°K, %		
initial composition	—0,58	—0,60
after removal of sodium	—0,37	—0,39
Change of k_{eff} on heating the ^{238}U in the core from 1100°K to 2200 °K‡, %	—0,63	—0,63
Change of k_{eff} on heating the ^{239}Pu in the core from 1100°K to 2200°K	0,042	0,029

*Temperature of all nuclides 1100°K.
†Temperature of uranium and plutonium nu-
clides 2200°K.
‡Temperature of all other nuclides 1100°K.

TABLE 2. Comparison of the Reaction Veloc-
ities and Material Efficiencies ρ at the
Center of the Reactor

Parameter	BNDL-78	BNDL-78-N
c^8/f^9	0,1613	0,1657
f^8/f^9	0,0224	0,0224
c^9/f^9	0,2872	0,2877
ρ^9	$24,1 \cdot 10^{-5}$	$24,1 \cdot 10^{-5}$
ρ^8	$-1,44 \cdot 10^{-5}$	$-1,42 \cdot 10^{-5}$
ρ^{Na}	$-0,140 \cdot 10^{-5}$	$-0,151 \cdot 10^{-5}$
ρ^{Fe}	$-0,175 \cdot 10^{-5}$	$0,176 \cdot 10^{-5}$
ρ^{10}	$-15,2 \cdot 10^{-5}$	$14,5 \cdot 10^{-5}$

Note. c is the radiative capture; f, fis-
sion; the suffixes 8, 9, and 10 correspond
to ^{238}U, ^{239}Pu, and ^{10}B.

The results of the calculations for k_{eff}, the breeding factor in the core (C.B.F.) and
in the whole reactor (R. B. F.), and also the effects of reactivity in the case of removal of
sodium and heating up of the fuel, are compared in Table 1. For the R. B. F. and the C. B. F.,
the results are given in brackets of a recalculation for a critical reactor by means of a
change of enrichment. They were obtained for the condition of conservation of the nuclide
composition and the ratio of the enrichments in both subzones of the core. Table 2 gives the
velocities of the principal reactions and the reactiivty coefficients (material efficiencies)
at the center of the reactor — the quantities measured most frequently on critical assemblies.

The following conclusions can be drawn on the basis of the foregoing:

the revision of the nuclear data for ^{238}U and ^{239}Pu in the forbidden region has led to
an appreciable change of the value of k_{eff} (~0.9%);

the breeding parameters were almost unchanged;

the effect of reactivity in the case of removal of sodium increased by approximately 20%.

clides of of uranium and plutonium) is quite small (~4%), the contribution of ^{239}Pu was reduced markedly (~1.5 times). The latter circumstance can be important for justifying the calculated safety characteristics of fast reactors and the technology of mixed fuel manufacture.

LITERATURE CITED

1. A. A. Van'kov, L. S. Gosteva, and V. F. Ukraintsev, Analysis of Experiments on Transmission for ^{238}U in the Region of Forbidden Resonances [in Russian], Problems of Nuclear Science and Technology. Series Nuclear Constants, Issue 3(52), (1983), pp. 27-32.
2. A. A. Van'kov, S. Toshkov, V. F. Ukraintsev, and N. Yaneva, Group Cross Sections and Resonance Self-Screening Factors of ^{239}Pu in the Region of Forbidden Resonances [in Russian], Problems of Nuclear Science and Technology, Issue 4(53) (1983), pp. 18-25.
3. L. P. Abagyan, N. O. Bazazyants, M. N. Nikolaev, and A. M. Tsibulya, Group Constants for the Calculation of Reactors and Shielding [in Russian], Énergoizdat, Moscow (1981).
4. A. I. Voropaev, O. P. Chukhlova, A. A. Van'kov, et al., "Comparison of calculations of a two-dimensional fast reactor model," At. Énerg., 48, No. 6, 355-357 (1980).
5. O. P. Chukhlova, A. I. Voropaev, A. A. Van'kov, et al., Calculations of the Characteristics of a Standard Fast Reactor (International Two-Dimensional Test Model NEACRP): [in Russian], Preprint FÉI-802, Obninsk (1977).

529

MEASUREMENT TECHNIQUES
Izmeritel'naya Tekhnika
Vol. 27, 1984 (12 issues) $520

MECHANICS OF COMPOSITE MATERIALS
Mekhanika Kompozitnykh Materialov
Vol. 20, 1984 (6 issues) $430

METAL SCIENCE AND HEAT TREATMENT
Metallovedenie i Termicheskaya Obrabotka Metallov
Vol. 26, 1984 (12 issues) $540

METALLURGIST
Metallurg
Vol. 28, 1984 (12 issues) $555

PROBLEMS OF INFORMATION TRANSMISSION
Problemy Peredachi Informatsii
Vol. 20, 1984 (4 issues) $420

PROGRAMMING AND COMPUTER SOFTWARE
Programmirovanie
Vol. 10, 1984 (6 issues) $175

PROTECTION OF METALS
Zashchita Metallov
Vol. 20, 1984 (6 issues) $480

RADIOPHYSICS AND QUANTUM ELECTRONICS
Izvestiya Vysshikh Uchebnykh Zavedenii, Radiofizika
Vol. 27, 1984 (12 issues) $520

REFRACTORIES
Ogneupory
Vol. 25, 1984 (12 issues) $480

SIBERIAN MATHEMATICAL JOURNAL
Sibirskii Matematicheskii Zhurnal
Vol. 25, 1984 (6 issues) $625

SOIL MECHANICS AND FOUNDATION ENGINEERING
Osnovaniya, Fundamenty i Mekhanika Gruntov
Vol. 21, 1984 (6 issues) $500

SOLAR SYSTEM RESEARCH
Astronomicheskii Vestnik
Vol. 18, 1984 (6 issues) $365

SOVIET APPLIED MECHANICS
Prikladnaya Mekhanika
Vol. 20, 1984 (12 issues) $520

SOVIET ATOMIC ENERGY
Atomnaya Energiya
Vols. 56-57, 1984 (12 issues) $560

SOVIET JOURNAL OF GLASS PHYSICS AND CHEMISTRY
Fizika i Khimiya Stekla
Vol. 10, 1984 (6 issues) $235

SOVIET JOURNAL OF NONDESTRUCTIVE TESTING
Defektoskopiya
Vol. 20, 1984 (12 issues) $615

SOVIET MATERIALS SCIENCE
Fiziko-khimicheskaya Mekhanika Materialov
Vol. 20, 1984 (6 issues) $445

SOVIET MICROELECTRONICS
Mikroelektronika
Vol. 13, 1984 (6 issues) $255

SOVIET MINING SCIENCE
Fiziko-tekhnicheskie Problemy Razrabotki Poleznykh Iskopaemykh
Vol. 20, 1984 (6 issues) $540

SOVIET PHYSICS JOURNAL
Izvestiya Vysshikh Uchebnykh Zavedenii, Fizika
Vol. 27, 1984 (12 issues) $520

SOVIET POWDER METALLURGY AND METAL CERAMICS
Poroshkovaya Metallurgiya
Vol. 23, 1984 (12 issues) $555

STRENGTH OF MATERIALS
Problemy Prochnosti
Vol. 16, 1984 (12 issues) $625

THEORETICAL AND MATHEMATICAL PHYSICS
Teoreticheskaya i Matematicheskaya Fizika
Vol. 58-61, 1984 (12 issues) $500

UKRAINIAN MATHEMATICAL JOURNAL
Ukrainskii Matematicheskii Zhurnal
Vol. 36, 1984 (6 issues) $500

Send for Your Free Examination Copy

RUSSIAN JOURNALS IN THE PHYSICAL AND MATHEMATICAL SCIENCES

AVAILABLE IN ENGLISH TRANSLATION

ALGEBRA AND LOGIC
Algebra i Logika
Vol. 23, 1984 (6 issues) $360

ASTROPHYSICS
Astrofizika
Vol. 20, 1984 (4 issues) $420

AUTOMATION AND REMOTE CONTROL
Avtomatika i Telemekhanika
Vol. 45, 1984 (24 issues) $625

COMBUSTION, EXPLOSION, AND SHOCK WAVES
Fizika Goreniya i Vzryva
Vol. 20, 1984 (6 issues) $445

COSMIC RESEARCH
Kosmicheskie Issledovaniya
Vol. 22, 1984 (6 issues) $545

CYBERNETICS
Kibernetika
Vol. 20, 1984 (6 issues) $445

DIFFERENTIAL EQUATIONS
Differentsial'nye Uravneniya
Vol. 20, 1984 (12 issues) $505

DOKLADY BIOPHYSICS
Doklady Akademii Nauk SSSR
Vols. 274-279, 1984 (2 issues) $145

FLUID DYNAMICS
Izvestiya Akademii Nauk SSSR,
Mekhanika Zhidkosti i Gaza
Vol. 19, 1984 (6 issues) $500

FUNCTIONAL ANALYSIS AND ITS APPLICATIONS
Funktsional'nyi Analiz i Ego Prilozheniya
Vol. 18, 1984 (4 issues) $410

GLASS AND CERAMICS
Steklo i Keramika
Vol. 41, 1984 (6 issues) $590

HIGH TEMPERATURE
Teplofizika Vysokikh Temperatur
Vol. 22, 1984 (6 issues) $520

HYDROTECHNICAL CONSTRUCTION
Gidrotekhnicheskoe Stroitel'stvo
Vol. 18, 1984 (12 issues) $385

INDUSTRIAL LABORATORY
Zavodskaya Laboratoriya
Vol. 50, 1984 (12 issues) $520

INSTRUMENTS AND EXPERIMENTAL TECHNIQUES
Pribory i Tekhnika Éksperimenta
Vol. 27, 1984 (12 issues) $590

JOURNAL OF APPLIED MECHANICS AND TECHNICAL PHYSICS
Zhurnal Prikladnoi Mekhaniki i Tekhnicheskoi Fiziki
Vol. 25, 1984 (6 issues) $540

JOURNAL OF APPLIED SPECTROSCOPY
Zhurnal Prikladnoi Spektroskopii
Vols. 40-41, 1984 (12 issues) $540

JOURNAL OF ENGINEERING PHYSICS
Inzhenerno-fizicheskii Zhurnal
Vols. 46-47, 1984 (12 issues) $540

JOURNAL OF SOVIET LASER RESEARCH
A translation of articles based on the best Soviet research in the field of lasers
Vol. 5, 1984 (6 issues) $180

JOURNAL OF SOVIET MATHEMATICS
A translation of Itogi Nauki i Tekhniki and Zapiski Nauchnykh Seminarov Leningradskogo Otdeleniya Matematicheskogo Instituta im. V. A. Steklova AN SSSR
Vols. 24-27, 1984 (24 issues) $1035

LITHOLOGY AND MINERAL RESOURCES
Litologiya i Poleznye Iskopaemye
Vol. 19, 1984 (6 issues) $540

LITHUANIAN MATHEMATICAL JOURNAL
Litovskii Matematicheskii Sbornik
Vol. 24, 1984 (4 issues) $255

MAGNETOHYDRODYNAMICS
Magnitnaya Gidrodinamika
Vol. 20, 1984 (4 issues) $415

MATHEMATICAL NOTES
Matematicheskie Zametki
Vols. 35-36, 1984 (12 issues) $520